IPP-Report

Max-Planck-Institut für Plasmaphysik

Christoph Adelhelm

Structure and Erosion Behavior of Metal-doped Carbon Films

IPP 17/11
November, 2008

TECHNISCHE UNIVERSITÄT MÜNCHEN
Max-Planck-Institut für Plasmaphysik

Structure and Erosion Behavior of Metal-doped Carbon Films

Christoph Adelhelm

Vollständiger Abdruck der von der Fakultät für Maschinenwesen der Technischen Universität München zur Erlangung des akademischen Grades eines

Doktors der Naturwissenschaften

genehmigten Dissertation.

Vorsitzender:	Univ.-Prof. Dr.-Ing. H. Baier
Prüfer der Dissertation:	1. Hon.-Prof. Dr.-Ing., Dr.-Eng. (Univ. Nagoya/Japan) H. H. Bolt
	2. Univ.-Prof. Dr. phil. nat. U. K. Heiz
	3. Univ.-Prof. Dr. mont. habil. E. Werner

Die Dissertation wurde am 30.01.2008 bei der Technischen Universität München eingereicht und durch die Fakultät für Maschinenwesen am 29.07.2008 angenommen.

Für Katrin, Hannah und Mathilda

Kurzfassung

Die erste Wand von Fusionsexperimenten ist hohen Teilchen- und Wärmeflüssen aus dem Plasma ausgesetzt. Aufgrund der guten thermomechanischen Eigenschaften soll im zukünftigen Fusionsreaktor ITER faserverstärkter Kohlenstoff (CFC) für die am stärksten belasteten Bereiche des Divertors verwendet werden. Allerdings führt die chemische Reaktion mit Wasserstoffionen aus dem Plasma zur Erosion von Kohlenstoff (*chemical sputtering*) und zur Abscheidung von unerwünschten Kohlenwasserstoffschichten im Reaktor. Da in Zukunft radioaktives Tritium als Fusionsbrennstoff verwendet werden soll, baut sich durch diese Schichtbildung ein radioaktives Inventar auf, das ein erhebliches Sicherheitsproblem darstellt. Werden zusätzlich metallische Materialien an anderen plasmabelasteten Stellen eingesetzt, führt dies zur Bildung von metallhaltigen Kohlenwasserstoffschichten mit neuen Eigenschaften. Deren Erosionsverhalten ist von großer Bedeutung.

Metalldotierte Kohlenstoffmaterialien zeigen eine deutlich verringerte Erosion im Vergleich zu reinem Kohlenstoff. Dies beruht auf dem Einfluss des Dotierelements auf den Erosionsmechanismus und der schrittweisen Bildung einer schützenden, metallangereicherten Oberflächenschicht durch bevorzugte Erosion von Kohlenstoff. Um den Einfluss der Dotierung auf das Erosionsverhalten systematisch zu untersuchen, wurden amorphe, metalldotierte Kohlenstoffschichten (a-C:Me) mittels Magnetronsputtern hergestellt. Die genaue Kenntnis der Metallverteilung und der Struktur der Kohlenstoffmatrix ist nötig, um einen Einfluss der Filmstruktur auf die Erosion untersuchen zu können. Diese Arbeit beschäftigt sich deshalb hauptsächlich mit der Untersuchung der nanoskopischen Struktur der a-C:Me Filme in Abhängigkeit von Metalldotierung (Me=Ti, V, Zr, W), Metallkonzentration ($<$15 %) und Temperaturbehandlung (bis 1300 K). Nach der Abscheidung weist das Metall carbidischen Bindungscharakter auf und ist größtenteils atomar dispers in der amorphen Kohlenstoffmatrix verteilt. Dies geht aus Messungen mittels in Röntgenabsorptionsspektroskopie (XAFS) und Röntgenbeugung (XRD) hervor. Anschließendes Tempern führt zur Bildung von mehreren Nanometer großen Carbidkristalliten (TiC, VC, ZrC). Die Teilchengröße ist für VC am größten. Die Wolframcarbid-Phase in a-C:W Filmen konnte nicht eindeutig bestimmt werden. Nach Heizen auf 1300 K ähnelt die lokale atomare Umgebung der Wolframatome derjenigen in W_2C. Wahrscheinlich bilden sich schon während der Abscheidung sehr kleine, stark ungeordnete Carbidkristallite bzw. eine Mischung aus W_2C und WC_{1-x}. Mit Hilfe der Ramanspektroskopie konnte ein Einfluss der Metalldotierung auf die Größe von aromatischen Clustern in der Kohlenstoffmatrix gezeigt werden. Dabei haben Ti und Zr den größten Effekt während des Schichtwachstums. Durch anschließendes Tempern verringert sich der Einfluss der Dotierung auf die Clustergröße. Diese ist ab 1100 K vergleichbar mit der in undotiertem a-C. Somit kann die geheizte a-C:Me Schicht als Nanokomposit betrachtet werden, bestehend aus Carbidkristalliten in einer a-C Matrix. Der sp^2 Anteil in a-C erhöht sich durch Heizen von $\approx$80 % auf 95 % (1300 K).

Die Bildung von CD_4 als Erosionsprodukt durch Beschuss mit Deuteriumionen wurde mit-

tels Massenspektrometrie untersucht. Es zeigte sich eine deutliche Reduzierung im Fall von metalldotierten Filmen, besonders bei erhöhten Temperaturen. Dies kann durch eine metallinduzierte Erniedrigung der Aktivierungsenergie für die Freisetzung von Wasserstoff erklärt werden. Allerdings erhöht sich durch Dotierung der relative Anteil von CD_4 als Erosionsprodukt, was durch einen Vergleich mit der Gesamtmenge an erodiertem Kohlenstoff gezeigt werden konnte. Besonders bei niedrigen Energien und hohen Temperaturen steigt die relative CD_4-Ausbeute – auf Kosten von höheren Kohlenstoffspezies. In Plasmaerosionsexperimenten wurde der Einfluss der Schichtstruktur auf die Erosion untersucht. Ist in a-C:V Filmen Vanadium hauptsächlich atomar dispers verteilt, zeigen sich niedrigere Erosionsausbeuten als im Fall einer geheizten Probe, in der das Metall in Form von Carbidkristalliten vorhanden ist.

Abstract

The reactivity of carbon against energetic hydrogen species (chemical sputtering) is the main drawback for its application as a plasma-facing material (PFM) in future fusion reactors like ITER. It causes lifetime problems of the components and the formation of undesired hydrocarbon layers. If radioactive tritium is used, the formation of an in-vessel tritium inventory is of high safety concern. The combination of metallic and carbon-based materials as PFMs, leads to formation of mixed metal-hydrocarbon layers with new properties. Their erosion behavior under hydrogen impact is of great importance.

Doped carbon materials show strongly reduced erosion yields compared to pure carbon. This is due to an influence on the erosion mechanism and the successive formation of a protective metal-enriched surface region. Amorphous metal-doped carbon films (a-C:Me) are ideal test materials for systematic erosion studies. To be able to investigate the influence of the film structure on the erosion process, basic information about the metal distribution and the structure of the carbon matrix is required. Therefore, the structure of a-C:Me films was systematically analyzed in this work. The investigated parameters were type of doping metal (Me = Ti, V, Zr, W), metal concentration (<15 %), and annealing temperature (up to 1300 K). X-ray absorption fine structure spectroscopy (XAFS) and X-ray diffraction (XRD) showed, that after deposition the metal has carbide-like bonding character and is mainly distributed atomically disperse in an amorphous environment. Annealing leads to formation of carbide crystallites (TiC, VC, ZrC) of several nm, of which VC particles have the largest size. In a-C:W films, the local W coordination is similar to W_2C after annealing to 1300 K. For lower temperatures, the carbide phase could not be resolved. Probably a mixture of very small and distorted carbide crystallites occurs (W_2C, WC_{1-x}). Raman spectroscopy showed the influence of doping and annealing on the degree of clustering of the carbon sp^2 phase in aromatic rings. Compared to pure a-C, the addition of up to 15 % metal leads to a continuous increase of the average aromatic cluster size in the as-deposited samples. The strongest effect was observed for Ti and Zr. Annealing diminishes the differences of the different dopants regarding the clustering of the sp^2 phase. After heating to 1100 K, the aromatic cluster size is the same as for a-C, independent of metal type and content. For that temperature, the a-C:Me film structure can be described as a nanocomposite of carbide crystallites embedded in an a-C matrix. For a-C, the sp^2 content increases with annealing from ≈80 to 95 %.

Under 200 eV D ion bombardment, a-C:Me films showed a significant reduction of the CD_4 production, especially at high temperatures. This is explained by a lowering of the activation energy for hydrogen release. However, comparison of the total erosion with CD_4 production showed that especially at low ion energies and high temperatures a much higher suppression of the erosion occurs than indicated by the CD_4 production. This indicates that doping strongly alters the distribution of erosion species to more CD_4 production at expense of higher hydrocarbons. The influence of the nanostructure on the erosion yield was observed

in plasma erosion of a-C:V films. If the metal is present atomically disperse, a lower erosion yield was found than for erosion of pre-annealed samples with VC crystallites.

Contents

Chapter 1

Introduction

Safe and sustainable energy supply for a growing world population with increasing energy demand is one of the most important issues mankind has to deal with in the coming decades. By 2030, the world's primary energy demand will increase by nearly 50 % [1]. Presently, more than 80 % of the consumed energy is based on fossil fuels. The maximum output of oil is expected in about 10-20 years, whereas coal will be available for more than 100 years [2]. Despite the resource issue, the effects of global warming will force us to drastically reduce the production of the green house gas CO_2, associated with the burning of carbon-based fuels[1].

Since nuclear fission (applied as fast breeder technique) is hardly an option due to unsolved disposal, proliferation and safety policy issues, only three main long term primary energy sources remain: solar energy (i.e. all *renewable energies*), geothermal energy and nuclear fusion.

Nuclear fusion as energy source

Energy generation by nuclear fusion – which is actually the origin of solar energy – utilizes the fact, that the nuclear binding energy of the atom formed (e.g. helium) is larger than that of the original light atoms (e.g. hydrogen) that undergo fusion, i.e. energy is released. Thanks to the sufficient large cross-section, the most promising reaction is fusion of the hydrogen isotopes deuterium and tritium occurring at about 100 Mio. K in a plasma reactor with magnetic confinement [4]:

$$D + T \longrightarrow {}^4He\,(3.5\,MeV) + n\,(14.1\,MeV)$$

Utilizing the heat generated from impacting neutrons and particles, electrical energy will be generated via a conventional steam process.

Resources required for this type of energy generation are available for centuries: Deuterium can be extracted from abundant sea water, whereas tritium will be bred from lithium, which is widespread in the earth's crust. Nevertheless, due to immense technological challenges, a commercial fusion plant is not expected before mid-century. After some years of operation, a fusion plant will accumulate radioactive inventory due to activation of materials by neutron

[1] According to the 2007 IPCC report an absolute reduction of greenhouse gas emissions of 50 to 85 % in 2050 (based on the year 2000) is required to stabilize the global temperature increase to 2 to 2.4 °C since the beginning of industrialization [3].

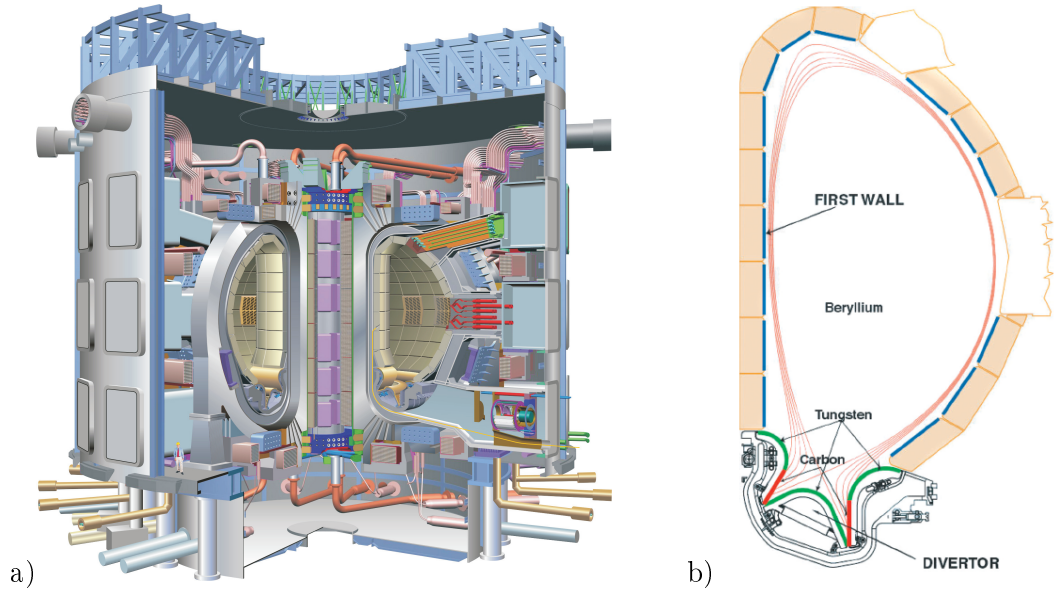

Figure 1.1: *a) Principal design of ITER, the next-step fusion device to be built in Cadarache, France. The person on the left gives a rough scale on the dimensions. Source: www.iter.org. b) ITER cross-section with the divertor system at the bottom. The different wall materials Be, W and C are located as indicated. The red lines represent the main magnetic field lines. Taken from [5].*

irradiation. The total amount generated is comparable to fission plants, but the much lower half-life of the formed radioactive isotopes leads to timescales for safe storage of only about 100-150 years. This is much less compared to the nuclear waste generated from fission reactors, which have to be safely stored for thousands of years.

Controlled nuclear fusion has been studied for about 60 years, and is now on the border of demonstrating its feasibility for power generation. In 1997, JET, the largest fusion reactor built yet, achieved a fusion power of 16 MW, 65 % of the power consumed for heating the plasma. This is expressed by the fusion energy gain factor Q, which is 0.65 for that JET experiment. The joint international research and development project ITER, shown schematically in Fig. 1.1a, aims "to demonstrate the scientific and technological feasibility of fusion power for peaceful purposes". Projected to be built in France between 2008 and 2016, ITER will be the first experiment realizing a net energy gain with Q >5-10 and operate at quasi steady-state.

One of the most critical issue facing ITER is the choice of the plasma-facing materials (PFM) that must handle the high power and particle loads without degradation. Although currently under review [6], three different wall materials have been considered for different areas [7], as indicated in Fig. 1.1b. Beryllium-coated tiles cover the main chamber (≈1000 m^2), where only moderate power and particle loads are expected. Therefore, Be can be employed with its benefit as a low-Z material and acting as an oxygen getter.

The highest power and particle impact will occur at the *divertor* component located at the bottom of the reactor. The main function of the divertor system is to dissipate a large portion of the alpha particle power, and serve as an exhaust for He ash and other impurities [8]. In ITER, mainly tungsten (≈100 m^2) will be applied in the divertor since it is able to handle

the expected heat loads of ≈3 MW m^{-2} while possessing a high sputtering threshold [9]. The divertor *strike point* region has to withstand up to 20 MW m^{-2} during thermal shocks which requires carbon in form of 75 m^2 tiles of carbon fiber reinforced carbon (CFC).

Carbon as plasma-facing material [10–12]

Carbon-based materials – graphite and CFC – have been successfully applied as PFM in many fusion devices, allowing optimization of the plasma core performance and exploitation of a large range of plasma conditions. As a low-Z material, carbon atoms are fully ionized in the plasma. Therefore, the plasma can tolerate about one percent C without major impact on plasma performance and radiation loss. Carbon-based PFMs show good thermomechanical properties, thermal shock resistance during off-normal events (ELMs, disruptions), and are not at risk to melting. Therefore, the application of CFC is probably essential for the strike point region of the ITER divertor during the first phase of operation. Another advantage is the low activation of carbon by neutrons. However, carbon offers two severe drawbacks:

1. The high chemical reactivity with hydrogen species (**chemical sputtering**, section 3.2) could lead to lifetime problems of the installed components leading to frequent replacements.

2. As a result of carbon erosion, the reaction products will partly deposit in the reactor vessel as hydrocarbon layers. Since they contain radioactive tritium, **tritium retention** is of high safety concern in case of an accident. A limit of ≈350 g tritium is set for the in-vessel inventory in ITER [13].

An additional problem is the trapping of tritium in the bulk of CFC and graphite [14, 15]. If the retention limit is reached (in the worst case after less than 100 pulses [16]) operation must be stopped. Therefore, tritium removal technologies are indispensable if carbon is to be used as a PFM. Some techniques currently under investigation include oxidation, and flash lamp and laser ablation [17]. They are planned to be applied during night and shut-down periods. Hydrocarbon layers deposited in hidden gaps are of special concern [18, 19].

Besides the already mentioned removal techniques, other suggestions were proposed to solve this problem, e.g. increasing the PFM temperature above 1000 K could significantly reduce the tritium inventory [14]. Another strategy is the developement of self-passivating graphite and CFC materials with high erosion resistance, which could drastically reduce the above mentioned drawbacks of pure carbon materials.

Carbon materials with improved erosion resistance

Doping (e.g. B, Si, transition metals) is shown to strongly reduce chemical sputtering, which is a result of surface enrichment and chemical influence [20, 21] (see section 3.2). Unfortunately doping often results in worse mechanical properties. One promising combination is Si-containing CFC, developed some years ago [22]. However, current research is also perfomed on transition metal doped graphites with improved thermal conductivity [23, 24], where Ti and Zr seems to be the most promising dopants. The Chinese tokamak HT 7 is operated with B/Si/Ti-doped graphite [25], which is also employed as a PFM in the 2006 commissioned fusion reactor EAST [26]. Nevertheless, up to now, the thermal conductivity and mechanical strength of such erosion improved carbon materials are still not high enough to be employed in the ITER divertor.

Plasma wall interaction and mixed material formation

During fusion reactor operation, PFMs experience erosion and redeposition processes which alter their surface composition. Such *mixed material* formation must be considered if different elements are used together as PFMs. This is of great importance since the modified surfaces exhibit different properties from the original, leading to an altered plasma-wall interaction with impact on the plasma performance. To investigate the complex interaction of the plasma with different wall materials, numerous studies have been performed with lab-scale plasma (e.g. PSI-2 [27], PISCES [28]) and ion-beam experiments (e.g. at IPP and ORNL [29]). Important results are expected from the ITER-like wall project at JET [30] and the recently completed change of ASDEX Upgrade from a full carbon to a full tungsten machine [31]. Nevertheless, plasma-wall investigations in the ITER relevant flux regime are not possible with present experiments. For this purpose, the facility Magnum-PSI is being built in Belgium [32].

Aim of the present work

At IPP, the erosion of (doped) graphites and CFCs by ion beams have been investigated for several years [33–38]. With growing concern of the mixed materials issue, artificial metal-containing amorphous carbon films (a-C:Me) were investigated [33, 39, 40]. They were produced by magnetron sputter deposition and can be regarded as a model for metal-containing hydrocarbon layers, produced in a fusion device with carbon and metallic PFM. Due to the flexibility in dopant metal and concentration, systematic investigations of the erosion yield regarding metal type and concentration are possible. Since it was assumed that the dopant distribution has significant influence on the erosion yield, structural characterization of the a-C:Me films used for the erosion experiments was required. Basic knowledge about the structure of a-C:Me films is also important for the application of such films as hard coating or for wear protection [41–44].

The main focus of the present work was, therefore, **characterization** of the a-C:Me film structure in detail. The influence of three parameters on the film structure was thoroughly investigated (Fig. 1.2): The metal type (Ti, V, Zr, W), metal concentration (generally $<15\,\%$), and annealing after deposition (700-1300 K). The interest in the chosen dopant metals is driven by ITER's material choice (W) and the possible use of doped (Ti, Zr, V) graphite as divertor PFM. The metal content in the carbon films was limited to low concentrations, since even small amounts of metal supress the chemical erosion strongly. Also the carbon layers formed in fusion devices incorporate only low amounts of metal.

Different analytical techniques were used for characterization – offering structural information on several length scales. A review of the main applied techniques is given in chapter 2. Background information on amorphous carbon films and erosion of carbon by hydrogen is summarized in chapter 3. Experimental details can be found in chapter 4.

Two main objectives are pursued in characterizing a-C:Me films given in chapter 5: To identify the *metal distribution and phase* and to investigate structural changes of the *carbon matrix* (Fig. 1.2). XAFS investigations of the atomic environment of the metal are presented, as well as size data of carbide crystallites, determined by XRD and TEM. A special section is devoted to the carbide phase in a-C:W, investigated by XAFS and XES. Only limited information about crystallinity in the carbon matrix could be gained from XRD. The carbon phase was mainly characterized by Raman spectroscopy to investigate aromatic clustering and by NEXAFS and XPS to investigate the carbon bonding state.

Following the characterization work, a secondary focus is the investigation of the **erosion behavior** of a-C:Me films and other doped carbon materials under deuterium impact (Fig. 1.2), given in chapter 6. This connects the work to fusion research. Temperature-dependent measurements of the CD_4 production yield during 200 eV D bombardment of a-C:Me are presented. Special attention is dedicated to a comparison of the total erosion yield and the contribution of CD_4 as erosion species. In plasma erosion experiments, the dependence of the erosion yield on the dopant distribution was investigated. The erosion behavior of a-C:Me films with nm-sized carbide crystallites is compared with films showing an atomically disperse dopant distribution. In the frame of the European Integrated Project ExtreMat [45], doped graphite and CFC materials, developed by two independent groups in Spain, were also investigated in respect to deuterium erosion resistance. Results from ion beam erosion are also presented in chapter 6.

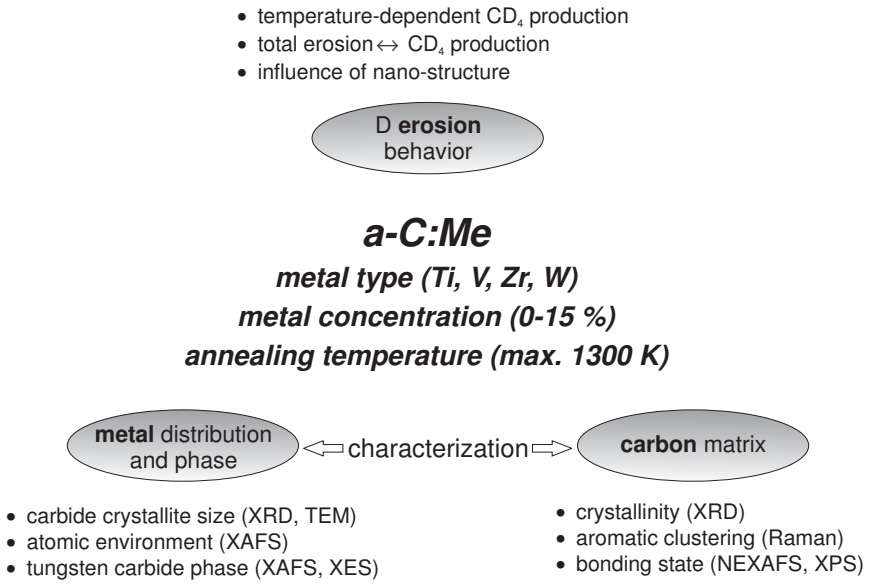

Figure 1.2: *This work is divided into characterization and erosion studies with three main objectives: Investigation of a) metal distribution and phase, b) the structure of the carbon matrix and c) D erosion of a-C:Me films.*

Chapter 2

Characterization techniques and film deposition

This chapter describes the main characterization techniques used in this work. The last section deals with the basic principles of film deposition by magnetron sputtering. It is not intended to give a complete theoretical description of each technique, which can be gathered from the quoted references. Microsopy techniques (SEM, TEM, AFM) are not described, detailed information can be found in [46–49]. The main objective is to explain the basic principles and to illustrate the strengths and limitations for each technique. Important aspects are also on which length scale information can be gathered and the probed sample depth. Generally surface or bulk sensitive techniques are distinguished. Fig. 2.1 roughly classifies most of the applied characterization techniques in respect to *probed sample depth* and *information length scale*. The latter should be regarded as a *soft* phrase and not to be confused with the resolution of the technique itself. X-ray diffraction for example is used in this work to quantify the size of carbide crystallites which are several nm in size. Nevertheless, X-ray diffraction can also be used to determine bond distances in the Å range. In general, the probed sample depth is in the µm range when X-rays are utilized and detected. Due to the low mean free path of electrons in matter, all techniques which use electron detection are surface sensitive.

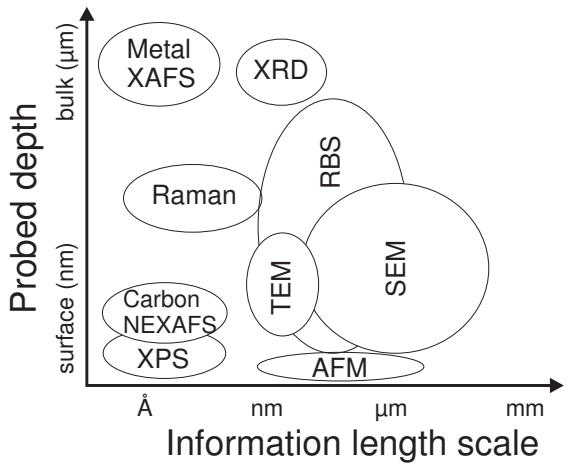

Figure 2.1: *Summary of different characterization techniques used in this work. They are classified in respect to the probed sample depth and the length scale on which information is gained.*

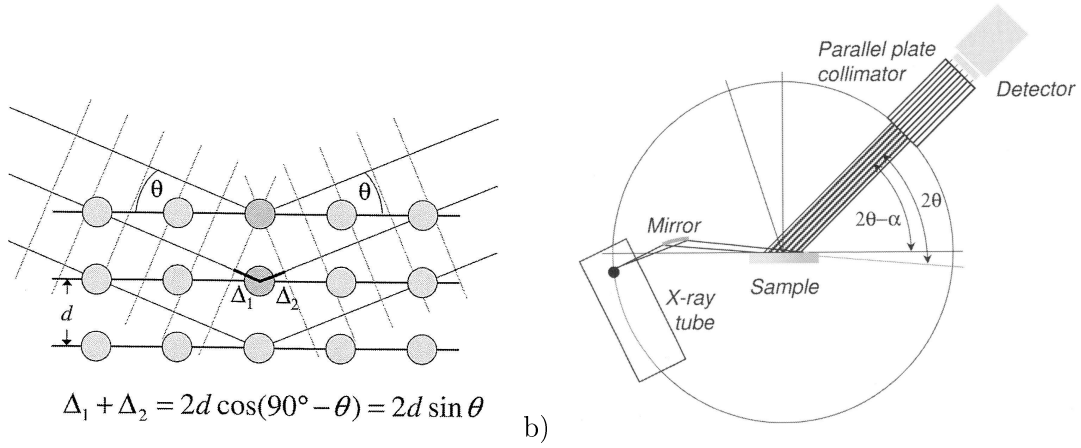

Figure 2.2: *a) Illustration of the relation between latice spacing d and the phase shift 2d sinθ manifested in the Bragg equation. b) Principle of gracing incidence measurement geometry applied for thin film analysis. Both pictures from [51].*

2.1 X-ray diffraction (XRD)

Elastic scattering (*Thomson scattering*) of X-ray radiation with matter is the basis for all structural analysis by X-ray diffraction (XRD) since the wavelength of X-rays is on the length scale of interatomic disctances. The radiation is scattered at electrons which are excited to oscillate at the frequency of the incoming beam. If periodic structures are present, a diffraction experiment leads to maxima at defined scattering angles, due to constructive interference [50]. The *Bragg equation* correlates the distance d of two crystal lattice planes with the observed diffraction angle θ, when radiation of a wavelength λ is scattered at the planes [51]:

$$2d\,sin\theta = n\lambda \tag{2.1}$$

Fig. 2.2a illustrates that constructive interferrence only occurs if the phase shift $2d\ sin\theta$ between the two reflected waves is a multiple n of the wavelength.

The number, positions and intensities of the diffraction peaks (the *diffraction pattern*) are dependent on the crystal structure and can therefore be used to determine the crystallographic phase of a substance. This can be done by comparing the diffraction pattern with known crystal sturctures, which can be gathered from databases. The most frequently used measurement geometry is the $\theta/2\theta$ configuration. Here, the diffraction pattern is collected by changing the X-ray incidence angle by θ and the scattering angle by 2θ. In a diffractogram the scattered intensity is plotted as function of 2θ.

The penetration depth of X-rays is in the 10-100 µm range – according to X-ray attenuation coefficients of about 10^4-10^5 m^{-1}. For measuring thin films with a thickness of only about one µm, this causes the majority of the detected signal originating from the substrate. To overcome this problem, a special measurement configuration has been applied (*gracing incidence*, GIXRD), where the radiation hits the sample at very low angle of incidence. This increases the traveling path of the beam in the film and lowers the substrate signal. The gracing incidence measurment configuration used in this work is shown in Fig. 2.2b. In contrast to the usual $\theta/2\theta$ geometry, the diffractogram is collected by only moving the detector at fixed incidence angle α. Aditionally, the whole beam geometry is changed from a focused

beam to a parallel beam. This is provided by a laterally graded multilayer mirror consisting of alternating Si/W layers, which is installed in front of the exit slit of the X-ray tube. By that, the beam divergence is reduced to only a few 0.01°. To exclude that contributions of other scattering angles reach the detector, a parallel plate collimator is installed on the secondary side.

A very small crystallite size leads to broadening of the measured diffraction peaks. By applying the Scherrer formula the average crystallite size D can be calculated [51]

$$D = \frac{0.9394\,\lambda}{B_{2\theta}\,cos\theta_B} \tag{2.2}$$

with $B_{2\theta}$ the peak FWHM, θ_B the peak position, and λ the radiation wavelength (e.g. 0.154 nm for Cu $K\alpha$). Using this relation it is assumed that peak-broadening is determined by the small crystallite size only. Nevertheless, there exist several other factors which have impact on peak-broadening (i.e. the FWHM) as there are the crystallite shape, the shape distribution, and distortions in the crystal structure like stacking faults, dislocations and microstrain. Also, it has to kept in mind that the Scherrer formula is derived for monodisperse (i.e. all particles have the same size), cube-shaped crystallites. For spherical particles, which is more realistic, the prefactor is ≈1. As outlined in [51], the assumption of a log-normal size-distribution results in an volume-weighted average crystallite size determined by XRD, which is much larger than a number-weighted average crystallite size. On the other hand, the coherently diffracting domains (influencing the FWHM) are smaller than the particle size observed by TEM.

Being aware of the different influences on peak broadening and the unrealistic assumption of monodisperse crystallite distribution, size determination by the Scherrer equation should be regarded as an estimate. Nevertheless, the evolution of the carbide particle size by annealing of a-C:Me films can be followed easily as shown in section 5.2.1.

2.2 Raman spectroscopy

Raman spectroscopy is a common and versatile technique to gain structural information about disordered amorphous carbon, although the derivation of quantitative information is often challenging [52]. First, the basic principle of Raman spectroscopy is described, then the Ferrari-Robertson model (FM model) is presented, which correlates features of the visible Raman spectra to the carbon structure. Finally, peak fitting is discussed, since this is essential for quantitative comparison.

2.2.1 The Raman effect

Raman spectroscopy is based on the inelastic scattering of light involving excitation of vibrational modes [53]. Three basic processes are shown schematically in Fig. 2.3. Only vibrational modes are considered, being aware that also electronic or rotational energy could change. For elastic scattering, also termed *Rayleigh scattering*, the scattered photons have the same energy (and therefore wavelength λ) as the incident light. This is explained by the excitation from the vibrational ground state into a virtual state. Transition back to the ground state leads to the emission of light of the same wavelength. For a small fraction of photons (only about one out of 10^7), *Stokes scattering* occur, leading to a transition into the first vibrational state. The emitted photon has a lower energy and therefore a larger wavelength. This shift in energy

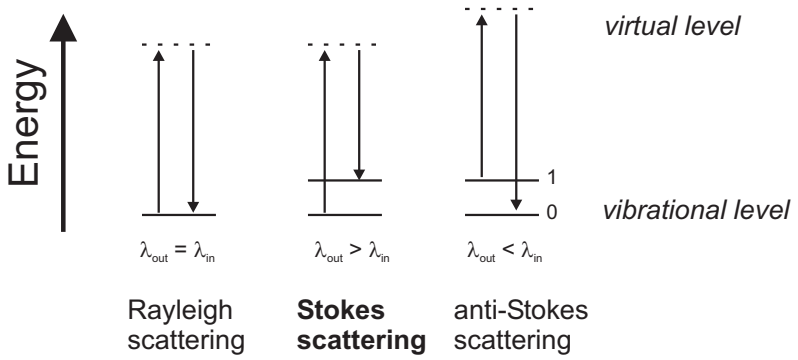

Figure 2.3: *Elastic and inelastic light scattering processes. Raman spectra are recorded by collecting the light from Stokes scattering.*

is called the *Raman shift* and is usually used as the x-axes of a Raman spectrum. The third process (*anti-Stokes*) leads to emission of photons with higher energy, because the transition into a virtual state starts from the first vibrational state and ends up in the vibrational ground state. This process has much lower probabilty compared to Stokes scattering since at room temperature the population of the first vibrational level is very low.

In a modern Raman microscope, a laser is used for excitation and the measurement is perfomed in that way, that the Stokes scattered part of the light is separated from the Rayleigh line. By means of a grating the Stokes intensity is recorded as function of the energy shift from the Rayleigh line (Raman shift). The probed depth for carbon materials is in the range of 50-100 nm for visible laser light [52].

2.2.2 The Ferrari-Robertson model

Raman spectroscopy of carbon materials is usually performed using visible light, e.g. in this work with an Ar^+ laser emitting at 514.5 nm. In this case, mainly vibrational modes from sp^2 bonded carbon atoms contribute to the spectrum, because visible light preferentially exite π states. But the spectrum depends strongly on the ordering of the sp^2 sites. In Fig. 2.4a the typical shape of a Raman spectrum of amorphous carbon is given. Following the interpretation of Ferrari and Robertson [54], it can be described by two features, i.e. the so-called G and D peaks. The G peak around 1550 cm^{-1} is due to the in-plane bond-stretching motion of sp^2-bonded carbon atoms. This relative motion can occur for all sp^2-bonded carbon atoms in rings and chains. The D peak at $\approx$1360 cm^{-1} is symmetry forbidden for perfect graphite and occurs in the presence of disorder. It is only active in sixfold aromatic rings. For amorphous carbon both peaks are very broad and overlap each other, so peak fitting is essential to determine their position, width and intensity.

In 2000, Ferrari and Robertson [54] introduced a model to correlate the visible features, i.e. D and G peak, to different carbon structures (Fig. 2.4b). They distinguish 3 stages, confined by 4 kinds of carbon materials with different order. It starts from the material with the highest order – graphite – and by increasing amorphization, other states of carbon materials are reached. In **stage 1** a transition from well-ordered graphite with large crystal sizes to nanocrystalline graphite with small crystallite size occurs. In this stage, increasing disorder is associated with increasing G peak position (G_{max}) and an increasing intensity ratio of D and G peak, I(D)/I(G). The in-plane graphite crystallite size L_a (determined by XRD) is inverse

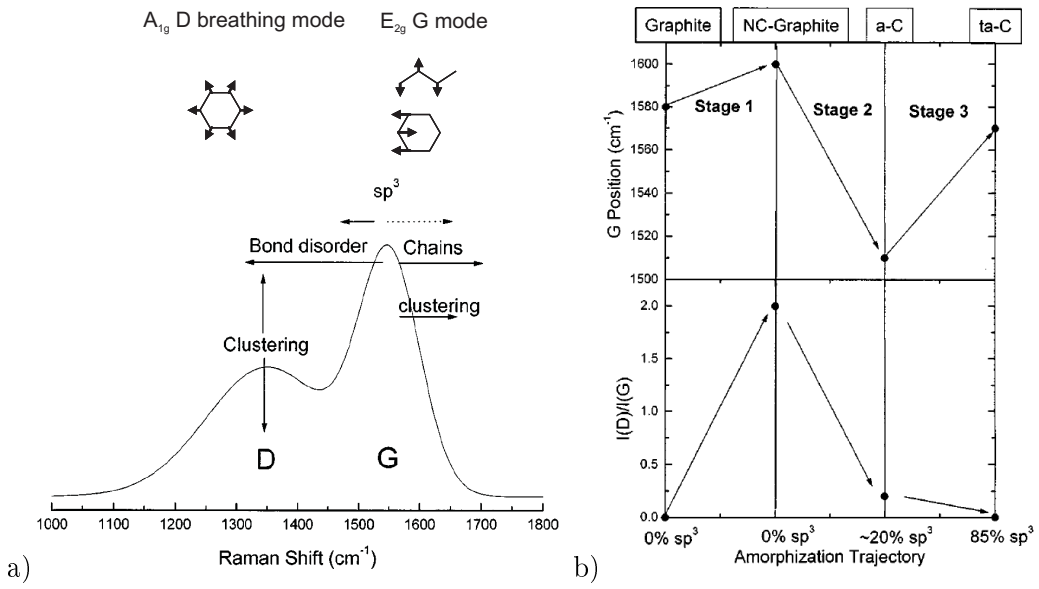

Figure 2.4: *a) Typical shape of a Raman spectrum of amorphous carbon with structural parameters, influencing the spectral shape. On top the responsible vibrational modes are illustrated. b) 3-stage model developed by Ferrari and Robertson to correlate spectral Raman parameters (I(D)/I(G) and G peak position, G_{max}) with the structure of carbon materials. Taken from [54].*

proportional to the I(D)/I(G) ratio as described by the relationship found by Tuinstra and Koenig [55]: $I(D)/I(G) = 0.44\,\mathrm{nm}/L_a$. In **stage 2**, amorphization leads to the collapse of graphite crystallites and the structure is better described by clusters of aromatic rings, which can show high distortion. Also transformation for sp^2 to sp^3 bonded carbon occurs. The end of this stage is set by sputtered amorphous carbon (a-C). In this stage, I(D)/I(G) and G position both decrease with increasing disorder. Further amorphization leads to stage 3 which is characterized by a massive increase of sp^3 bonded carbon and the transformation of sp^2 sites located in rings into olefinic chains. The end of this stage is tetrahedral amorphous carbon (ta-C).

All carbon films used in this work were deposited by magnetron sputtering, so it is assumed that the carbon structure is always described by stage 2, especially when increasing the order by annealing. This increases the amount of sp^2 sites in clustered aromatic rings. Since the D peak is due to the breathing mode of aromatic rings, it gains intensity and I(D)/I(G) rises. In stage 2, the G peak position also increases with higher order. Since the average C=C bond is strenghted due to less bond disorder, this leads to a higher vibration frequency of the relative C=C motion, shifting the G peak position to higher energy. Generally also the FWHM of D and G peak decreases with increasing order, according to the decreased bonding angle distortion. For stage 2, Ferrari and Robertson [54] proposed the following relation between I(D)/I(G) and L_a for cluster sizes smaller than 2 nm (using an excitation laser wavelength of 514.5 nm):

$$L_a = [(I_D/I_G)/0.0055]^{0.5}\ \text{Å}. \tag{2.3}$$

This formula is applied in this work only to give an impression of the aromatic cluster size,

beeing aware that this can only be a rough estimation. It can not be unambigiously confirmed by XRD or other techniques, due to the amorphous character of the material. Nevertheless, Raman spectroscopy is an unique technique to study nm-range order in a-C films.

2.2.3 Peak fitting of Raman spectra

Different approaches using various line shapes exist for fitting Raman spectra of amorphous carbon [54,56–58]. It is important to note that there is no a priori reason to favor a particular fitting function. In literature, two Gaussians are common [56, 57], but also asymmetrical line shapes as the Breit-Wigner-Fano (BWF) are used [54, 58]. If one assumes a random distribution of phonon lifetimes in a disordered material, a Gaussian line shape is expected [54]. Nevertheless, to fit spectra of a-C or a-C:Me it is often not sufficient to use only two Gaussians for D and G peak, and additional peaks have to be introduced to simulate the whole spectrum properly [59,60]. There exist assignments of additional peaks to vibrational modes of planar rings with 5-7 atoms [61] or graphene-analog clusters [62] but they are only based on theoretical calculations and used for fitting spectra of a relatively ordered form of amorphous carbon.

The use of an asymmetric line shape is justified by the asymmetry of the vibrational density of states (DOS) towards lower wave numbers for graphite and amorphous carbon in the region of the D and G lines [63]. The BWF line shape arises from the coupling of a discrete Raman mode to a continuum of Raman modes [64,65]. Asymmetrical line shapes allow to fit the whole spectrum with only two peaks, e.g. a linear background combined with a BWF for the G peak and a Lorentzian for the D peak [54,64,66,67]. The strength of this combination is the increased fit quality and one is able to fit spectra of different shapes with the same set of functions. McCulloch et al. [64] demonstrated the suitability of this combination in amorphisation experiments of glassy carbon by xenon ion beam bombardment, which causes strong structural modifications resulting in strongly altered Raman spectra.

The following expression describes the BWF line shape [54]:

$$I(\omega) = \frac{I_0 \left[1 + \frac{2(\omega-\omega_0)}{Q\Gamma}\right]^2}{1 + \left[\frac{2(\omega-\omega_0)}{\Gamma}\right]^2}, \tag{2.4}$$

with $I(\omega)$ the intensity of the Raman signal at wave number ω, ω_0 as the peak position, I_0 as the peak intensity at ω_0, Γ as the full width at half maximum (FWHM) and $\frac{1}{Q}$ as the BWF coupling coefficient. For $\frac{1}{Q} \to 0$ the line shape converge to a Lorentzian. Due to the asymmetry the maximum of the G peak (G_{max}) is located at

$$\omega_{max} = \omega_0 + \frac{\Gamma}{2Q}. \tag{2.5}$$

In section 5.3.2.2 it is shown, that fitting with 2 and 4 Gaussians does not result in consistent I(D)/I(G) values for an annealing series of a-C. Therefore, in this work the mentioned combination of linear background, BWF and Lorentzian was used for quantitative analysis of the spectra.

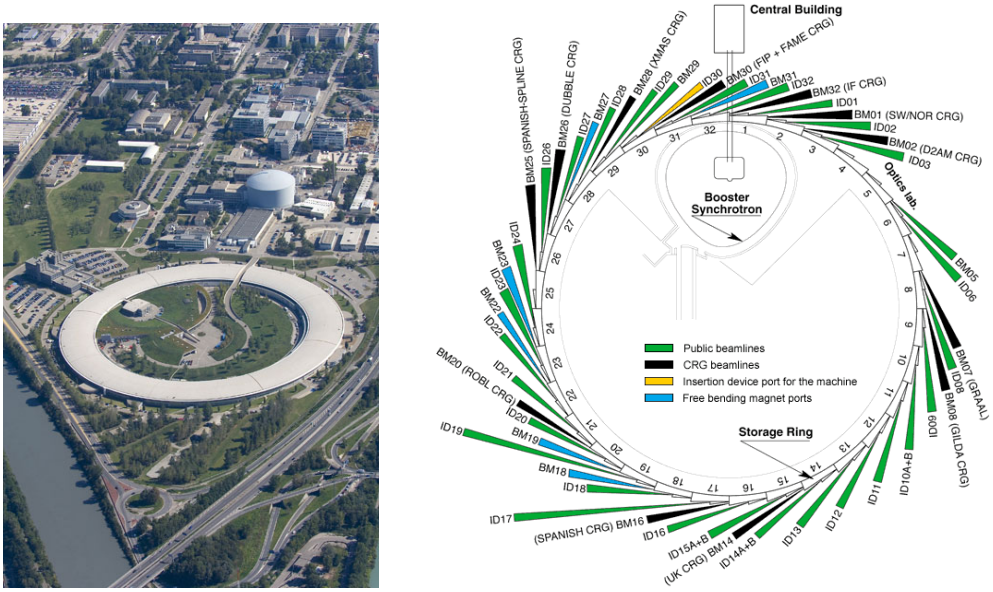

Figure 2.5: *The European Synchrotron Radiation Facility, ESRF, in Grenoble (France). On the right side a schematic of the storage ring with all beamlines is shown. Picture by Denis Morel, courtesy of ESRF.*

2.3 Investigations with synchrotron radiation

Some advanced characterization techniques are only feasible at synchrotron sites. Charged particles (today usually electrons) are accelerated in a large UHV storage ring to several GeV. When moving in a closed loop near the speed of light, they emit synchrotron radiation, ranging from IR to hard X-rays. The intensity and brilliance of the produced light is several orders of magnitude higher compared to conventional X-ray sources. Fig. 2.5 shows an aerial view of the ESRF synchrotron facility and the arrangement of the beamlines.

In former storage rings only radiation from bending magnets was utilized, keeping the electrons on circular motion. Nowadays, synchrotrons also employ insertion devices like undulators. In an undulator, a set of dipol magnets is alternately oriented along the beam, leading to an additional sinusoidal motion of the electrons. By radiation interference the undulator provides a very high photon flux and brilliance in a narrow radiation spectrum.

This work included XAFS measurements at HASYLAB in Hamburg, NEXAFS/XES investigations at ESRF in Grenoble (France) and NEXAFS/XPS measurements at SRS in Daresbury (UK).

2.3.1 X-ray absorption fine structure (XAFS)

X-ray absorption fine structure (XAFS) is the general term for investigations dealing with the analysis of modulations in the region of the X-ray absorption edge [68,69]. XAFS spectra are acquired by scanning the photon energy above the absorption edge of a chosen element and detecting the absorption coefficient $\mu(E)$. This is usually done by using synchrotron radiation and a monochromator. If the region of interest is only around the edge ($\approx$50 eV), the term NEXAFS (near edge X-ray absorption fine structure) or XANES (X-ray absorption near edge structure) is used. If the energy range covers $\approx$1000 eV above the edge, an EXAFS (extended

X-ray absorption fine structure) spectrum is obtained. Fig. 2.6a shows a XAFS spectrum of TiC with NEXAFS and EXAFS part.

The absorption coefficient $\mu(E)$ can be measured in transmission mode by detecting the incoming (I_0) and transmitted (I) intensity: $\mu(E) = ln(I_0/I)$. The emitted fluoresecence light (I_f) can also be used: $\mu(E) \sim I_f/I$. Fluorescence radiation is associated with the filling of the created core-hole by an electron from a higher energy level (see below).

XAFS is sensitive to the local atomic environment of the excited atom. A NEXAFS spectrum easily reveals the oxidation state, and provides information about the local coordination symmetry, but the theoretical description is challenging and still under development. The EXAFS part of the spectrum can be handeled by a well-developed theory and used to gain information about the nature of next neighbors, their coordination numbers and distances to the absorbing atom.

The important fact which makes XAFS usefull for many applications is, that no crystallinity or any long-range order is required. Therefore, XAFS can be applied for disordered and amorphous solid systems, but also for molecules or clusters in liquid and gas phase. By choosing the absorption edge it is element specific, which reduces sample preparation.

2.3.1.1 EXAFS

The basic process of EXAFS starts with the absorption of a photon which has enough energy to eject a core electron (K or L shell), creating a core hole in the atom [68,70]. The difference between the photon energy and the electron's binding energy determines the kinetic energy of the ejected photoelectron. In quantum mechanics the photoelectron is regarded as a spherical wave leaving the absorbing atom. This wave is backscattered at the surrounding atoms as shown schematically in Fig. 2.6b. Depending on their relative phase, constructive or destructive interference of the backscattered with the outgoing wave occurs, modifying the amplitude of the photoelectron wave function. This leads to a change of the X-ray absorption probability at the absorbing atom. Since the photon energy is continuously increased, the photoelectron wavelength is changing and so the phase difference, thus causing maxima and minima in the EXAFS spectrum. It is clear that the distance to the scattering atom, the atomic number and the coordination number is reflected in the EXAFS.

To extract the oscillations above the absorption edge ($\chi(E)$, "the EXAFS"), a smooth background function $\mu_0(E)$ (representing the absorption of an isolated atom) is subtracted from the spectrum followed by a normalization to the edge step $\Delta\mu_0(E_0)$ at the threshold energy E_0:

$$\chi(E) = \frac{\mu(E) - \mu_0(E)}{\Delta\mu_0(E_0)} \tag{2.6}$$

The energy scale is usually changed from the photon energy E (eV) to k, the wave number of the photoelectron, given in Å^{-1}:

$$k = \sqrt{\frac{2m_e(E - E_0)}{\hbar^2}} \tag{2.7}$$

with E_0 the edge energy and m_e the electron mass.

Fig. 2.7a presents the extracted EXAFS $k^2\chi(k)$ from the spectrum in Fig. 2.6a. Multiplication of $\chi(k)$ with k^2 (also k or k^3 are common) is usually performed to enhance the oscillations at higher energies due to the fast decay of $\chi(k)$ with k.

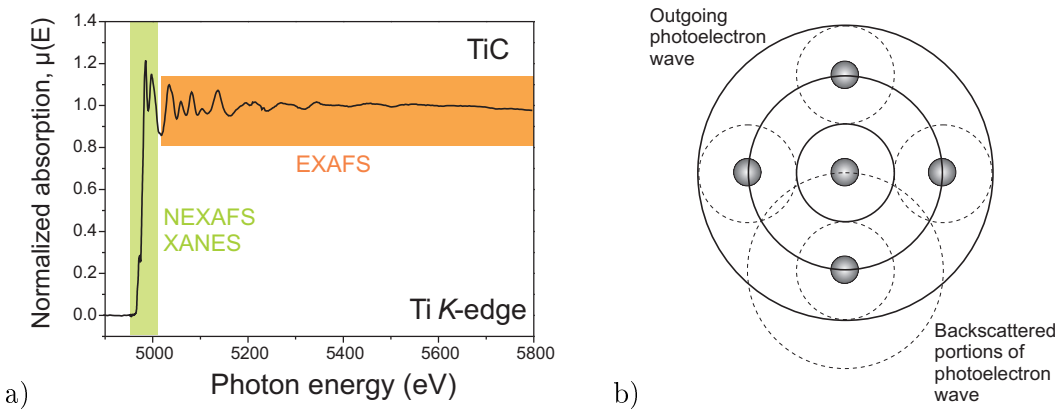

a) b)

Figure 2.6: *a) Ti* K*-edge XAFS spectrum of TiC, with NEXAFS and EXAFS regions. b) Schematic of the radial part of the photoelectron wave. The solid circles represent the outgoing wave, the dashed circles the backscattered portion. The absorption probability of X-rays at the absorbing atom is proportional to the amplitude of the backscattered wave.*

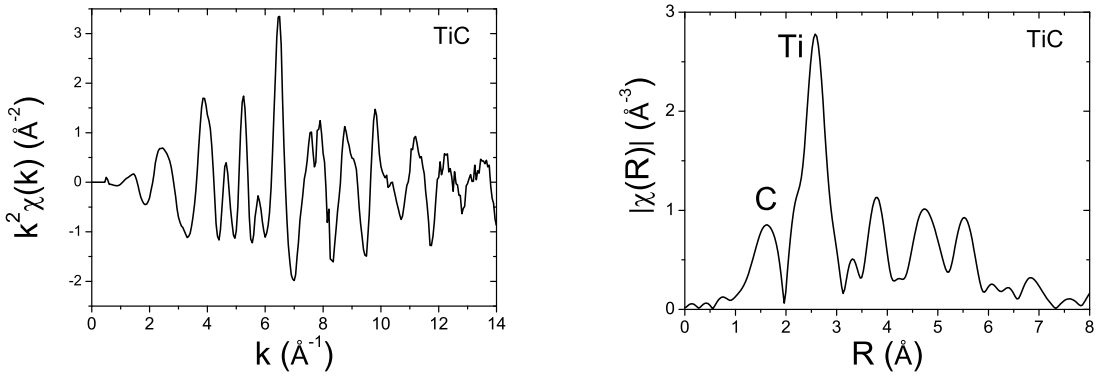

a) b)

Figure 2.7: *a) Extracted EXAFS, $k^2\chi(k)$, from the spectrum in Fig. 2.6a. It is weighted with k^2 to enhance oscillations at higher k. b) After Fourier transformation, the data is presented as $|\chi(R)|$ in realspace R, given in Å. The first two coordination shells from a Ti atom in TiC are C and Ti, as indicated.*

Since the photoelectron scatters back also from beyond the adjacent atoms, $\chi(k)$ is a sum over several next neighbors. They are grouped in symmetric *coordination shells* of one atomic species, surrounding the absorbing atom.

As derived in [68], $\chi(k)$ can be analytically described in a simple description as

$$\chi(k) = \sum_j \frac{N_j e^{-2k^2\sigma_j^2} e^{\frac{-2R_j}{\lambda(k)}} f_j(k)}{kR_j^2} sin[2kR_j + \delta_j(k)] \tag{2.8}$$

For every coordination shell j, N gives the coordination number and σ^2 the mean-square displacement (also called Debye-Waller factor) in bond distance R. $f(k)$ is the scattering amplitude and $\delta(k)$ the phase shift of the atom which determines the coordination shell. To account for inelastic scattering of the photoelectron and the finite lifetime of the core hole, a damped spherical wave is used with $\lambda(k)$ as the mean free path of the photoelectron.

The pure local sensitivity (only several Å) of EXAFS is evident when considering that $\chi(k)$ is proportional to $\frac{1}{R^2}$, and the influence of $\lambda(k)$. The different distances of each coordination shell result in different frequencies building up $\chi(k)$. They can be extracted using Fourier transformation and the EXAFS is transferred into real space R, given in Å. Usually, the magnitude of the resulting complex function is shown, as presented in Fig. 2.7b. The first two maxima show the first (C) and second (Ti) coordination shells of a titanium atom in TiC. Due to the scattering phase shift $\chi(R)$ is shifted ≈0.5 Å to lower distances than the real distances in TiC.

By quantitative analysis of the EXAFS data it is possible to derive values for R, N and σ^2. For that the scattering properties $\delta(k)$ and $f(k)$ of each coordination shell has to be known. They can be calculated with programs like FEFF [71].

2.3.1.2 NEXAFS

The physical description of the NEXAFS part of an XAFS spectrum can not be explained in the simple way as for the EXAFS part [72, 73]. Close above the absorption edge, the ejected photoelectron has an energy of only a few eV. Therefore, its wavelength is larger than the inter-atomic distances and multiple scattering effects (which are neglected for the simple EXAFS interpretation) become dominant. Even below the ionization threshold absorption occurs. Here, the electron can be promoted into unoccupied valence states (molecular orbitals, MO's), showing specific symmetry depending on the type of bonding. This is schematically shown for a diatomic molecule in Fig. 2.8a [72].

For carbon materials, the K-edge NEXAFS spectrum is dominated by transitions into σ^* and π^* anti-bonding MO's, as shown for graphite in Fig. 2.8b. The π^* MO is only present if the carbon atom forms π bonds which is the case in double (and triple) bonds, i.e. carbon in sp^2 (and sp) hybridization. Carbon in all bonding configurations exhibit unoccupied σ^* MO. Since the characteristic resonance at 285.5 eV directly reflects the presence of C=C bonds, it can be used to estimate the sp^2 content of carbon materials.

For that purpose, the area below the π^* peak is normalized with the area of a large fraction of the spectrum in the σ^* region. The value for graphite is used as standard because it has virtually 100 % sp^2 bonded carbon. By comparison with graphite (and if C≡C bonds can be excluded, as in the case of a-C), the sp^2 fraction of an unknown carbon material can be determined [56, 66].

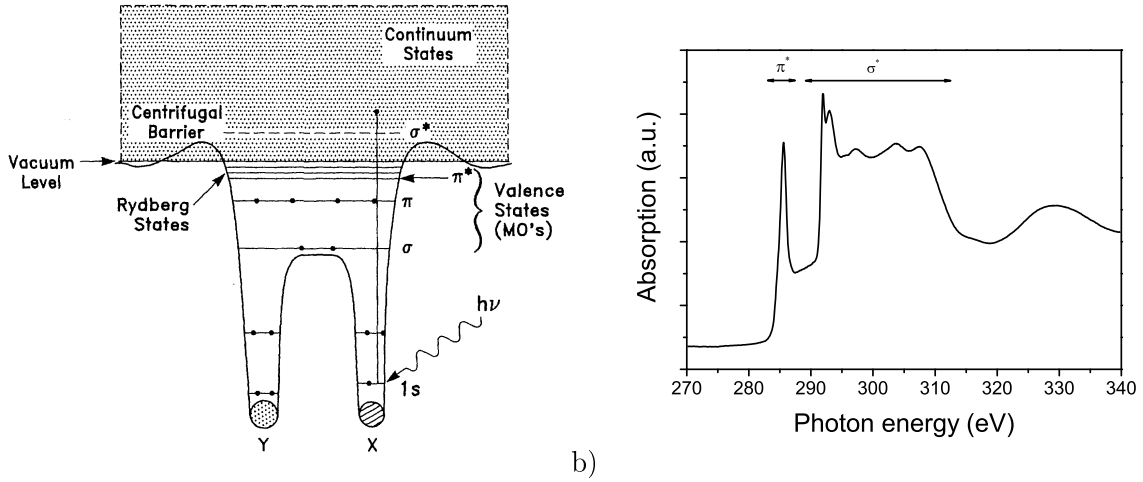

Figure 2.8: *a) Schematic representation of the potential of a diatomic molecule and possible transitions for a 1s electron. Unfilled states are labeled with *. Taken from [72]. b) Carbon K-edge NEXAFS spectrum of graphite. The regions for π^* and σ^* transitions are indicated.*

Due to the low energy of the carbon K-edge, the measurements have to be performed in UHV conditions, and usually electron yield detection is applied. In the case of *total electron yield* (TEY), simply the sample drain current is measured. This includes all electrons escaping from the material, i.e. Auger and photo electrons. In contrast to measurements using transmission or fluorescence detection, TEY is surface sensitive ($\approx$5 nm for carbon) due to the low electron mean free path in matter.

2.3.2 X-ray emission spectroscopy (XES)

The creation of a photoelectron, which leaves a core-hole in the atom, is the basic process of EXAFS and NEXAFS beyond the ionization threshold. The fluorescence radiation, emitted due to filling of the core-hole, can be used to measure XAFS spectra. In Fig. 2.9a the possible fluorescence decays of a 1s core-hole (K shell) are schematically shown in detail for transition metal compounds. Fig. 2.9b illustrates the respective fluorescence lines (*emission lines*) exemplarily for MnO [74]. For the purpose of XAFS measurements, usually the most intense $K\alpha$ lines are used. In the case of transition metals this means filling of the 1s core-hole by a 2p electron – with 2 possible spin orientations.

There exist also other decay channels at higher fluorescence energies but lower probability as depicted in Fig. 2.9. The $K\beta$ main lines are due to filling of the core-hole by 3p electrons, and have $\approx$8 times lower intensity. About further 50 to 100 times weaker are the so-called $K\beta$ satellite lines, which include transitions from higher (valence) orbitals. They show high sensitivity to the chemical environment and comprise the $K\beta_{2,5}$ line, directly below the Fermi level, and the $K\beta''$ (or *cross-over*) peak. The $K\beta_{2,5}$ line results from filling of the 1s vacancy by transition metal 4p electrons and ligand[1] 2p or 3p electrons. The $K\beta''$ peak is due to a ligand 2s to metal 1s cross-over transition. This transition is not dipole forbidden, since orbitals of different atoms are involved. In a study by Bergmann et al. [75], a decreasing

[1]The term *ligand* (from Latin ligare – to bond) has its origin in organo-metallic complex chemistry but is here also used to denote the neighboring atom of a transition metal in solid state materials.

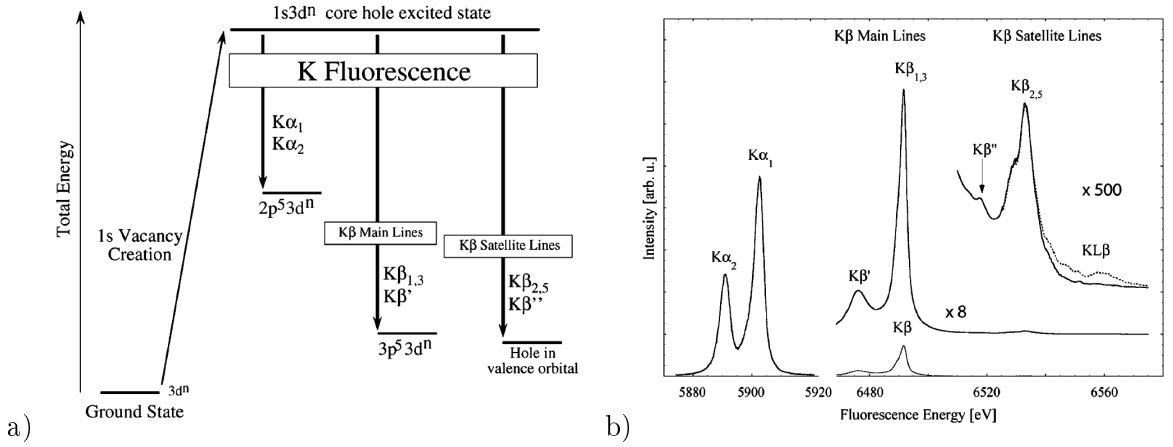

Figure 2.9: *a) Energy scheme for different* K *fluorescence channels following the creation of a 1s core hole. b) Different* K *fluorescence emission lines observed for MnO. The KLβ line is due to a double (1s, 2p) ionization. Both pictures are taken from [74].*

$K\beta''$ peak position for N, O and F ligands was shown for Mn compounds. Additionally, the Mn-ligand distance was reflected in the $K\beta''$ intensity.

This ligand sensitivity of the $K\beta''$ peak position gives an valuable additional information, since elements with similar atomic number can be hardly distinguished with EXAFS. By using X-ray fluorescence light, it is a bulk sensitive technique, thus surface contaminations can be neglected (in contrast to XPS).

Since conventional solid state fluorescence detectors used to detect K shell fluorescence have an energy resolution of $E/\Delta E \approx 40$, the satellite lines can usually not be resolved on standard XAFS beamlines. This is only possible when the emitted fluorescence light is spectroscopically analyzed utilizing the Bragg reflection of single-crystals. Therefore, the term X-ray emission spectroscopy (XES) was introduced for such measurements, which are only possible at a small number of synchrotron beamlines (e.g. ID26 at ESRF).

2.3.3 X-ray photoemission spectroscopy (XPS)

X-ray photoemission spectroscopy (XPS) is a widely used technique to investigate surfaces in respect to composition and chemical state [47]. A core electron is ejected by X-rays, creating a photoelectron and a core-hole. The kinetic energy of the photoelectron is given by

$$E_{kin} = h\nu - E_B - \Phi_S \tag{2.9}$$

with $h\nu$ the photon energy, Φ_S the (almost constant) work function, and E_B the binding energy of the K-shell electron. By means of an electron analyzer the photoelectrons are detected as function of energy (usually E_B instead of E_{kin} is given on the x-axis of a XPS spectrum).

Since the binding energy of the core level is unique for every atom, elemental analysis is possible. The sensitivity of E_B on the chemical surrounding leads to a *chemical shift* in the photoemission spectrum. Therefore, the chemical state can be determined.

Beamlines for measuring carbon K-edge NEXAFS spectra are usually equipped with an electron analyzer for detecting the ejected photoelectrons. In contrast to conventional XPS

systems, where X-ray radiation of fixed wavelength is applied, the excitation energy can be adjusted by means of a monochromator (grating).

XPS is a surface sensitive technique, due to the low mean free path of the photoelectrons. Seah and Dench [76] published the "universal curve" for the inelastic mean free path of electrons in matter. Depending on the element it shows a minimum at 0.1-0.8 nm around 30-100 eV. Therefore, by choosing different excitation energies in a synchrotron XPS experiment, the information depth is changed, due to the different E_{kin}.

Thanks to the high photon flux provided by a synchrotron beamline, measurement time for XPS spectra can be significantly lower compared to conventional XPS systems. A drawback is the influence of monochromator misalignment which results in peak shifts in the photoemission spectra. For an exact energy scale a calibration has to be performed after every monochromator movement.

2.4 Rutherford backscattering spectroscopy (RBS)

Rutherford backscattering spectroscopy (RBS) is a fast and simple method to determine composition of thin films depth-resolved [47, 77, 78]. For that purpose a monoenergetic MeV ion beam of light atoms (typically He^+or H^+at 0.5-4 MeV) is created by an accelerator and directed to the sample surface. The particles backscatter at the nuclei of atoms in the surface near region and transfer a fraction of the energy to the target atom. The number and energy distribution of the backscattered ions are detected by an analyzer.

The energy ratio of an ion before (E_0) and after (E_1) a scattering event depends only on the masses of projectile and target atom (M_1, M_2) and the scattering angle θ. It can be derived from the binary collision theory [77]:

$$\frac{E_1}{E_0} = \left[\frac{\left(M_2^2 - M_1^2 sin^2\theta\right)^{1/2} + M_1 cos\theta}{M_2 + M_1}\right]^2 \tag{2.10}$$

Therefore, the target element can be easily identified. This equation is only valid for scattering at the outermost surface, but the ion beam penetrates the target and scattering occurs also from deeper atoms. During traveling through matter, the projectile looses energy due to excitation and ionization of electrons. This electronic energy loss $\frac{dE}{dx}$ is called stopping power and leads to peak broadening in a RBS spectrum, which delivers the depth information. Fig. 2.10 shows a spectrum which occurs for a 7.5 % a-C:Ti film. The atomic mass difference leads to different elemental signal positions, whereas the thickness of 880 nm leads to peak broadening. The different atomic species and their (atomic) concentrations as well as the layer thickness (more exactly the *area density* in at cm^{-2}) of the film is generally determined by fitting a theoretical spectrum to the measured data. This can be performed by programs like SIMNRA [79].

It is important to note, that RBS is an absolute method which requires no standards (despite an energy calibration). It has a very high accuracy with typical uncertainties of ±3% for areal densities and less than 1 % for stoichometric ratios. On the other hand, the method is limited to thin films of only a few µm, and roughness can influence depth resolution. By decreasing the ion energy (e.g. 500 keV $^4He^+$) a depth resolution in the nm range can be achieved for the surface-near region. Also overlapping of signals from different elements can be problematic. For example, the oxygen content can not be detected with films on Si substrate (but on graphite), which is evident in Fig. 2.10.

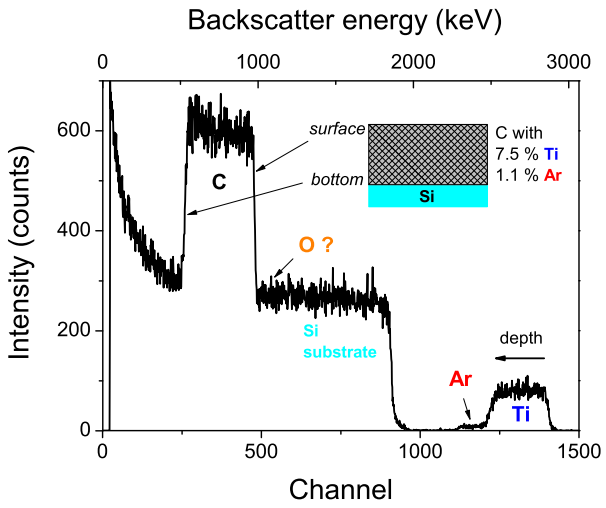

Figure 2.10: *4 MeV $^4He^+$ RBS spectrum of a 7.5 % a-C:Ti film on Si substrate. The energy loss due to different target atoms and the electronic loss due to scattering in different depths results in broad signals at different backscattering energies. Signals from the surface and heavier atoms appear at higher energies. The layer thickness (in at cm^{-2}) and C, Ti and Ar content (in at%) can be determined with high accuracy from this spectrum. The oxygen signal is superimposed by the high Si background.*

2.5 Magnetron sputtering

Thin film production by physical vapor deposition (PVD) is of high technological relevance in many industrial sectors like the production of hard and wear resistant coatings, diffusion barriers, optical films and in semi-conductor applications. PVD – generally applied in vacuum – is based on the production of a vapor by physical processes and the subsequent condensation as thin film on a substrate [80]. The two most important methods producing a vapor are evaporation and sputtering. Whereas evaporation transfers the atoms thermally into the gas phase, in sputtering they are ejected by ion impact [81].

Sputter deposition of materials is based on the plasma-assisted production of ions (usually Ar) which bombard a target, acting as cathode of the plasma discharge. As a result of ion bombardment, target atoms are ejected (*sputtered*) and deposit on the substrate, thus forming a thin film. Details of the underlying processes (*collision cascades*), leading to a sputtered surface atom can be found in [82]. Pure DC and RF sputtering, where the plasma is simply created by a DC or RF discharge, suffer from low deposition rates due to low Ar ionization in the plasma. The magnetron sputter arrangement, developed in the 1970s, is the most common one and offers higher deposition rates.

In Fig. 2.11a the effect of a planar magnetron setup is shown. A magnetic field is created by a set of permanent magnets, placed behind the target, providing a ring-shaped magnetic field. It is oriented parallel to the target surface and perpendicular to the electric field. Secondary electrons, created by the impacting ions, are concentrated with cycloidal motion above the target ("race track"). This leads to a high plasma density near the target, resulting in increased Ar ionization and enhanced ion bombardment. Fig. 2.11b shows the circular erosion

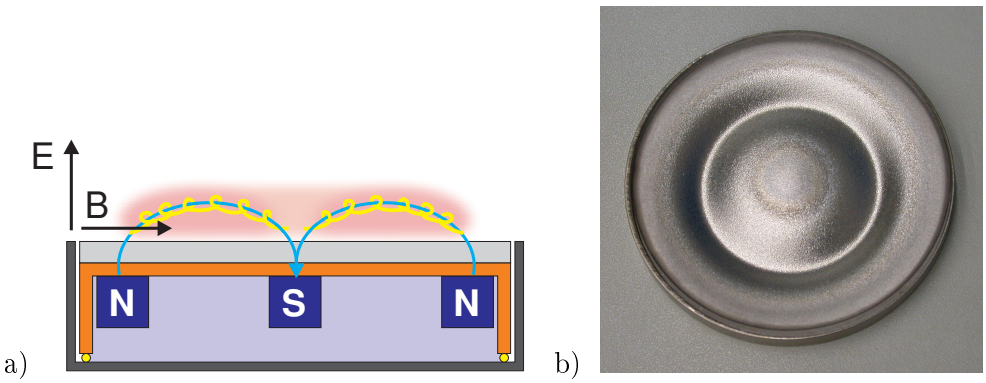

Figure 2.11: *a) Schematic cross section of a planar magnetron. Electrons are trapped in cyclic motion near the target surface, leading to a higher plasma density and therefore higher sputtering rates. Taken from [81]. b) Ring-like erosion track on a Ti sputter target.*

track produced by the magnetically confined plasma. The magnetron configuration can be used with DC and RF discharges and leads to much higher deposition rates. Thanks to the increased plasma density, depositions can be performed at lower pressures, which increase film quality.

The sputtered atoms – mainly neutral atoms are ejected – have a broad energy distribution, that peaks at a few eV, approximately half the surface binding energy [83]. Influence on the film properties is possible by varying Ar pressure, deposition temperature and a substrate bias voltage, which results in sputtering during layer growth. Additional energy of several eV is deposited on the film surface by reflected Ar ions from the cathodes which also leads to a small amount of implanted Ar in the film (1-2 at%).

Chapter 3

Background knowledge

In this chapter background information is given about the structure of amorphous carbon films and the mechanisms behind carbon erosion by hydrogen isotopes.

3.1 Structure of amorphous carbon films

In the last decades, amorphous carbon films have attached great attention, due to their superior properties in respect to hardness, tribology, optics and chemical resistance [84]. It is related to the exceptional characteristic of carbon to occur in different hybridization states, forming carbon-carbon single, double and triple bonds. Graphite (only sp^2 bonded carbon) and diamond (only sp^3 bonded carbon) are two stable carbon allotropes exhibiting very different physical properties. Amorphous carbon consists of varying fractions of both bonding types (in most carbon materials triple bonds do not have significant contribution) and can also contain hydrogen.

In contrast to a simple consideration, the structure of amorphous carbon is not just a "mixture" of graphite and diamond. A new material with new properties is observed, and due to the lack of order, experimental approaches are challenging [52]. Therefore, and due to the fact that a large variety exists for amorphous carbon, the discussion about its structure is yet lively [67,85,86]. A still accepted conception was introduced by Robertson and O'Reilly [87]. They claim that clusters of a sp^2 phase consisting of distorted condensed aromatic rings are interconnected by a random sp^3 bonded carbon network. Also concepts about full sp^2-bonded hard amorphous carbon films were published [88]. Methods used for characterization of amorphous carbon are summarized in [89].

Much confusion exist about various terms for different kinds of amorphous carbon. Depending on the preparation conditions they show strong variations in respect to structural properties. The VDI guideline 2840 [90] classifies all common types of amorphous carbon films and gives recommendations for the preferred acronyms. Following this guideline, hydrogen-free carbon films with high sp^2 content prepared by PVD are denoted **a-C**; in the case of metal-containing a-C the term **a-C:Me** should be used.

In 1987, the first paper about the production of metal-doped carbon films was published by Dimigen et al. [91]. They prepared hydrogenated amorphous carbon films (a-C:H) containing Ru, Ta and W by reactive sputtering and reported about improved tribological properties and adhesion. Generally, metal-doping leads to reduced film stress and higher electrical conductivity [92]. Also hardness and wear-resistance can be increased [42,44,93,94]. For such

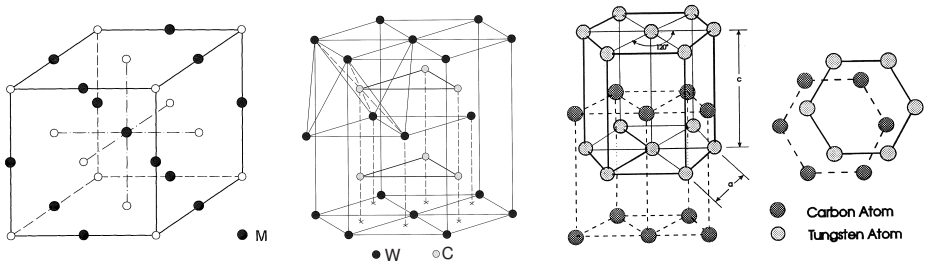

Figure 3.1: *Crystal structures of Ti, V, Zr and W carbides, relevant for this work. Taken from [102, 103].*

applications the formation of a nanocomposite of metal-containing particles in the amorphous carbon matrix is preferable. Therefore, most research concentrated on production of such nanocomposites, often achieved by an elevated substrate temperature or application of a bias voltage.

In recent years several groups studied the structure of metal-containing carbon films – mainly using Ti as dopant – with a focus on the bonding environment of the metal. [95–101]. They generally observe the formation of nm-sized TiC crystallites embedded in a matrix of (hydrogenated) amorphous carbon. Nevertheless, for low metal contents, the metal does not form carbide crystals detectable by XRD or TEM, and it is distributed in an amorphous state in the carbon matrix.

Here, it is important to note, that the assignment with "TiC" does not mean, that a carbide phase with 1:1 stoichometry is formed. In fact, the crystal structure of fcc TiC (which is a interstitial carbide with carbon in the octahedral sites) facilitates different carbon contents in a homogeneity interval from $TiC_{0.48}$-$TiC_{1.00}$ [102]. These variations in the carbon content slightly changes the lattice constant. Nevertheless, this differences are usually not resolved in experiments, which is also not the case for investigations presented in chapter 5. In this work the term "TiC" is used for convenience, although "TiC_{1-x}" would be more accurate. This is also the case for the fcc phases VC ($VC_{0.65}$-$VC_{0.875}$) and ZrC ($ZrC_{0.6}$-$ZrC_{0.98}$) [102]. For tungsten carbides the situation is different. Whereas the crystal structure of hexagonal WC (carbon in trigonal prismatic sites) does not show deficient C atoms, the carbon content in hcp W_2C (carbon in half of octahedral sites) can vary. For the W-C system, also the formation of the fcc phase WC_{1-x} can occur, which can be described similar to the TiC structure. Fig. 3.1 summarizes the structures of metal-carbides relevant for this work.

3.2 Erosion of carbon by hydrogen

Bombardment of carbon with hydrogen species leads to erosion of carbon below the physical sputtering threshold due to chemical reactivity. A comprehensive review about this issue was recently published by Jacob and Roth in [104], from which basic information is given in this section. Following their recommended definitions, two chemical processes have to be distinguished:

1. **Chemical erosion** – chemical reactions due to neutral, thermal species.
2. **Chemical sputtering** – "a process whereby ion bombardment causes or allows a chemical reaction to occur which produces a particle that is weakly bound to the surface and hence easily desorbed into the gas phase" [105].

It is important to note that in the case of hydrogen ion bombardment both processes contribute to erosion, and confusion exists about the general term for erosion by hydrogen ions. Many authors use the term *chemical erosion* for the case of hydrogen ion bombardment, even if the dominating process is due to ion impact, i.e. chemical sputtering. In this work, in both plasma and ion beam erosion experiments energetic hydrogen ions are the reactive species. Therefore, the term chemical sputtering is used throughout the text. Chemical erosion and chemical sputtering are briefly described below.

Before, it is important to introduce the term *erosion yield* Y, in which carbon erosion is generally described. It is defined as the ratio of removed carbon atoms divided by the number of impacting hydrogen atoms or ions. The erosion yield can be determined by measuring the total amount of removed carbon, e.g. by weight-loss or ellipsometry. Then, the *total erosion yield* is determined. Mass spectrometry can be used to determine volatile erosion species and quantify the erosion. Nevertheless, high experimental effort has to be driven to quantify all erosion products correctly, especially in the case of highly reactive or highly sticking species. Only when using a molecular-beam mass spectrometer, total erosion yields can be determined by capture of all erosion species. The signal of a mass spectrometer in usual line-of-sight configuration is dominated by the gas atmosphere, i.e. stable species that survived wall collisions. When quantifying only one species (e.g. CH_4) by mass spectrometry, usually the term *CH_4 production yield* is used.

3.2.1 Chemical erosion

Chemical erosion of carbon by atomic hydrogen is a thermally activated process and does not require energetic species. The individual steps of the reaction was described by Küppers et al. [106,107]. The authors characterize the process as an erosion cycle including four individual steps as shown in Fig. 3.2. On the left side, the sp^2 carbon atoms are hydrogenated to sp^3 sites, including an intermediate radical stage sp^x. Further addition of hydrogen can lead to hydrogen formation, leaving a radical center (right side). A thermally activated process (T $>$400 K) can lead to desorption of hydrocarbon (e.g. methyl) species in the neighborhood of a sp^x site and restoring a C=C bond (sp^2). At temperatures $>$600 K, the recombination of incoming hydrogen with bonded hydrogen becomes dominant (left side). This leads to less sp^3 sites, and therefore to a decrease of the chemical erosion. Hence, the chemical erosion yield exhibits a temperature-maximum around 600 K. Hydrocarbon complexes can also directly desorb at temperatures $>$600 K (arrow in center of Fig. 3.2). In the described model, the main erosion species is CH_3, but also CH_4, C_2H_x and C_3H_x species were detected by mass spectrometry [108–110]. Also the carbon structure influences the product spectrum [111,112].

3.2.2 Chemical sputtering

Chemical sputtering appears, when energetic species lead to erosion. Generally, energetic species can be chemically inert (e.g. noble gas ions) or chemically reactive (e.g. hydrogen or oxygen ions). In the first case, also atomic hydrogen is required to form the volatile reaction

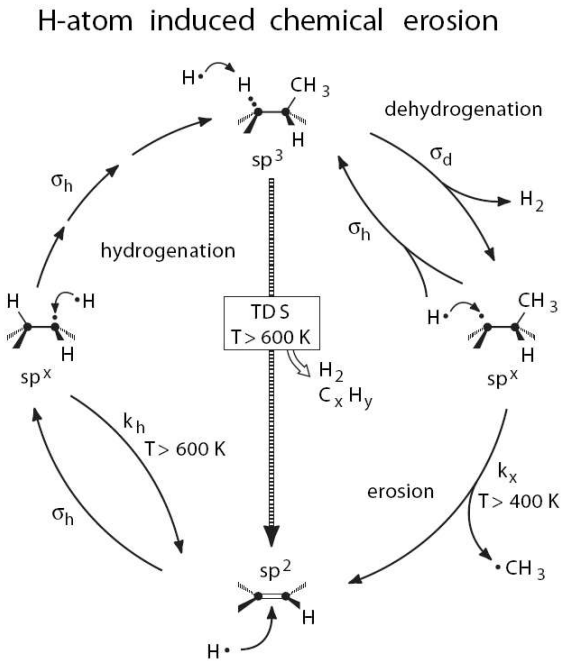

Figure 3.2: *Chemical erosion cycle as described in [106, 107]. The process starts with the attack of a carbon double bond (sp^2 site) by atomic hydrogen (bottom). The picture is taken from [104] .*

products. Only the case of energetic hydrogen ions is discussed here. Carbon erosion due to chemical sputtering is temperature dependend and shows a maximum at T_{max} of around 800 K. The chemical sputtering yield depends on the ion energy, as shown in Fig. 3.3 for D bombardment of different carbon materials at RT and T_{max}. The solid line describes erosion due to physical sputtering. The contribution of different erosion species also varies with energy [110, 113, 114], with CH_4 as the main reaction product. Recent measurements showed that for energies below 50 eV higher hydrocarbon species are dominating [115, 116].

An empirical, analytical description of chemical sputtering was proposed by Roth and Garcia-Rosales [118,119]. It is based on the assumption that energetic ions are slowed down by mainly kinematic interaction with carbon atoms, leading to ion damage. A chemical reaction with carbon only appears for the slow, thermalized hydrogen ions which can be described by the chemical erosion mechanism developed by Küppers et al. [106,107] for atomic hydrogen (see Fig. 3.2). The proposed formula describes the total erosion yield Y_{tot} by a) physical sputtering Y_{phys}, b) a chemical erosion term, including effects of radiation damage, Y_{therm} and c) a low-temperature near-surface process Y_{surf}. The last term can be regarded as physical sputtering of weakly bound sp^3-CH_n, groups from the surface (corresponding to the state on top of Fig. 3.2). Y_{therm} is only active at temperatures above 400 K and exhibits a maximum between 600 and 900 K, depending on hydrogen isotope, flux, ion energy, and radiation damage. Y_{surf} is dominant at lower temperatures and low ion energies. With the formula proposed by Roth and Garcia-Rosales [118, 119], the influence of temperature, energy, flux on the total erosion yield can be well described, and also the isotope dependence is reproduced.

Recently, Hopf et al. [120] proposed a microscopic model for chemical sputtering for the case of energetic argon ions and atomic hydrogen. In 2005 it was adapted to the case of graphite bombardment with hydrogen ions [121]. It is assumed that the incoming ions break

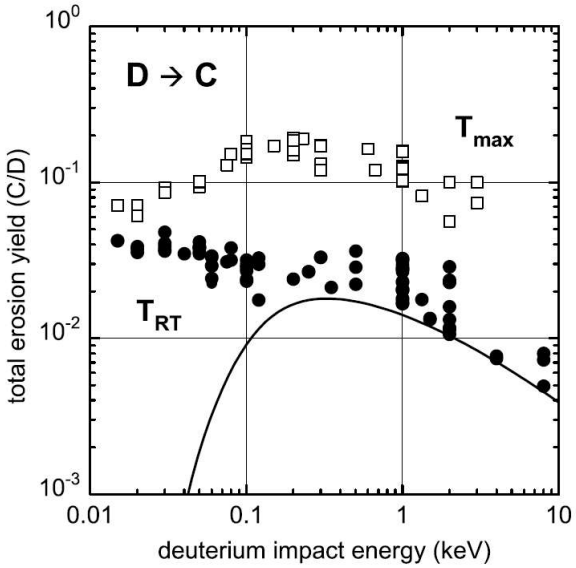

Figure 3.3: *Energy dependence of the total erosion yield for bombardment of carbon with D at RT and T_{max}. T_{max} is the temperature where maximum erosion occurs at a given D energy. The solid line gives the physical sputtering contribution. Taken from [117].*

C–C bonds. Locally available hydrogen reacts with the broken bonds, forming a C–H bond. This leads to formation of stable, volatile hydrocarbon molecules, which diffuse to the surface and desorb in the gas phase. The model agrees well with experimental data.

3.2.3 Doping of carbon

Doping of carbon leads to a reduction of the chemical sputtering yield. A review about the influence of different dopants on the carbon erosion process was published by Balden [20]. Already in the 1980s the effect of metallic surface impurities was investigated [122]. In recent years, mainly doped graphites (B, Si, Ti, W, introduced as carbides) were used as target material [21,33–35,123–125]. The most pronounced effect on suppressing chemical sputtering was observed with B doping. [36, 126]. Even small amounts of B lead to a decrease of the erosion yield and a shift of T_{max} to lower temperatures. In terms of the model proposed by Roth and Garcia-Rosales, the effect of B doping is explained by an influence on the regime Y_{therm}. The dopant lead to a reduction of the activation energy for hydrogen desorption E_{Hrel} from 1.8 eV (pure graphite) to 1.2 eV (B-doped graphite). Therefore, the concentration of sp^x states is reduced (reaction from sp^x to sp^2, left side of Fig. 3.2) and the erosion cycle is interrupted. It is clear, that the lowering of E_{Hrel} is dependent on the type of dopant. For doping with Si, Ti and W, E_{rel} was found to be 1.5 eV [123]. For erosion of doped carbon materials, an additional influence on the total erosion yield is evident due to preferential erosion of carbon and dopant enrichment at the surface. A typical erosion morphology evolves for doped graphites, where exposed carbide grains protect the underlying carbon from further erosion [20,33,124,127].

Chapter 4

Experimental details

In this chapter experimental details of specimen preparation, characterization and erosion experiments are presented.

4.1 Specimens

4.1.1 a-C and a-C:Me film preparation

Different substrate materials were used for film deposition: Si wafer (polished, (100) orientation, 0.5 mm thickness) and pyrolytic graphite (polished, grade HPG, parallel orientation of the graphitic layers with 20 ° mosaic spread, ≈1 mm thickness). All substrates were ultrasonically cleaned in isopropanol for 3 minutes.

The a-C and a-C:Me films (Me = Ti, V, W, Zr) were produced by magnetron sputter deposition (Discovery 18, Denton Vacuum) using argon (99.999 %) as sputtering gas. A graphite target (99.999 %) was installed at cathode 1 and operated in RF mode. The metal targets (Ti 99.6 %, V 99.5 %, W 99.95%, Zr 99.2 %) were sputtered in DC mode at cathode 2. Before deposition, the substrates were etched by an argon plasma for 2 minutes (100 W, 550-600 V bias) to remove the oxide layer and adsorbed species. Subsequently, the sputter targets were cleaned by operation with closed shutters for 2 minutes (≈350 V). All depositions were performed without external heating. The sample temperature did not exceed 350 K during film deposition. No substrate bias voltage was applied and the substrate holder was rotating at 10 rpm during deposition and etching. The deposition chamber was pumped by a turbo molecular pump, by means of a liquid nitrogen trap a base pressure of $\approx 5 \cdot 10^{-5}$ Pa was achieved. During sputter deposition 20 sccm Ar lead to a pressure of $\approx 1 \cdot 10^{-1}$ Pa. The film thickness varied between ≈0.7 and 1.5 µm (Tab. 5.1) and was measured by a profilometer (alpha-step 200, Tencor) on a sample on which a line of ink was drawn before deposition. Due to low adhesion the layer could be removed, generating a step with a height of the film thickness.

Multilayer films were produced with an a-C:Me layer (≈300 nm) between two a-C layers (≈300 nm at the substrate side and ≈200 nm to the surface). This was realized by sputtering continuously the graphite target and operating the metal target only for the a-C:Me layer.

Annealing of the samples after deposition was performed in vacuum at 700, 900 and 1100 K (oven MOMO, base pressure $\leq 5 \cdot 10^{-4}$ Pa, during heating $\leq 2 \cdot 10^{-3}$ Pa) and 1300 K (experiment TESS, base pressure $\approx 1 \cdot 10^{-5}$ Pa, during heating $\approx 1 \cdot 10^{-4}$Pa) for 15 minutes. In both ovens the temperature was measured by thermocouples near the sample. Some samples were annealed in the chamber of the high current ion source experiment (section 4.3.1).

4.1.2 Graphites and CFC

Graphite and CFC materials were produced in the frame of the ExtreMat project from Spanish research institutes and were investigated in this work in respect to D erosion resistance.

Fine-grain graphites (Ti-doped and undoped) were supplied by the *Centro de Estudios e Investigaciones Técnicas de Gipuzkoa (CEIT)* in San Sebastian. A mesophase pitch was doped with 130 nm TiC powder and after uni-axial molding subjected to cold isostatic pressing. Carbonization and graphitization at >3000 K gave the final material.

The *Instituto Nacional del Carbón (INCAR)* in Oviedo developed Ti-doped CFC. A mesophase pitch was mixed with TiC powder (130 nm average particle size) and applied for densification of the 2D fiber preform (which has a high porosity). After an oxidative stabilization, carbonization and graphitization at 2900 K the final material was obtained.

Both materials were received as small bars. After sawn in small plates of ≈12x15x1.5 mm^3, they were polished and ultrasonically cleaned in isopropanol.

4.2 Characterization techniques

4.2.1 X-ray diffraction (XRD)

The crystallographic phase and size of carbide crystallites formed in a-C:Me films were determined by X-ray diffraction (XRD). The diffractometer (Seifert XRD 3003 PTS) was operated with Cu K_α radiation (0.154 nm). The experimental setup was optimized to measure thin films. A parabolic multilayer mirror (W/Si) was used on the primary side to achieve a parallel beam and almost complete K_β suppression. On the secondary side, a parallel plate collimator – oriented perpendicular to the scattering plane – was installed to prevent detection of non-parallel beam intensity. Spectra were acquired in a θ-scan on a-C:Me films on Si substrate at an incident angle α of 1° between 2θ = 20-120°. Small samples (≈5x5 mm^2) were fixed on Si wafers to exclude contributions from the sample holder.

The Scherrer formula with a pre-factor of 1 was used to estimate the carbide crystallite size (section 2.1). Determination of the FWHM was done by fitting PearsonVII profiles to the diffraction peaks using the program fityk (version 0.7.6, [128]), including a fixed linear background which was adjusted by eye. This is shown exemplarily in Fig. 4.1. For quantification of the carbide grain size, the (111) peak was evaluated. All PearsonVII variables were free fit parameters, fityk provided standard deviations.

4.2.2 Raman spectroscopy

All Raman measurements were performed at Forschungszentrum Karlsruhe, IMF I. Spectra were measured between 900 and 1900 cm^{-1} with a Renishaw 1000 microscope using an argon laser at 514.5 nm. The software Wire (V. 1.3.18) was used to acquire the spectra applying continuous mode and 120 s detector time. The spot size was ≈1 μm^2 and the laser power was limited to 10 % giving ≈0.4 mW μm^{-2}, which induced no damage or structural changes in the films. This was checked visually and by applying a lower laser power which resulted in comparable spectra. For each sample 2 or 3 spectra were measured at different positions which were averaged to achieve better statistics. No significant differences of the individual spectra were observed at different positions of the same sample. Peak fitting was performed using the program fityk [128] as described in detail in section 2.2.3. It utilizes the Levenberg-Marquard

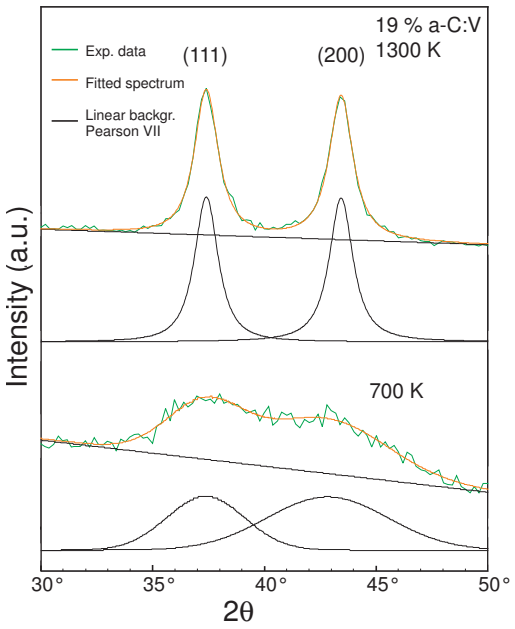

Figure 4.1: *Peak-fitted spectra of X-ray diffractograms from 19 % a-C:V samples, annealed to 700 and 1300 K. The fit included PearsonVII line shapes and a linear background.*

algorithm for non-linear least-square optimization, which provides standard deviations for the fitted parameters.

To check the influence of film reflectivity on Raman signal intensity, optical reflectometry measurements were performed at IPP with a Jobin Yvon PZ 2000 ellipsometer, choosing a wavelength of 515 nm, similar to the Raman laser wavelength.

4.2.3 Synchrotron-based techniques

4.2.3.1 XAFS

XAFS measurements at the *K* absorption edges of Ti, V, Zr and the W *L3*-edge were performed at HASYLAB (Hamburg) on beamlines A1, E4 and C.

XAFS spectra of a-C:Me films were acquired by recording the emitted fluorescence light (i.e., I) with a 7 channel Ge fluorescence detector perpendicular to the incident X-ray beam (fluorescence yield, FY). The angle between sample surface and beam was set to 45°. I_0 was measured by an ionization chamber (having a low partial pressure of N_2 or Ar) in front of the measurement chamber. During measurements the experimental chamber was pumped to ≈1 Pa.

Measurements of pure carbides (as powders, W_2C as sintered particle) were also performed at beamline C by measuring the emitted electrons (electron yield, EY) to avoid self-absorption effects which damps the EXAFS oscillations for bulk samples when using FY detection.

The measured energy range was about -200 eV to +800 eV in respect to the used absorption edge of the metal (Ti *K*: 4966 eV, V *K*: 5465 eV, Zr *K*: 17998 eV, W *L3*: 10207 eV). The pre-edge was scanned in 5 eV steps, the NEXAFS region with 0.2-0.5 eV step width, and the EXAFS region with 0.8 to 3.9 eV distance (equidistant steps in k space). The measuring time to record one spectrum was usually around 1 h, for samples with low metal concentration

several spectra were added to improve statistics. The spot size was ≈4 mm in width and ≈0.5 mm in height.

The software ATHENA [129] was used for normalization of the edge step to unity and removal of the background using the autobk algorithm. The FEFF code (version 8.2 [130]) was applied to calculate the theoretical scattering paths of carbides and TiO_2. The FEFF input files were created by ATOMS [131] with crystallographic data from the ICSD database [132].

In cooperation with Dr. M. Sikora, W *L1*-edge NEXAFS measurements were performed at beamline ID26 of the ESRF. A Si (660) crystal was applied to collect high resolution NEXAFS spectra at the maximum of the W Lβ_3 emission line (9819 eV), detected by an avalanche photodiode. Spectra were measured from 12080-12150 eV incident photon energy and normalized to the edge step at the highest energy.

Calculation of W *L1*-edge NEXAFS spectra of 3.5 Å clusters of W_2C, WC and WC_{1-x} were performed by Dr. M. Sikora using the code FDMNES [133]. The monoelectronic calculations are based on the Finite Difference Method (FDM) to solve the Schrödinger equation. In that way the shape of the potential is free and avoid the muffin-tin approximation, therefore FDM is more realistic for non-ionic solids [134].

4.2.3.2 Carbon NEXAFS and XPS

Carbon *K*-edge NEXAFS and X-ray photoemission (XPS) measurements were done at SRS Daresbury Laboratory (UK), beamline 1.1.

NEXAFS spectra were recorded under UHV conditions in total electron yield (TEY) mode by collecting the sample drain current, I. They were normalized by simultaneously recording the beam current using a gold-coated grid with 85 % transmission (I_0). Spectra were measured between 270 and 340 eV using 0.1 eV (280-340 eV) and 0.2 eV (270-280 eV) step width and an integration time of 1 s.

To exclude contributions from adsorbed hydrocarbons on Au grid and beamline optics, all spectra (I/I_0) were normalized by the obtained NEXAFS spectrum of a carbon-free silicon wafer, which was previously annealed to 1470 K for 30 minutes.

In-situ annealing of the samples was performed by conducting a current through the sample which therefore was resistively heated. The temperature was measured by a pyrometer. By manually varying current and voltage the temperature was controlled and held for 15 minutes at the desired value. The fine-grain graphite reference sample was annealed to 1300 K before measurement.

The sp^2 content of a-C was calculated by comparing the relative intensity of the π^* peak with a spectrum of fine-grain graphite (100 % sp^2) according to the following formula:

$$sp^2(\%) = \frac{A^{\pi*}_{a-C}}{A^{\pi*}_{graphite}} \frac{A_{graphite}(\Delta E)}{A_{a-C}(\Delta E)} * 100 \tag{4.1}$$

with $A^{\pi*}$ the π^* peak area between 283.0 and 286.0 and $A(\Delta E)$ a large fraction of the spectrum (290.6-305.0 eV), similar to [56,66]. A linear background was subtracted before integration.

XPS C 1s spectra were recorded at 400 eV photon energy using 0.05 eV step width, 20 eV pass energy and a dwell time of 0.4 s. To measure oxygen and metal spectra, 600 eV photons, a step width of 0.1 eV and a pass energy of 20 eV were used.

Due to energy shifts during the measurements, all C 1s spectra were shifted to 284.2 eV for the maximum peak intensity and normalized to unity. For quantification of the surface composition sensitivity factors of a conventional XPS system were used, since they were not

provided for the used setup: 0.314 (C 1s), 0.711 (O 1s) and 1.798 (Ti 2p). Therefore, the atomic concentrations should be only regarded as rough estimate.

4.2.3.3 X-ray emission spectroscopy (XES)

Measurements of X-ray emission spectra were performed in the frame of a cooperation with Dr. M. Sikora at the undulator beamline ID26 (High Brilliance XAFS-XES beamline) at ESRF, Grenoble.

For measurements on a-C:V and VC samples, the incident photon energy was 5500 eV, which is above the V K-edge (5465 eV), provided by means of a pair of Si (111) single crystals. Higher harmonics were suppressed by two Si mirrors at 3.0 mrad. The beam on the sample was ≈0.25 mm horizontal and 1 mm vertical with a total flux in the order of $2.5{\cdot}10^{13}$ photons s^{-1}. The radiation induced heating of the sample should have not increased the temperature above 370 K.

The emitted fluorescence light was analyzed by means of a spherically bent (R = 1000 mm) Ge wafer (85 mm diameter) that employs the (422) Bragg plane. To reduce absorption and scattering of the fluorescence light by air, a He filled balloon was placed inside the spectrometer along the optical path between sample, analyzer and detector. The energy bandwidth in the X-ray emission detection was 0.7 eV. An avalanche photodiode of 100 µm thickness was used as detector. The fluorescence energy region including the Kβ main and Kβ satellite lines was measured from 5400 to 5475 eV. Spectra were normalized by the integral spectral intensity.

4.2.4 Rutherford backscattering spectroscopy (RBS)

Rutherford backscattering spectroscopy (RBS) was applied for film analysis and for quantification of the total erosion yield after deuterium erosion (see chapter 4.3.1). The IPP tandem accelerator provided high energetic ion beams, the measurements were performed in the RKS endstation.

4.2.4.1 Film composition

A beam of 4 MeV $^4He^+$ was used to determine the elemental composition of the carbon films depth-resolved. The spot size was about 1x1 mm^2 and a charge of 20-30 µC was accumulated for a spectrum. The scattering angle was 165°. Measurements on different positions of the same sample revealed good lateral homogeneity. The oxygen content was determined using films deposited on graphite substrates. An energy of 500 keV was used to increase the depth resolution at the surface. The spectra were simulated using the program SIMNRA 6.02 [79]. Hence, the film composition could be determined in at%. For convenience, the following notation is used throughout the text to describe a carbon film containing x at% metal: x % a-C:Me.

4.2.4.2 Quantification of absolute erosion yield

The amount of eroded carbon (and metal) atoms was estimated by analyzing eroded samples on Si wafers with 1.5 MeV H^+ at normal incidence. At this energy, the cross-section for carbon is large, leading to a carbon peak on a broad silicon signal and a separate metal peak, as shown in Fig. 4.2. Integration of the peaks (using the program SpecInteg [135]) gives an absolute measure of the amount of carbon and metal (in at cm^{-2}) in the analyzing spot.

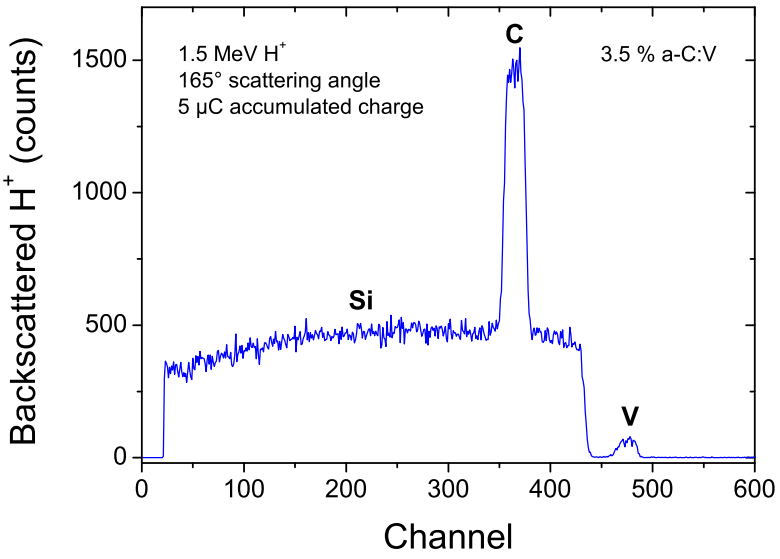

Figure 4.2: *1.5 MeV H^+ RBS spectrum of an 3.5 % a-C:V film on silicon wafer. Quantification of C and V amounts were performed by integration of both peaks.*

The following formula was applied for calculating the area density N (at cm^{-2}) [77]:

$$N = \frac{A \cos\Theta\, e}{Q\,\Omega\,\sigma} \tag{4.2}$$

with A as the integrated intensity, Θ the incidence angle, e the elementary charge ($1.602 \cdot 10^{-19}$ C), Q the accumulated charge (C), Ω the detector solid angle ($1.19 \cdot 10^{-3}$ sr), and σ the scattering cross-section (C: $1.688 \cdot 10^{-25}$, Ti: $2.88 \cdot 10^{-25}$, V: $3.14 \cdot 10^{-25}$, W: $3.23 \cdot 10^{-24}$, Zr: $9.49 \cdot 10^{-25}$ m^2 sr^{-1}).

The dimension of the erosion crater, created during D_3^+ bombardment (see section 4.3.1) was estimated by performing two perpendicular scans (0.5x1 mm^2, step width 0.5 mm, accumulation of 5 µC) over the sample including also un-eroded area at the sample edges. Typical erosion spots are shown in Fig. 4.5. The area of the erosion spot and its depth was determined by extrapolating a rectangular spot profile for both scan directions. This is shown exemplarily for a line scan in Fig. 4.3.

This virtual rectangular spot profile was then used to calculate the absolute erosion yield (Y_{IBA}) according to the following formula:

$$Y_{IBA} = \frac{\text{eroded carbon thickness (at cm}^{-2}) \cdot \text{erosion spot area (cm}^2)}{\text{impacting D (at)}}.$$

Since the number of impacting D is well quantified by charge measurement, the accuracy of Y_{IBA} is determined by the error introduced by estimating the rectangular beam profile, as described above. For most films the error should be smaller than ±30 %, but for films with low erosion it could exceed ± 50%. The uncertainty of the metal yield is even larger than 50 % because of the small amount of eroded metal.

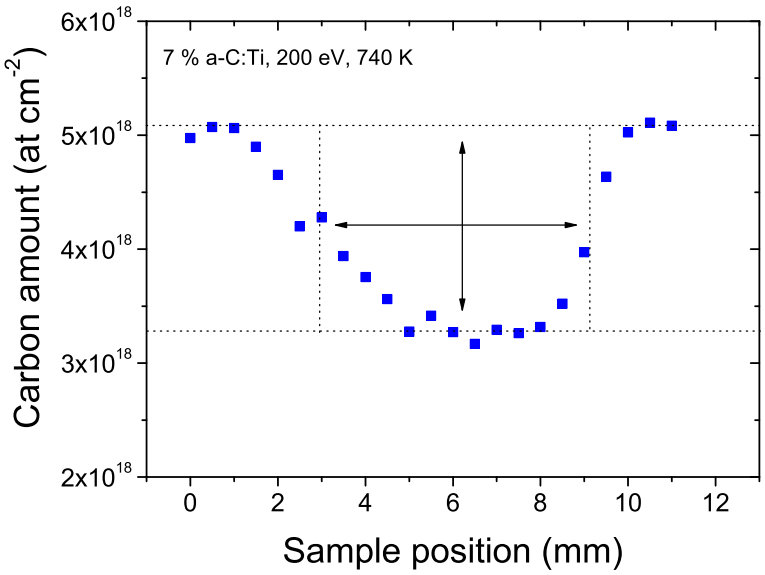

Figure 4.3: *Cross-section of the erosion crater on a 7 at% a-C:Ti film created by 200 eV D impact at 740 K. The data points represent the carbon area density measured by 1.5 MeV H^+ across one direction of the erosion spot.*

4.2.5 Microscopy (SEM, TEM, AFM)

Scanning electron microscopy (SEM) was performed to study the surface morphology (Philips XL 30 ESEM, usually operated at 20 kV).

Preparation of cross-sections of annealed a-C:Me films on silicon wafers and subsequent TEM analysis was done by M. Rasinski at IPP. The TEM (Philips EM 430) was operated at 300 kV. For TEM studies of Dr. H. Leiste (Forschungszentrum Karlsruhe, IMF I), films were deposited on polished hard metal stripes (Co-WC). Thin cross-sections were prepared and subjected to TEM analysis (Philips CM30, 300 kV).

Surface morphology of pristine and eroded a-C and a-C:Me films on Si wafers was studied by atomic force microscopy (AFM) in contact mode (Rasterscope 4000, AFM 2194, DME). DC cantilevers (DME DC Probe 2622) with pyramidal Si tips (NanoWorld Pointprobe CONTR) with tip radius of curvature <10 nm were used. The maximum resolution of 512x512 points and a constant force of 1 nN was chosen. The open-source software Gwyddion [136] was applied for raw data processing. Roughness was quantified using the the root mean square definition (RMS)

$$R_q = \sqrt{\frac{1}{n}\sum_{i=1}^{n} y_i^2}$$

with the RMS mean line such that the sum of the square of the deviations of the profile height from it is equal zero [137]. The program determines R_q for the whole scan area by averaging the values determined for each scanned line. The used pixel size can influence the calculated

R_q for a surface with low roughness. Therefore, comparison of R_q is only possible for the same experimental settings (scan area, pixel number).

4.3 Ion beam and plasma erosion experiments

4.3.1 High current ion source

The IPP high current ion source [37] was used to study the erosion behavior under D ion bombardment. It provided mono-energetic (90 eV, 600 eV, 3000 eV) D_3^+ ion beams which results in 30, 200 or 1000 eV per impacting D, assuming equal energy distribution on each D after reaching the surface and splitting of the D_3^+ molecule[1]. The deuterium flux was in the order of 10^{19} D m^{-2} s^{-1}.

The setup of the high current ion source is shown in Fig. 4.4. A high current injector of the Oak Ridge type is used as ion source. D_2 is ionized by electrons emitted from a cathode, and the ions are extracted and accelerated by a high voltage (3000 V + x V, with x V as the desired D_3^+ energy (p≈5·10^{-3} Pa). After focused by a grid system the ion beam passes a differential pumping stage. The magnetic analyzer (p≈3·10^{-3} Pa) is adjusted to deflect only species with m/z of 6 (i.e. D_3^+) into the target chamber, where a base pressure of 1·10^{-5} Pa (1·10^{-4} Pa during operation) is achieved by a cooling trap with liquid nitrogen. The cooling trap is normally applied in measurements with operating mass spectrometer. The sample holder is set to a bias voltage of +3000 V which decelerates the D_3^+ ions to the desired energy of 90, 600, or 3000 eV.

Heating of the samples (size usually 12x15 mm^2) is performed by means of electron bombardment from a grounded tungsten filament, located behind the sample utilizing the 3 keV. The current is remote controlled by a computer. The sample temperature is monitored by an infrared pyrometer (TMSR 95/105, Dr. Georg Maurer GmbH) outside the target chamber. It is calibrated against a filament pyrometer (Mikro Pyrometer 3725, Pyro-Werk GmbH) during pre-annealing of each sample at 1100 K for 15 minutes before the erosion experiment. During calibration, the emissivity of the sample is determined by adjusting the temperature measured by the infrared pyrometer to the value obtained by the filament pyrometer.

The current introduced by the ion beam is measured by an electronic charge integrator. A Faraday cup around the target accounts for secondary electrons, produced by the ion impact.

The D fluence was calculated according to the following formula

$$F = \frac{3 \cdot Q}{e \cdot A} \tag{4.3}$$

with F the deuterium fluence (D m^{-2}), Q the accumulated charge (C), e the elementary charge (1.602·10^{-19} C), A the spot size (m^2), as determined by ion beam analysis described in 4.2.4. The factor of 3 accounts for the D_3^+ molecule.

An integrated balance (Mettler ME21) allows in-situ measurement of the sample weight-loss with an accuracy of ±1 µg.

The gas phase was analyzed by a quadrupole mass spectrometer, QMS (QMG 422, Pfeiffer Vacuum), separated by an aperture. It is oriented line-of-sight in 45° to the sample surface, but due to the long distance (25 cm) the QMS signal is dominated by the gas atmosphere.

[1] Nevertheless, recent experimental results and theoretical calculations show slightly different erosion yields per D depending on the impacting species (D^+, D_2^+, D_3^+) for energies <60 eV/D [138].

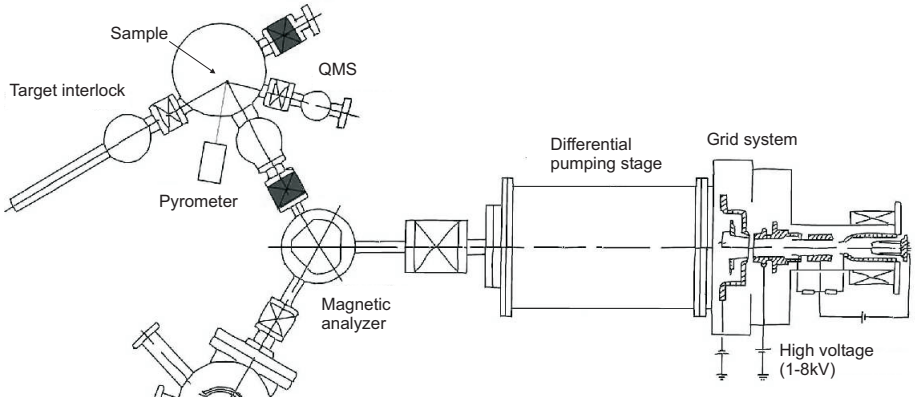

Figure 4.4: *Setup of the IPP high current source used for D ion beam erosion experiments. The second chamber attached to the ion source was not in use during experiments.*

Therefore, the measured species have undergone several wall collisions. By a surrounding liquid nitrogen cooling trap in the QMS chamber a pressure of $\approx 2 \cdot 10^{-5}$ Pa was achieved.

4.3.1.1 Experiments at fixed ion energy and temperature

To determine the total carbon erosion yield for specific conditions (ion energy, temperature) with sufficient accuracy, fluences $>10^{23}$ D m^{-2} were accumulated on a-C and a-C:Me samples with Si substrate and doped CFC and graphite samples (12x15 mm^2). Prior the erosion experiments all specimens were annealed to ≈1100 K for 15 minutes. This lead to desorption of adsorbates and in the case of a-C:Me films to the formation of carbide crystallites of several nm size (see section 5.2.1).

The **total erosion yield** ($Y_{WL/IBA}$) was determined from the accumulated ion fluence (a-C:Me films: $4\text{-}9 \cdot 10^{23}$ D m^{-2}, bombardment usually one night; doped graphites and CFC: $10^{24}\text{-}10^{25}$ D m^{-2}) onto the specimen and the total amount of eroded carbon. These amounts were measured by in-situ weight-loss (WL) and/or by ion beam analysis (IBA). The weight-loss of a-C:Me was typically only a few µg, therefore the uncertainty could exceed ±50 %. Also the composition of the eroded material can not be resolved from the weight-loss. Determination of the erosion crater by means of IBA as described in section 4.2.4 gives a more accurate measure of the total eroded carbon amount. For doped graphite and CFC samples, the total erosion yield was determined by in-situ weight-loss as a function of D fluence. For that, the erosion of a sample was performed over several days and nights, measuring the mass-loss twice a day.

Fig. 4.5 shows two typical erosion spots, produced on a-C:Me films after deuterium ion beam erosion. On the left sample an additional spot (appearing blue on the picture) is visible on the lower side. This is a result of undesired irradiation with high energetic species which were neutralized after passing the magnetic analyzer. Therefore, they were not decelerated and hit the sample with the full extraction energy. An accurate determination of their contribution was performed by Balden and Roth [117] who reported about a fraction of 3 % neutrals in a 180 eV D_3^+ beam. This contribution is not further taken into account in analysis and discussion.

The **methane production yield** (Y_{CD_4}) was obtained from the QMS signal of m/z 20 (CD_4), measured in steps of 6 seconds. The cooling trap in the target chamber increased the sensitivity for CD_4 by adsorption of (deuterated) water. On the other hand, no information

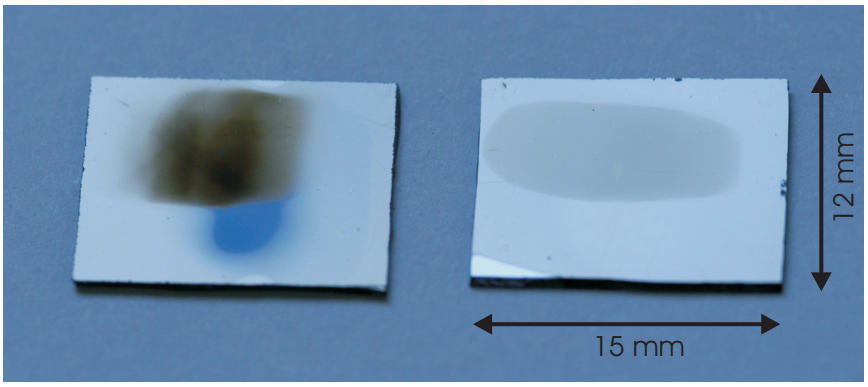

Figure 4.5: *Erosion spots on a-C:Me films after deuterium ion beam bombardment. Left sample: 30 eV D irradiated 2 % a-C:Zr sample with $4.6{\cdot}10^{23}$ D m^{-2} at 300 K. The small dark blue shadow on the bottom side is a result of the small fraction of neutrals. Right sample: 200 eV D irradiated 3.5 % a-C:Ti specimen with $9.0{\cdot}10^{23}$ D m^{-2} at 740 K.*

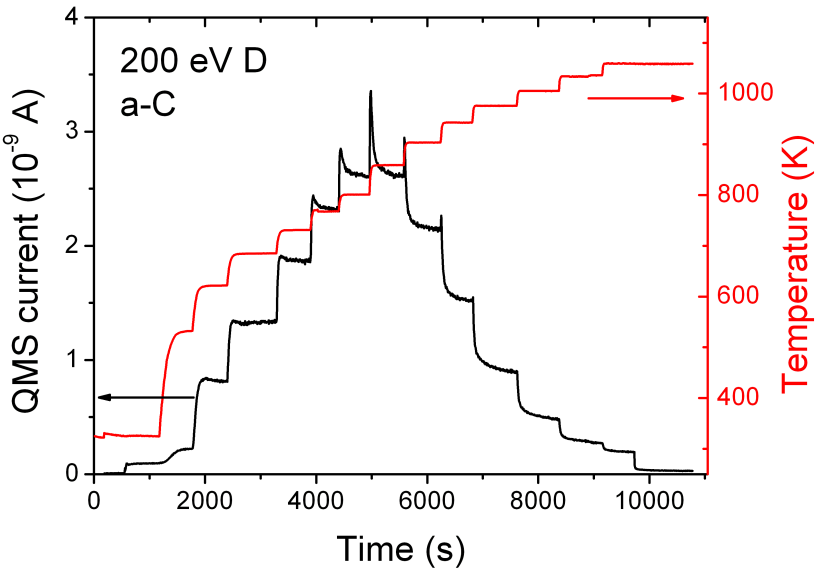

Figure 4.6: *m/z 20 measured by QMS during a temperature dependent measurement to determine the methane production yield (Y_{CD_4}) at 200 eV D impact.*

about higher hydrocarbon species can be gained, because they are also adsorbed at the cooling trap. Several m/z signals were recorded during each erosion experiment but only m/z 18 and 20 will be discussed in this work. Contributions from the background gas were corrected linearly by measuring the signals before and after the experiment with deflected ion beam. Other possible hydrocarbon sources (e.g. desorption of species from the chamber walls) were neglected and due to the cooling trap also (deuterated) water species should not contribute to m/z 18 and 20. The background-corrected signals were normalized to the ion flux and to the signal from pyrolytic graphite bombarded with 1 keV D at T_{max} (≈800 K), as described in detail in [117]. At these conditions the chemical sputtering yield of graphite was determined to be 0.1 [118,119], and under the assumption that the only species released is CD_4, the chemical sputtering yield equals Y_{CD_4}. This normalization has to be taken with care, because CD_4 is in fact the main, but not the only emitted species, especially at D energies < 100 eV where C_2 and C_3 species also have significant contributions [113,116,117].

4.3.1.2 Temperature dependent measurements

The **methane production yield** (Y_{CD_4}) was also measured for a-C and a-C:Me as a function of temperature between 300 and 1100 K. Before the experiment, the samples were annealed to ≈1100 K for 15 minutes to exclude structural changes during the measurement due the temperature ramp. The background correction and data normalization was performed in the same way as described above. Each temperature step was normally held for about 6-10 minutes to reach a steady-state in the release of hydrocarbons, i.e. a constant m/z 20 (CD_4) QMS signal, which is reached at fluences of $<10^{22}\,D\,m^{-2}$ [29,139]. The fluence for a temperature step was typically $4\text{-}7{\cdot}10^{21}\,D\,m^{-2}$, which is also low enough to minimize effects of dopant enrichment (carbide grains) due to preferential sputtering of carbon.

In Fig. 4.6 the evolution of m/z 20 with increasing temperature is shown for 200 eV D bombardment of an a-C film. The calculation of Y_{CD_4} for each temperature was done by taking the average of the last 11 data points of each temperature step.

4.3.2 Low temperature plasma facility

Deuterium plasma exposure experiments were performed in cooperation with the University of Augsburg by Dr. P. Starke at the chair for Experimental Plasma Physics. Fig. 4.7 shows schematically the setup of the planar inductively coupled RF low pressure plasma experiment used for erosion studies of carbon films [140,141].

The plasma consists of 10 % deuterium in He at a pressure of 20 Pa and is sustained by an external RF generator. By addition of He the electron density and temperature is increased and likewise the dissociation of molecular to atomic deuterium. a-C and a-C:Me films on Si substrates (30x30 mm^2) were placed on the substrate holder in the center of the cylindrical discharge and by applying a bias voltage (-20 V) the ion energy was adjusted to 30 eV, taking into account the plasma potential. The sample holder was actively water-cooled which gave a sample temperature of about 300 K. The atomic deuterium flux on the sample was measured by optical emission spectroscopy (OES) in line-of-sight (LOS) configuration and was estimated to $1.0{\cdot}10^{23} m^{-2}s^{-1}$.

The total ion flux Γ_{Ion} was about $7\cdot10^{20}$ $m^{-2}s^{-1}$ obtained by an energy mass analyzer (EMA) in combination with a Langmuir probe. It is about ten times higher than achieved in the high current ion source for energetic D. An ion fluence of $1{\cdot}10^{24}\,m^{-2}$ can therefore

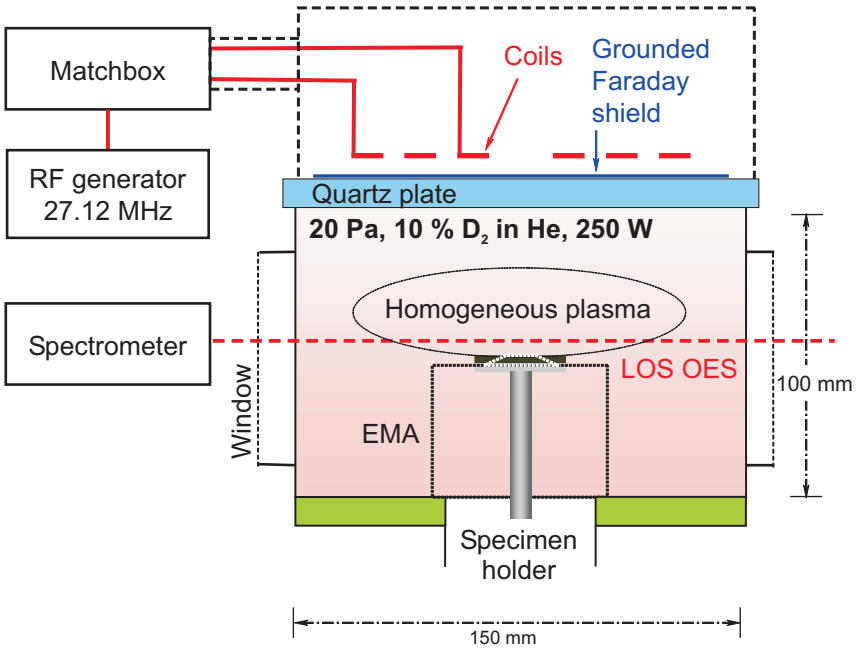

Figure 4.7: *Schematic of the planar inductively coupled RF low pressure plasma experiment used for erosion experiments. Courtesy of Dr. P. Starke, University of Augsburg.*

achieved after about 25 minutes of plasma operation. The main species is D^+, but also other species contribute to the ion flux on the surface: 60 % D^+, 10 % (D_2^+/He^{2+}) and 30 % D_3^+. By time-resolved OES analysis of the CD (431 nm) and C_2 (516 nm) band emission, the carbon flux due to erosion of the specimen could be measured in-situ during the experiment. Quantification of the total eroded carbon amount by RBS after the experiment (section 4.2.4) allows to calibrate the carbon flux data using the following formula [142]:

$$\Gamma_C(t) = A \cdot \varepsilon_{CD}(t) \cdot \left(1 + 2 \cdot B \cdot \frac{\varepsilon_{C_2}(t)}{\varepsilon_{CD}(t)}\right) \tag{4.4}$$

with $\Gamma_C(t)$ the absolute carbon flux from the sample (at $m^{-2}s^{-1}$), A the total amount of eroded carbon measured by RBS (at m^{-2}), ε the intensity of CD or C_2 emission bands measured by OES (s^{-1}) and $B = 3.29$, a factor which contains the excitation mechanisms for the relevant excited states of the CD and C_2 molecules. It was thoroughly determined in [140].

The carbon erosion yield at a given fluence (i.e. time) is estimated by calculation of Γ_C/Γ_{Ion}. Each experiment was stopped when the spectroscopic signal reached the range of the detection limit.

Chapter 5

Characterization

In this chapter, results from various investigations are presented in order to resolve the a-C:Me film structure in detail. The influence of three parameters was tested: metal type (Ti, V, Zr, W), metal concentration (0-19 %) and post-annealing temperature (700, 900, 1100, 1300 K), as shown schematically in Fig. 5.1. The metal distribution can influence the obtained erosion yield, as shown in section 6.2 for a set of experiments.

It was decided to apply a larger number of different experimental techniques, at expense of going into the very detail in the respective analysis. For investigation of structural changes on the nanometer scale in a heterogeneous material as a-C:Me, this approach gives a better global view of the structural situation. For example, fitting of C 1s XPS spectra was kept on a relatively simple level compared to approaches demonstrated in recent publications [143]. Also, EXAFS data can be fitted to a model to derive structural parameters as described in section 2.3.1. Nevertheless, a problem of such procedures is that usually a defined crystalline structure is used as model, which is challenging when applied to amorphous matter (even if a fit is possible and produces *values*). Due to the high effort needed for performing reasonable fits, only a qualitative comparison is presented.

First, a short description of the film composition and morphology is presented. The two main sections are dealing with investigations of the *metal distribution and phase* and the

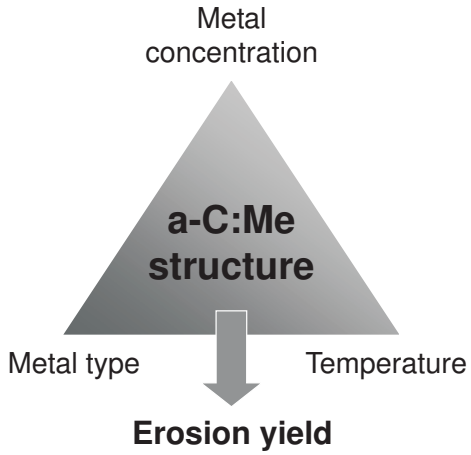

Figure 5.1: *Metal type, concentration and annealing temperature are the investigated factors which have impact on the a-C:Me film structure.*

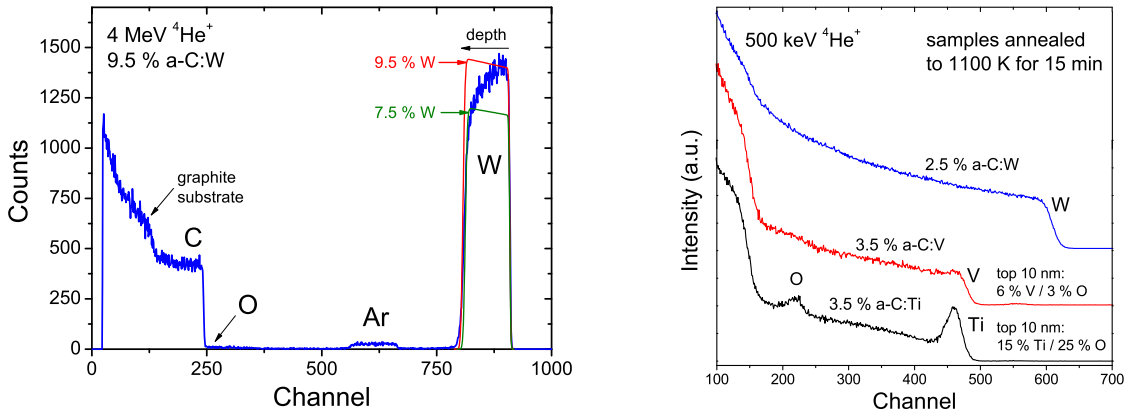

a) b)

Figure 5.2: *a) 4 MeV $^4He^+$ RBS spectrum of 9.5 % a-C:W film on graphite substrate. The calculated signal for 9.5 % (red) and 7.5 % (green) W are also shown. b) RBS spectra of 1100 K annealed a-C:Me films using 500 keV $^4He^+$ to increase the resolution of the surface-near region.*

carbon matrix (see also Fig. 1.2). Results of carbide grain size determination (XRD, TEM), the local atomic environment around the metal (XAFS, XES) and the tungsten carbide phase (XRD, NEXAFS) are presented in the first part. Crystallinity (XRD), aromatic clustering (Raman) and carbon bonding state (XPS) are the main points in the analysis of the carbon matrix.

5.1 Composition and surface morphology

5.1.1 Film composition and homogeneity

RBS analysis with 4 MeV $^4He^+$ confirmed very good homogeneity of the deposited a-C:Me films regarding composition in lateral space and also for different specimens of the same deposition run. Usually 1-2 % Ar and O are present in as-deposited samples. Traces of metallic impurities (e.g. Cu, Fe, Mo) could be detected in some samples but their concentration is usually well below ≈0.2 %. The in-depth dopant concentration decreases to the substrate side, as shown for a 9.5 % a-C:W[1] film in Fig. 5.2a. A continuously decreasing W concentration with depth can be observed. The concentration gradient is lower for the surface-near region. For a film thickness of 835 nm, the W concentration in the upper ≈350 nm is about the given 9.5 %. For the ≈200 nm directly above the substrate a metal concentration of 7.5 % is observed. This is indicated in Fig. 5.2a by the calculated W signal for both concentrations. Similar concentration gradients are observed for all deposited a-C:Me films. It is due to the incapacity of the sputter device to regulate low cathode powers properly. Generally, the given concentration values represent the topmost 30-40 % of the layer. The metal concentration in the lower 50 % of the sample can be up to 20-40 % lower. Tab. 5.1 summarizes thickness and concentration data of all films used in this work. All values given in this work are at% and rounded to 0.5 %.

[1] In this work, the notation x % a-C:Me is used to describe a metal-doped carbon film with concentration x of dopant metal Me. All given concentrations are at%.

After annealing to 900 K the Ar content is reduced, after 1100 K it is completely vanished. No increased oxygen concentration in the bulk was observed after annealing. RBS measurements with 500 keV $^4He^+$ show, that annealing to 1100 and 1300 K leads to surface enrichment of the metal (and oxygen) in about the topmost 10 nm for Ti, V and Zr-doped samples. This is shown in Fig. 5.2b for three 1100 K annealed films with similar concentrations. For 3.5 % a-C:Ti the observed surface enrichment peak is related to 15 % Ti in a ≈10 nm thin layer. The increased oxygen content leads to the assumption, that Ti is mainly present as TiO_2. For a-C:Zr a similar behavior is observed. As obvious from the the 3.5 % a-C:V spectrum, enrichment is less pronounced with only about 6 % V. For 2.5 % a-C:W no surface segregation is observed. The different behavior depending on the dopant metal is reasonable, since the surface segregation is expected to be driven mainly by oxide formation (oxygen partial pressure in high vacuum oven), and the ability of the metal to diffuse in the material. Oxide formation is more favored for Ti compared to V ($\Delta G_{f,TiO_2}$= 745 kJ mol^{-1}, $\Delta G_{f,\frac{1}{2}V_2O_5}$ = 547 kJ mol at 1100 K). Diffusion of W in a-C should be much lower due to the lower atomic mobility, indicated by the less pronounced temperature-induced carbide crystallite growth (section 5.2.2).

The metal surface enrichment does not strongly alter the metal concentration in deeper regions, but directly below the enrichment zone. Here, for several ten nm, a small depletion of metal is observed.

For most of the applied (bulk sensitive) experiments, the described metal surface enrichment should not influence the interpretation. For surface sensitive XPS and NEXAFS measurements, annealing was performed in-situ in UHV, which should significantly reduce this effect. For erosion experiments with a 30 eV D ion beam (where annealing to 1100 K was always performed before measurement) a higher local metal concentration at the beginning has to be considered if annealing is performed without cooling trap. For bulk sensitive techniques the concentration values given in this work always represent a concentration range.

5.1.2 Surface morphology

The surface morphology of the sputter-deposited films depends strongly on the substrate material. This is demonstrated in Fig. 5.3 for an a-C:Zr film deposited on graphite and on Si wafer. The much rougher surface of the polished graphite – with characteristic cauliflower structure – is reflected in the surface morphology of the deposited layer. For a scan area of 4x4 µm the calculated surface roughness (R_q) of this film is 43 nm for graphite and 1.9 nm for Si substrate. This observation is in line with the appearance of cross-sections in SEM analysis. For graphite substrate, a columnar structure is often observed, but on Si substrate the cross-sections appear more dense and featureless without indication of columnar growth.

To investigate the influence of doping on the surface morphology and roughness, films deposited on Si wafer were analyzed by AFM, applying a scan area of 1x1 µm. The surface roughness R_q is between 2.5 and 4 nm for all investigated films. As obvious from Fig. 5.4a, no relation on metal type or concentration could be observed. Fig. 5.4b shows exemplarily an AFM picture of a 3.5 % a-C:V film with 1x1 µm scan area.

As a result of AFM/SEM investigation almost all experiments were performed on films deposited on Si wafer to exclude any influence of the surface roughness, especially for RBS analysis. Also possible effects on temperature-induced diffusion processes by a less dense, more columnar film structure are therefore minimized.

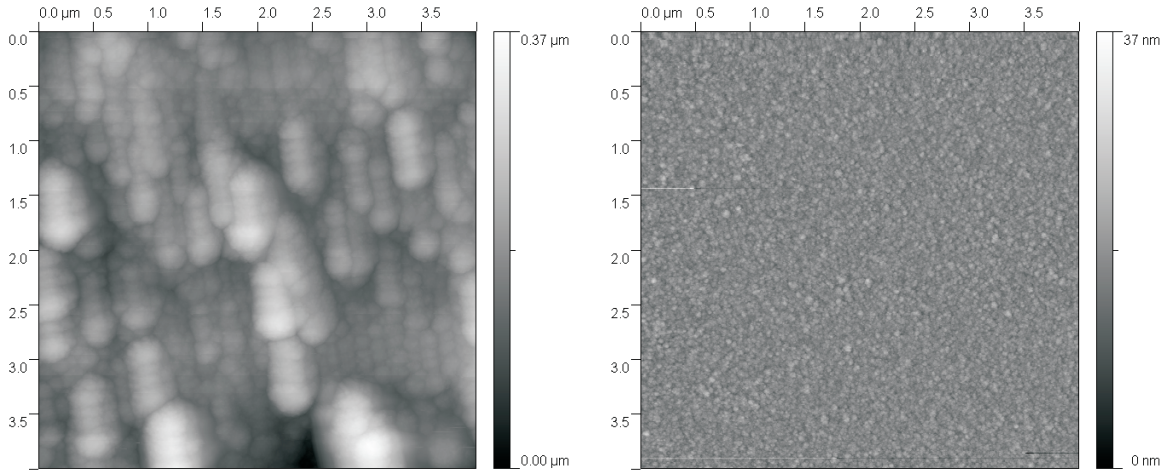

Figure 5.3: *Surface morphology of an 11 % a-C:Zr film deposited on graphite (left) and silicon substrate (right) measured by AFM with the same experimental conditions 4.2.5. Note the 10 times higher z-scale in the case of graphite as substrate.*

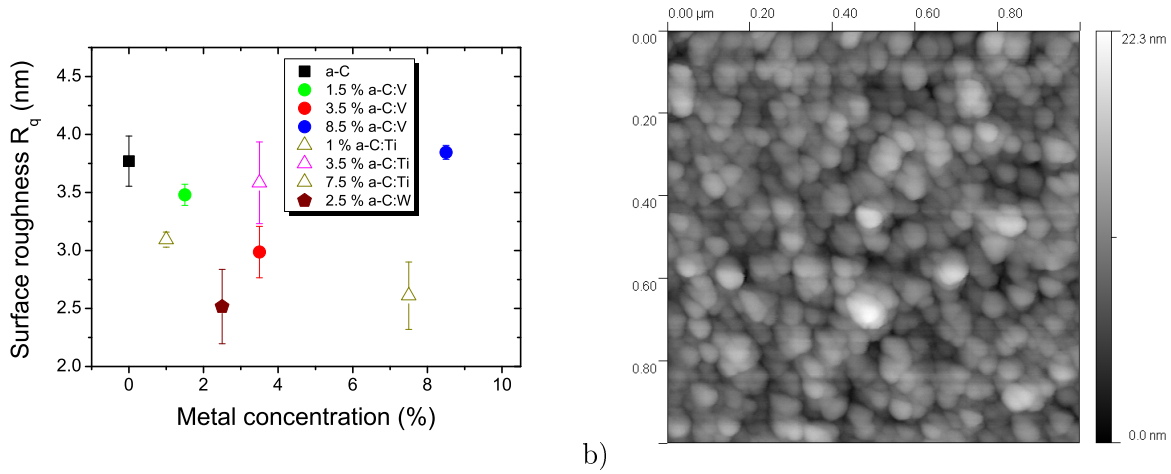

a) b)

Figure 5.4: *a) Summary of surface roughness parameters (R_q) of different a-C:Me films, determined by AFM (1x1 µm scan area). The values are an average of R_q values for three AFM scans on different sample positions. b) 1x1 µm AFM image of 3.5 % a-C:V film.*

Table 5.1: *Summary of a-C:Me films used in this work. Concentrations were rounded to full 0.5 %, thickness values (determined by profilometry) to full 5 nm. * Values for multilayer specimen are only for the doped layer, thickness is in 10^{14} at cm^2. Layers labeled with ** have been produced in the course of a former diploma thesis [144]. For them only the metal concentration is given.*

Dopant	Atomic concentration (Me / O / Ar)	Thickness (nm)	Internal label
-	- / 2 / 1.5	1650	CS24
Ti	1 / 2 / 1	900	TiS35
	3.5 / 2 / 1.5	945	TiS34
	6 / 1.5 / 1	635	TiS11
	7 / 1.5 / 1	650	TiS12
	7.5 / 2 / 1.5	880	TiS36
	10 / 2 / 2	≈1000	TiS48
	13	440	16A**
V	1.5 / 1.5 / 1	1015	VS32
	3.5 / 2 / 1	1045	VS31
	8.5 / 2 / 1	990	VS33
	19 / 1 / 1	1460	VS25
Zr	2 / 2 / 1	605	ZrS19
	7 / 2 / 1	640	ZrS20
	7.5	775	J**
	11 / 2 / 1	755	ZrS18
	14 / 1.5 / 1	265	ZrM05*
	14.5	1100	L**
W	2.5 / 3 / 2	800	WS39
	3	1560	B**
	4	1100	E**
	6.5 / 3.5 / 3	1065	WS47
	9.5 / 3 / 3	835	WS41
	12.5 / 3 / 3	320	WM25*
	14.5	540	D**

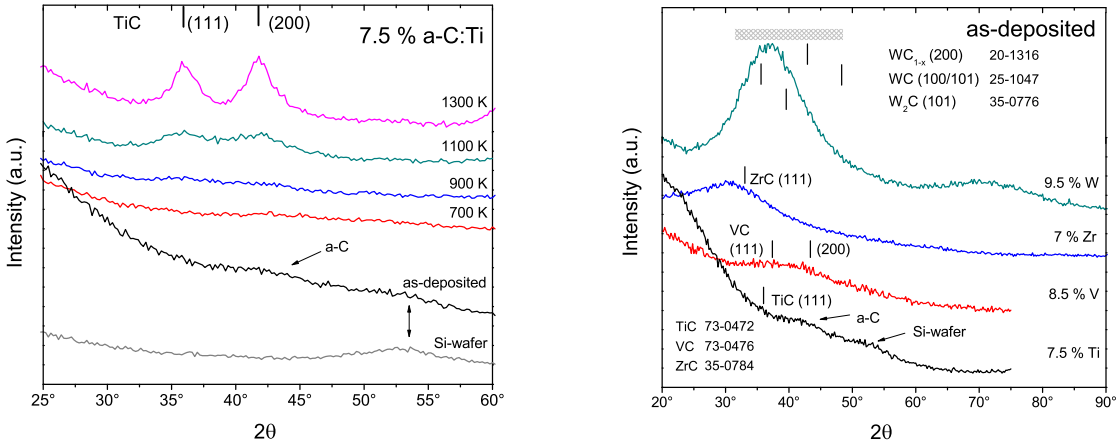

a) b)

Figure 5.5: *a) X-ray diffractograms of an annealing series of 7.5 % a-C:Ti. Contributions of a-C and the silicon substrate are visible for the as-deposited sample. The peak positions of TiC (111) and (200) reflexes in the shown angle range are indicated. b) Diffractograms for as-deposited samples of different a-C:Me films with 7-9.5 % metal concentration. The positions of the most intense carbide peaks are indicated, the PDF card number (JCPDS database [145]) of the carbides are given. For a-C:W, the observed maximum does not correspond to the maximum peak positions of the three indicated carbide phases. The bar indicates that also other carbide peaks occur in that region with lower intensity.*

5.2 Investigation of metal distribution and phase

In this chapter XRD, TEM[2], XAFS and XES results are presented, exploring the question how the metal is distributed in the carbon matrix: finely dispersed in amorphous environment without long-range order or in the form of small carbide crystallites. An important aspect is, how carbide formation is affected by annealing. XRD and TEM are only sensitive if crystallinity is present. XAFS and XES can be applied also for amorphous metal environment.

5.2.1 Determination of carbide crystallite size by XRD and TEM

5.2.1.1 Qualitative comparison

X-ray diffraction was used to investigate the formation of a crystalline phase in a-C:Me films. The setup was optimized for thin film analysis as described in 4.2.1 applying a parallel beam geometry and 1° gracing incidence[3]. The optimization of signal intensity results in a large experimental line width of about 0.3°, determined for the Si (111) peak at 28.4°. Nevertheless, since the observed peaks are generally about 10 times broader, the influence on the peak width for the crystallite size determination can be neglected.

Fig. 5.5a shows diffractograms between 25° and 60° of a 7.5 % a-C:Ti film annealed up to 1300 K. The increase in intensity towards lower 2θ is observed in different extent for all

[2] TEM measurements were performed by M. Rasinski (IPP) and Dr. H. Leiste (FZK).

[3] For this measurement setup the term GIXRD is often applied. Nevertheless, throughout the text the more general term XRD is used for convenience.

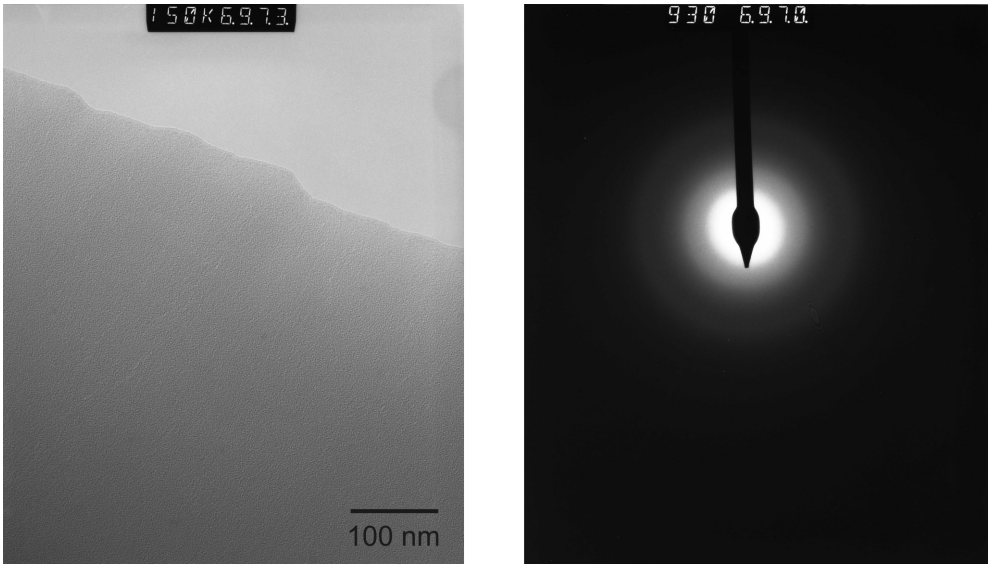

Figure 5.6: *a) TEM micrograph of an as-deposited 10 % a-C:Ti film. b) The electron diffraction pattern taken from the same image area indicates amorphous Ti environment and no carbide crystallites.*

diffractograms and is due to the used measurement geometry [51]. For pure a-C a much stronger increase is observed, which is probably due to the small amount of graphene-like crystallites (see section 5.3.1). They also lead to the small signal around 43°. Interestingly, intensity at small 2θ is much lower in the case of doping. The origin could be a different carbon nanostructure, but also the influence of doping on absorption and reflection of X-rays, or the layer thickness (about 50 % larger for a-C) could be the reason.

The as-deposited a-C:Ti sample shows only two weak and broad features, which can be attributed to contributions of the silicon wafer (probably the SiO_2 layer on top) and the carbon matrix. This indicates an amorphous Ti environment without formation of carbide crystallites. Annealing to 900 K reveals two very weak humps, which develop with further annealing as the (111) and (200) peaks of $B1$ phase of TiC.

The amorphous Ti environment in the as-deposited sample is supported by TEM, where no crystallinity could be detected in a 10 % a-C:Ti sample. Fig. 5.6 shows the TEM bright field and electron diffraction pattern.

In contrast to 7.5 % a-C:Ti, doping of a-C with similar concentrations of V, Zr and W leads to visible features in the diffraction patterns of the as-deposited samples as shown in Fig. 5.5b. For V and Zr-doping, broad peaks indicate a low amount of crystallinity in VC and ZrC phases. The maxima are shifted from the indicated positions of the pure carbides. This is probably due to disorder, and in the case of VC overlapping of both carbide signals (and the carbon signal) might be responsible. Since both VC and ZrC signals are broad and weak, it can be assumed that only a small fraction of the metal is situated in very small (and probably distorted) carbide crystallites. Nevertheless, many factors [51] have impact on the observed intensity, which preclude its quantitative analysis. Generally, scattering intensity increases with the atomic number.

For both films, annealing leads to the development of more intense and narrow peaks, which can be assigned as the $B1$ phases of VC and ZrC. Also other carbide peaks at higher

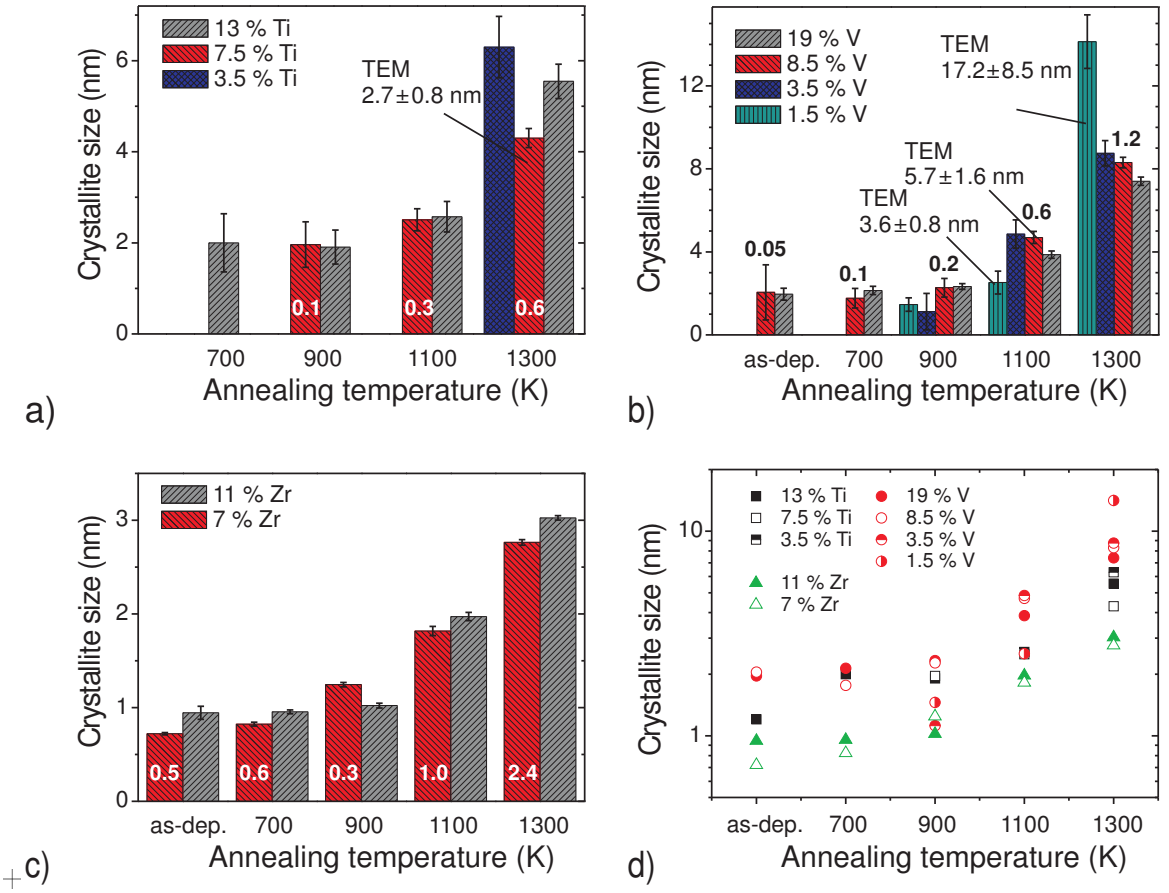

Figure 5.7: *a-c) Carbide crystallite sizes, determined from the fitted (111) peak of X-ray diffraction patterns. The error bars represents the uncertainty by determining the FWHM in the peak fitting procedure. The intensity ratio of the fitted peak and background is given for samples with about 8 % metal content. For some samples the average size was also determined by TEM. d) The XRD data from a-c) summarized in one plot with logarithmic scale.*

2θ angles develop analogous to a-C:Ti. Generally, the observed increasing peak intensity and decreasing peak width with annealing temperature indicates carbide formation and crystallite growth. Samples with lower concentrations (V: 3.5 %, 1.5 %; Zr: 2 %) appear completely X-ray amorphous after deposition.

For W-doping the situation is different. A very broad peak between 30 and 45° is observed even for lower concentrations (4 %, 2.5 %), indicating very small particles. The maximum of the broad hump does not correspond to the maximum peak positions of the three carbides given in Fig. 5.5b, also after annealing. The bar should indicate that several other carbide peaks with lower intensity appear in this region. A detailed discussion of the XRD pattern of a-C:W films is given in section 5.2.2.

5.2.1.2 Quantification of TiC, VC and ZrC crystallite size

Fig. 5.7 summarizes the crystallite sizes, determined by applying the Scherrer formula (section 4.2.1) for Ti, V, and Zr-doped films. The values are calculated under the assumption that peak

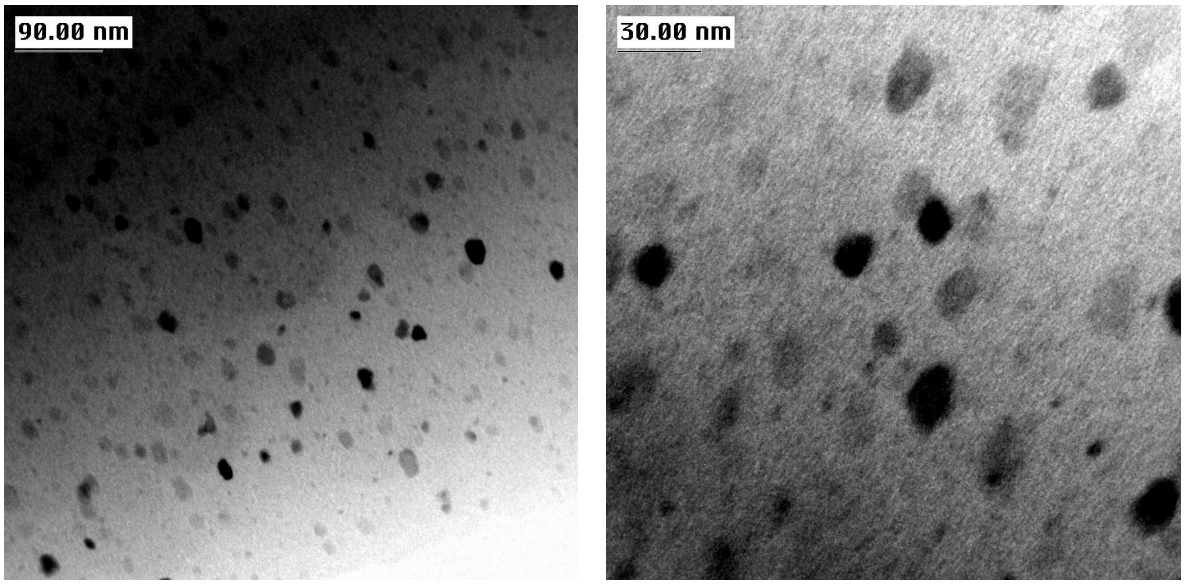

Figure 5.8: *TEM micrographs of a 1.5 % a-C:V specimen annealed to 1300 K. A mean VC crystallite size of 17.2±8.5 nm was determined from TEM analysis.*

broadening is dominated by the small crystallite size (see section 2.1). The error bars only result from the uncertainty introduced by the peak fitting procedure. To get an impression of the signal to background ratio, the intensity ratio from the fitted peak to the linear background at the peak maximum are given for films with ≈8 % metal concentration.

The 1 % a-C:Ti and 2 % a-C:Zr samples do not show any unambiguous carbide peaks, therefore no size could be estimated. This is also true for Ti and V-doped samples with low metal content and low annealing temperature. Generally, annealing leads to growth of carbide crystallites. VC crystallites are larger than TiC and ZrC crystallites for similar concentrations and annealing temperatures: For example at 1100 K, 7.5 % a-C:Ti exhibits ≈2 nm crystallites, whereas the carbide size in 8.5 % a-C:V is around 4 nm. For 7 % a-C:Zr, the crystallites are only about 1.5 nm. Fig. 5.7d summarizes all crystallite size data in one plot, which shows that the general trend in crystallite size is ZrC<TiC<VC.

An explanation for this sequence can be given by comparing the carbide melting temperatures, which can be regarded as a measure for the crystallite stability: ZrC (3693 K) > TiC (3340 K) > VC (3103 K) [103]. It is assumed that for crystallite growth the metal has to diffuse through the carbon matrix until it reaches another crystallite which therefore increases in size. Since the crystal stability of VC is lower than for TiC or ZrC, vanadium atoms can leave a crystallite more easily and start to diffuse through the carbon matrix to form larger crystallites. Diffusion of carbidic metal atoms on the nm-scale occurs at temperatures significantly lower than the macroscopic observed carbide melting point. Since the carbide crystallites are very small, the particles exhibit a large relative surface portion. Metal atoms at the surface are weaker bonded, so they can leave the crystallite more easily, i.e. at lower temperatures.

For some samples, crystallite sizes were also determined by evaluating TEM micrographs, given also in Fig. 5.7. Every value is an average of 200-500 analyzed crystallites. They were determined by the diameter of the smallest circle which encloses the carbide particle in a TEM micrograph. Therefore it should be an upper estimate of the particle size. Fig. 5.8 gives two micrographs of a 1.5 % a-C:V layer, Fig. 5.9 shows an 7.5 % doped a-C:Ti sample. Both

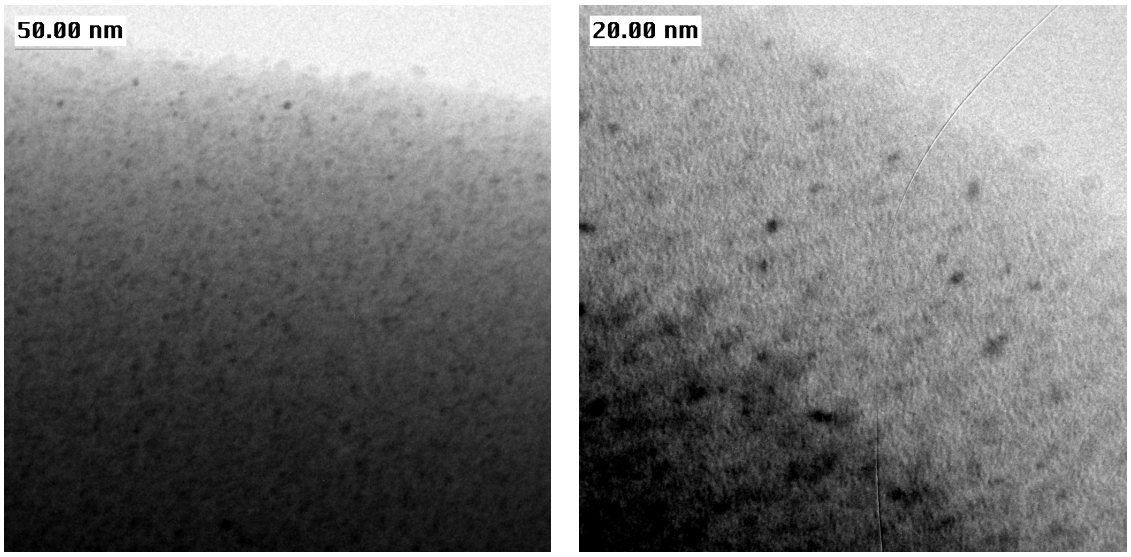

Figure 5.9: *TEM micrographs of a 7.5 % a-C:Ti film annealed to 1300 K. A mean TiC crystallite size of 2.7±0.8 nm was determined from TEM analysis.*

specimen were annealed to 1300 K.

A homogeneous distribution of carbide particles throughout the films can be observed. For the a-C:V samples, TEM analysis gives about 20-40 % larger values as determined by XRD (see Fig. 5.7). For the a-C:Ti sample, the size derived from TEM is about 35 % smaller. It is impossible to estimate the "real" average value. As outlined in section 2.1, different factors can influence the size determined by XRD. In principle, XRD should account for a volume-based average particle size, whereas TEM gives number-based values. One problem in TEM analysis is that only visible particles can be taken into account and particles which are too small to be detected are not included in the analysis. On the other hand, determination of the size distribution is possible. The right picture of Fig. 5.8 particularly shows that the particle size distribution is very broad with a significant number of very small particles. This broad distribution leads to the large spread in the determined average particle size by TEM.

No carbide crystallites could be detected by TEM in 7 % a-C:Zr and 7.5 % a-C:Ti samples annealed to 1100 K, which should be due to a too small particle size. With the applied microscope, particles smaller than 2 nm seem hardly to be resolved.

Considering all uncertainties, the deviation in average size determination for TEM and XRD is reasonable. Nevertheless, the fact that the average size determined by TEM for the a-C:Ti film is significantly smaller compared to XRD remains unclear. No principle difference is expected to the case of a-C:V films. More TEM investigations on a-C:Ti samples have to be performed to clarify if this has a real physical background or is related to an experimental artifact. Nevertheless, the development of crystallite growth can be investigated quite accurately with XRD (Fig. 5.7).

An interesting observation is, that the lowest V concentration (1.5 %) leads to the largest VC crystallites after annealing to 1300 K. This is confirmed by XRD and TEM. No explanation can be given for this effect.

One aspect was not addressed up to now. It is obvious from the above shown results, that some samples (generally with low metal content and low annealing temperatures) remain

completely X-ray amorphous in a XRD pattern. This could mean that the metal is in an amorphous state, but it can not be excluded that such samples exhibit also carbide crystallites, but too small to give a measurable diffraction peak or contrast in TEM. On the other hand, if the diffraction pattern shows a weak carbide signature, it can not be excluded that only a small amount of the metal is located in a carbide crystallite, and the majority is in an amorphous environment. In section 5.2.3 XAFS measurements will be presented which show that an amorphous appearance in XRD can be a result of too small crystallite size **or** an atomic disperse Ti distribution which results in an amorphous Ti environment without long-range order.

5.2.2 Investigation of carbide phase in a-C:W

As outlined before, the diffraction pattern of as-deposited a-C:W films show a broad hump, whose maximum does not correspond to the peak maxima of tungsten carbides. This is shown in detail for XRD patterns of the 9.5 % W-doped film in Fig. 5.10. The peak positions with relative intensities of three possible carbide phases W_2C, WC and WC_{1-x} are given for comparison. The stoichiometry of the high temperature phase WC_{1-x} is reported for x=0-0.4 [100,146], x=0.5-0.63 [147] and x=0.58-0.6 [148]. The only thermodynamic stable carbide phase which should occur in a C-rich C-W system below 3049 K is WC [149]. Nevertheless, during sputter-deposition, films are formed far away from the thermodynamic equilibrium, thus other (high temperature) phases can be formed by quenching. The diffraction patterns of the a-C:W annealing series show a slight peak shift of the broad maximum from about 36.8° to 38.3° with annealing. Also its FWHM decreases slightly, and two peaks at ≈62 and 75° develop. This two peaks do also not help to clarify phase identification, since all three carbide phases exhibit peaks at about this 2θ angles.

From all three carbides, WC seems to be the most unlikely one, because the second 100 % intensity peak at 48.3° is not observable. The peak maximum of the as-deposited sample is at a similar position as the (111) reflex of WC_{1-x} at 37.0°. Comparable spectra, obtained by Voevodin et al. [100] for W-C/a-C composite films, were interpreted as a result of distorted WC_{1-x} crystallites with strong (111) texture. Nevertheless, this argument alone is not very strong, since it could be also used for assignment with other phases. During electric discharge or ion arc production of tungsten carbides, the WC_{1-x} phase is often formed with the (111) peak observed with higher intensity [150, 151]. Slimani et al. [152] performed a thorough determination of the structure of a W-C layer with 25 % W produced by CVD assisted magnetron sputtering. Based on electron diffraction they report that about 5 nm large WC_{1-x} crystallites have formed, SAXS measurements revealed 1-2 nm large W-rich precipitates. For the latter, a structure similar W_2C or WC_{1-x} was assumed, the presence of WC could be excluded. Schiffmann et al. observed WC_{1-x} crystallites with (111) texture for 55 and 41 % a-C:H:W. But for 25 % W, also a broad peak was observed, which does not fit to the WC_{1-x} pattern.

From the measured a-C:W XRD spectra, the phase of the formed crystallites cannot be deduced, but W_2C or WC_{1-x} seems to be more reasonable than WC. No crystallite size can be given, since the observed signals are likely a result of several overlapping peaks. During annealing, the increased peak intensity and decreased FWHM indicate a temperature-induced ordering. Compared to the other dopants, a-C:W films exhibit high signal intensity in the XRD patterns already after deposition. This may indicate that in a-C:W films a larger amount of order around the W atoms is present compared to the other dopants. Probably very small

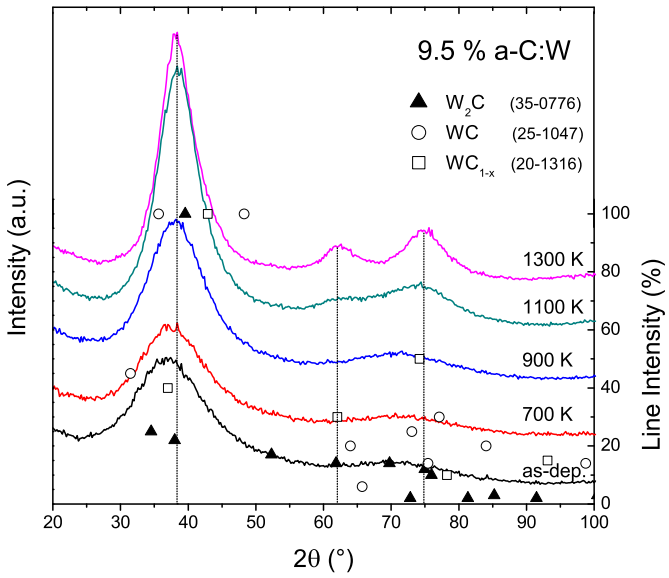

Figure 5.10: *X-ray diffractograms of an 9.5 % a-C:W film, annealed up to 1300 K. The peak positions and relative intensities of W_2C, WC and W_{1-x} are indicated by symbols (JCPDS database [145], PDF card number is given in brackets).*

and distorted carbide particles are formed during the deposition process. Annealing increases slightly ordering and size of this particles. Nevertheless, the intensity (but not the FWHM) of an XRD reflex also depends on the atomic number Z. Assuming similar crystallite sizes and order, the highest peak intensity is expected for tungsten carbides.

The as-deposited films remain amorphous for TEM, as it is obvious from Fig. 5.11. The electron diffraction pattern shows slightly more pronounced rings as for a-C:Ti in Fig. 5.6, indicating a more defined next-neighbor distance. For TEM micrographs of an 1100 K annealed 9.5 % a-C:W film, indication for crystalline particles < 2 nm exist.

To overcome the limitations of XRD, NEXAFS measurements of a-C:W films at the W L_1-edge were performed at ESRF to compare the local electronic environment of W in W-doped films with standard materials. Fig. 5.12 shows W L_1-edge NEXAFS spectra of three 6.5 % a-C:W films (as-deposited and annealed to 900 and 1300 K), a 12.5 % a-C:W film (a *multilayer* specimen with a-C:W between two a-C films, annealed to 1700 K) and three bulk materials: W, W_2C, WC.

The spectra of W, W_2C and WC are well separated from each other and have different shapes. A shift to higher energy is observed in this row, which is in line with the qualitatively increasing formal oxidation state. It is obvious from Fig. 5.12, that the W environment in a-C:W films annealed up to 1300 K is different to WC. But after annealing of a-C:W to 1700 K a phase transformation to WC occurred, which is also confirmed by XRD. The spectrum of the a-C:W sample annealed to 1300 K shows clear correspondence to the spectrum of W_2C. Differences are obvious for the a-C:W sample after deposition and annealed to 900 K. The pre-edge peak feature for the as-deposited sample is similar to that of the W spectrum. This could be interpreted as that during deposition small W-enriched (or C-depleted) carbide clusters have

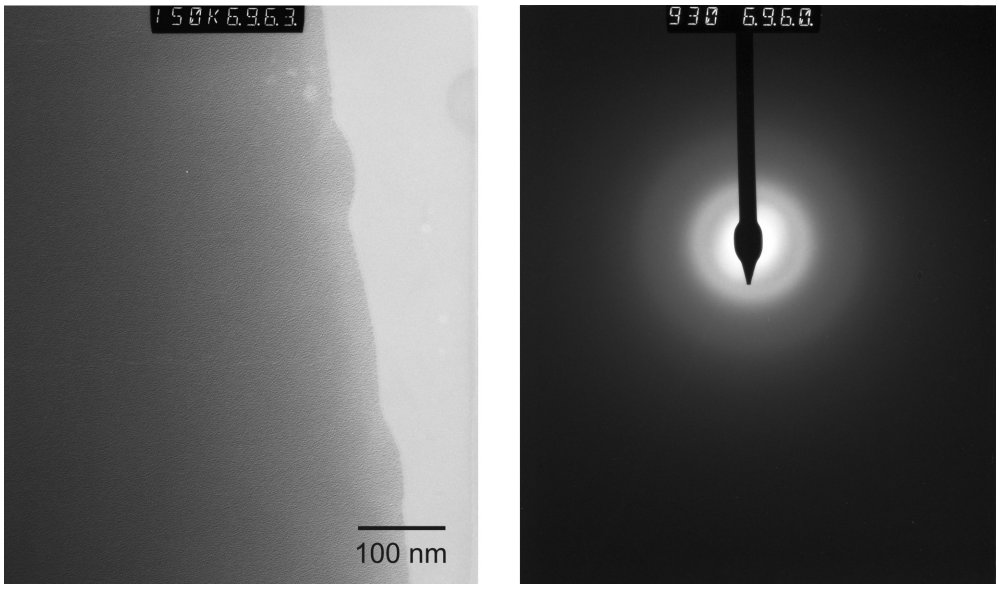

Figure 5.11: *TEM micrograph of an as-deposited 6.5 % a-C:W film. b) Electron diffraction pattern taken from the same image area.*

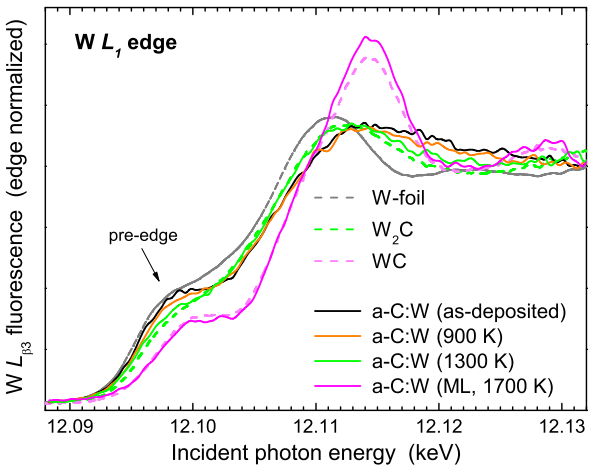

Figure 5.12: *Normalized W* L_1*-edge NEXAFS spectra of different a-C:W films and three reference materials (W,* W_2C *and WC). As-deposited, 900 K and 1300 K annealed a-C:W films have a W content of 6.5 %. A multilayer 12.5 % a-C:W specimen was annealed to 1700 K. Spectra were acquired by detecting the* $L\beta_3$ *fluorescence line.*

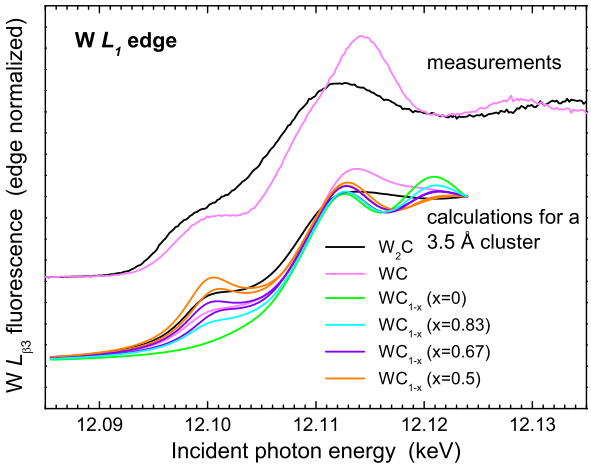

Figure 5.13: *Measured (W_2C, WC) and calculated (W_2C, WC, WC_{1-x}) W L_1-edge NEXAFS spectra. NEXAFS calculations of 3.5 Å clusters were performed by M. Sikora using the program FDMNESS [133]. For WC_{1-x} with x=0.5 and 0.67 two clusters were calculated with a spherically symmetric and asymmetric vacancy distribution. The latter gave a higher pre-edge intensity.*

formed. In general, distortion, stoichometry inhomogeneity or very small cluster size could be responsible for the spectral deviations of as-deposited and 900 K annealed a-C:W from the W_2C spectrum.

Nevertheless, also another crystallite phase (i.e. WC_{1-x}) could be responsible for the differences. Since no standard material of WC_{1-x} was available for measurement, NEXAFS spectra of 3.5 Å large clusters were calculated using the code FDMNES, shown in Fig. 5.13.

Comparison of the calculated and measured W_2C and WC spectra show qualitative agreement. For WC, the less pronounced maximum is due to the small cluster size, as shown for a calculation with a larger cluster. The main difference for W_2C to the measured spectrum is a slight energy shift. Simulated spectra of the WC_{1-x} clusters with different stoichometry exhibit two maxima around 12.113 and 12.120 keV with a minimum in between. This is the main difference to W_2C. The pre-edge feature around 12.100 keV is only visible for WC_{1-x} with x $\geq$0. Two calculations were performed for WC_{1-x} with x=0.5 and 0.67. One with a spherically symmetric vacancy distribution, the other one with a more asymmetric vacany arrangement. The latter gave higher pre-edge intensity.

Since the calculations show that the spectral shape of W_2C and WC spectra can be reproduced, it is assumed that this is also the case for WC_{1-x}. The as-deposited and 900 K annealed a-C:W spectra in Fig. 5.12 did not show any minimum similar to the calculated spectra of WC_{1-x}. This is an indication that the local W environment in this a-C:W samples is similar to W_2C, but with less order compared to the 1300 K annealed specimen. From inspection of the pre-edge region the existence of $WC_{1-x}$with x=0 can be excluded as dominating species.

On the other hand, all calculations were performed for very small clusters with perfect geometry and stoichometry. It can not be excluded that distortion or increase of cluster size alters the shape of the WC_{1-x} spectra after the edge to become similar to W_2C (i.e. more smooth). The more intense pre-edge region for the a-C:W film after deposition could therefore

also be interpreted as an indication for WC_{1-x} with x >0. Unfortunately, both the WC_{1-x} stoichiometry and the vacancy distribution is unknown, but the calculations show that both have strong influence on the pre-edge region.

Summarizing the XRD and NEXAFS results, a definite answer about the carbide phase in a-C:W for annealing up to 1100 K can not be drawn. For as-deposited a-C:W, the broad peak in the X-ray diffractograms could be a result of very small and distorted particles and/or the occurrence of a mixture of W_2C and WC_{1-x} (x >0) phases. NEXAFS indicates that the local W environment is similar to W_2C after annealing to 1300 K. XRD and NEXAFS confirm that the WC phase has formed after annealing to 1700 K.

5.2.3 XAFS investigations

As mentioned above, XRD is only sensitive to crystalline structures. But in principle, two explanations are possible for the X-ray amorphous appearance of an a-C:Me film: The carbide crystallite size is too small to give measurable diffraction peaks or an amorphous state on the atomic scale, i.e. the metal is distributed atomically disperse. Therefore, XAFS measurements of a-C:Me films were performed at HASYLAB and the processed data is compared with measured carbide standards and calculated spectra. XAFS is a local atomic probe and only the next neighbors in a few Å distance contribute to the signal (section 2.3.1). First, spectra for 7.5 % a-C:Ti and as-deposited a-C:Ti are presented in detail, then mainly the differences for the other dopants are discussed.

5.2.3.1 Annealing series of 7.5 % a-C:Ti

Fig. 5.14a shows Ti *K*-edge XAFS spectra of an annealing series of 7.5 % a-C:Ti and a spectrum of pure TiC. For the as-deposited sample only a broad peak is observable after the edge, representing the next neighbor of Ti, which should be a carbon atom. Annealing to 700 K does not alter the spectrum significantly, but after annealing to 900 K a peak evolves from the shoulder after the edge similar to TiC. Nevertheless, clear correspondence to the TiC standard spectrum is evident only after annealing to ≥1100 K. From the qualitative comparison of the XAFS spectra it is evident, that no carbide environment is formed around the Ti atoms after deposition and annealing to 700 K. After annealing to >1100 K Ti atoms are in a TiC-like bonding configuration. An intermediate-state appears for 900 K. This could be interpreted as that some small carbide crystallites have formed (also indicated by the weak diffraction peaks in Fig. 5.5a), but a large fraction of Ti atoms is still in an environment which is better described as amorphous.

The near-edge region (NEXAFS) and, therefore, the position of the absorption edge is sensitive to the local electronic structure of the absorber atom, and the edge position can be regarded as a *chemical shift* [70]. Comparison of the edge position gives a qualitative representation of the electron density localized at the Ti atom. For all spectra shown in Fig. 5.14a, the edge energy E_0 was determined by setting it to the value of the half edge step intensity [129]. This is presented as inset in Fig. 5.14a. A clear trend of increasing E_0 for higher annealing temperatures is visible. This corresponds to a stronger Ti–C interaction, i.e. decreased electron density at Ti, which is in line with stronger TiC-like bonding environment for higher annealing temperatures. For the sample annealed to 1300 K, the position is virtually identical to TiC. The edge position for the as-deposited sample is far away from pure Ti

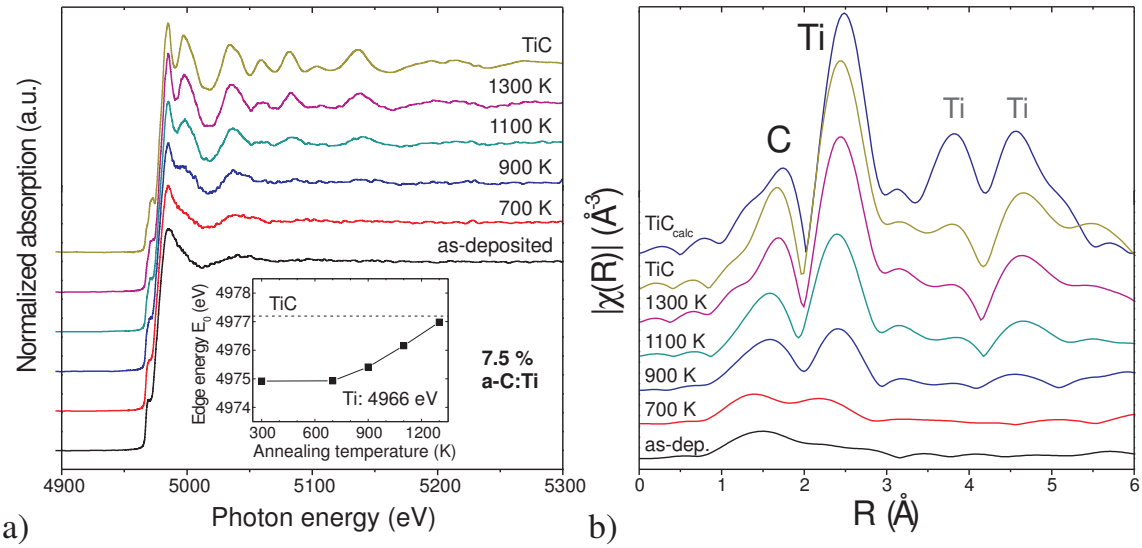

Figure 5.14: *a) Ti K-edge XAFS spectra of 7.5 % a-C:Ti and TiC, normalized to unit edge step. As inset, the edge energy E_0 is shown for all spectra. The values were derived by determining the edge position at the half intensity of the normalized edge step. b) EXAFS data presented as $\mid \chi(R) \mid$ in real space (after Fourier transformation of $k^2\chi(k)$ for k=2-8.5 Å^{-1}, not phase shift corrected). The top graph was derived by a FEFF calculation of a 6 Å TiC cluster [71].*

(4966 eV), which shows that titanium is not present in metallic clusters, but forms Ti–C bonds already during deposition.

In Fig. 5.14b the EXAFS part is shown after Fourier transformation of $k^2\chi(k)$ as $\mid \chi(R) \mid$, where the x-axis represents the radial distance R from a Ti atom in real space. In this graph also a calculated 6 Å large TiC cluster is included. The graphs are shifted by ≈0.4 Å to lower R, because of the scattering phase shift [70]. To obtain more reasonable distances the phase shift of ≈0.4 has to be added to the x-axis (the Ti-C distance in TiC is 2.16 Å). For the determination of exact atom distances fitting to a model has to be performed (section 2.3.1).

Starting with the calculated spectrum (TiC_{calc}), the peaks at 1.7 and 2.5 Å represent the first two coordination shells of Ti which means 6 C atoms as first and 12 Ti atoms as second neighbor. Due to the lower scattering amplitude of C compared to Ti and overlapping of different (multiple) scattering paths, only the next Ti neighbors are visible as maxima. The decrease in intensity after 5 Å is due to the small size of the calculated cluster.

The measured spectrum of the TiC standard fits well to the calculation, the only difference is the decrease in intensity with R, which is probably due to experimental damping and differences to the perfect TiC stoichometry used for the calculation.

For $\mid \chi(R) \mid$ of a-C:Ti after deposition, only the first neighbor (C) is visible. Additionally, the maximum is at lower distance compared to TiC, indicating no TiC-like coordination. Annealing to 700 K leads to the evolution of a second peak, also at lower distance compared to TiC. After annealing to 900 K the first two peaks are at similar distance as for TiC, indicating that formation of carbide crystallites has started. Also for R >3 Å the spectral shape is similar. Nevertheless, the second Ti neighbor has much lower intensity compared to TiC, which indicates a very small TiC crystallite size with a large fraction of Ti atoms at the surface. For 1100 K and 1300 K the atomic environment is clearly similar to TiC.

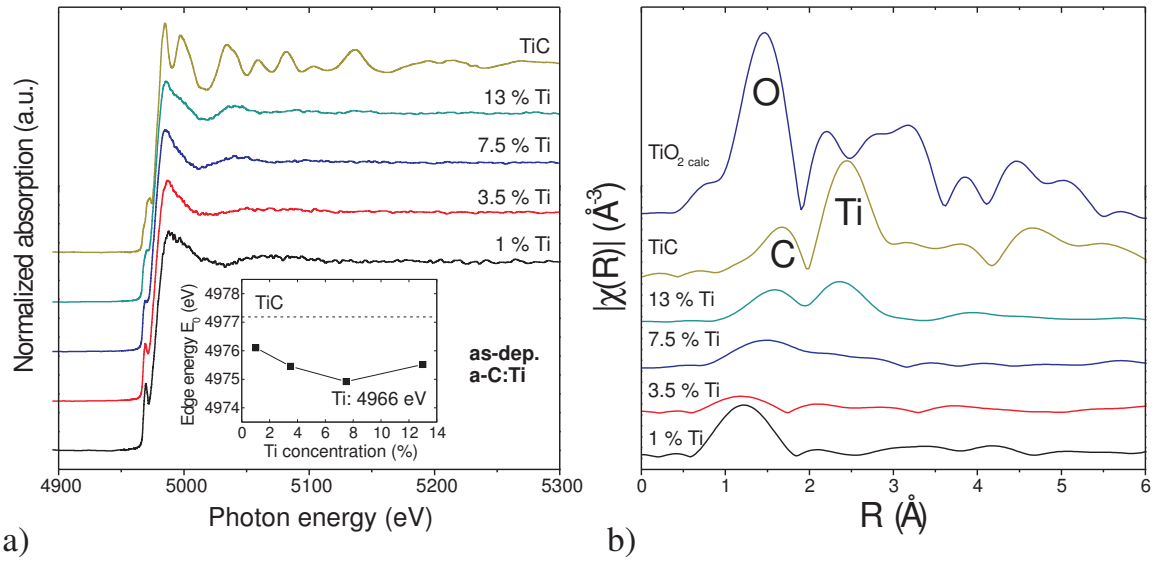

Figure 5.15: *a) Normalized Ti* K*-edge XAFS spectra of as-deposited a-C:Ti and TiC. As inset, the edge energy E_0 is shown for all spectra. b) EXAFS data presented as | $\chi(R)$ | in real space (after Fourier transformation of $k^2\chi(k)$ for k=2-8.5 $Å^{-1}$, not phase shift corrected). The top graph was derived by calculating a 6 Å TiO_2 cluster (Rutile modification) using FEFF.*

5.2.3.2 As-deposited a-C:Ti with various Ti concentrations

In Fig. 5.15a XAFS spectra of as-deposited a-C:Ti specimens with different Ti concentrations are presented. All spectra show only one peak after the edge, which is most pronounced for the 13 % doped sample, with the highest Ti concentration. Interestingly, the spectrum of the 1 % doped sample exhibits a more pronounced maximum in the EXAFS region compared to 3.5 % a-C:Ti, indicating a more defined next neighbor. The inset of Fig. 5.15a presents the edge energy as function of Ti concentration. In contrast to the annealing series in Fig. 5.14a, no linear increase is visible. The 1 % Ti-doped sample exhibits the highest value, which indicates the strongest electron transfer from Ti to the next neighbor for that sample. For 7.5 % a-C:Ti a minimum is reached. Comparing the EXAFS data after Fourier transformation, | $\chi(R)$ | in Fig. 5.15b, the 1 % a-C:Ti exhibits a intense first peak, at a smaller R compared to the 7.5 % a-C:Ti and TiC. For the 3.5 % a-C:Ti the first maximum is at the same distance but with lower intensity.

This more intense peak at lower R for 1 % a-C:Ti can be explained when considering the oxygen content, which is about 2 %. Since the metal has a strong affinity to form an oxide, the oxygen will be mainly localized around the Ti atom after film deposition. For low metal concentrations, this means that the first coordination shell is dominated by oxygen. For 1 % a-C:Ti the stoichometry ratios of Ti and O would allow formation of TiO_2. In Fig. 5.15b, the calculated | $\chi(R)$ | for TiO_2 (rutile structure) is added. The first O shell for TiO_2 is at lower R compared to first C shell for TiC. Therefore, the strong first shell peak observed for 1 % a-C:Ti is probably due to local Ti–O bonding. Formation of larger TiO_2 crystallites is unlikely due to the low intensity at higher R. The local Ti–O bonding also explains the higher edge-energy for the 1 % a-C:Ti, since O has a higher electronegativity, and the Ti–O bond a higher ionic fraction. For the 3.5 % a-C:Ti spectrum in Fig. 5.15b probably a mixed C/O first shell leads

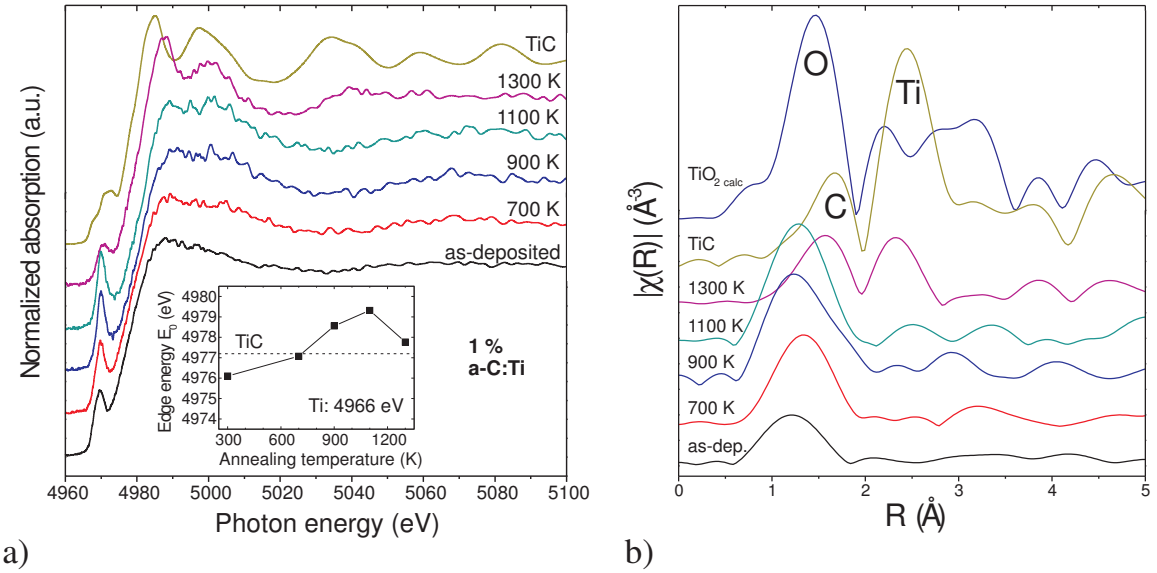

Figure 5.16: *a) Normalized Ti K-edge XAFS spectra of annealed 1 % a-C:Ti and VC. As inset, the edge energy E_0 is shown for all spectra. b) EXAFS data presented as | $\chi(R)$ | in real space (after Fourier transformation of $k^2\chi(k)$ for k=2-8.5 $Å^{-1}$, not phase shift corrected). The top graph was derived by calculating a 6 Å TiO_2 cluster (Rutile modification) using FEFF.*

to a less pronounced first maximum in | $\chi(R)$ |. For 13 % a-C:Ti, the first shell is at the same distance as in TiC, and the second shell (Ti) appears. But the lower relative intensity of the second shell and higher R compared to pure TiC indicates that the Ti environment for R >3 Å is mainly amorphous.

Now, the developing of the edge energy in Fig. 5.15a can be explained as follows: For 1 % Ti, the first shell mainly consists of O atoms, and a high E_0 is observed. With increasing Ti concentration (but similar O content) more C atoms are in the first shell leading to less electron transfer from Ti and decreasing E_0. For 13 % Ti, a partly TiC-like first and second coordination shell is present, with a more defined and stronger Ti-C bonding, leading to a higher E_0 compared to the 7.5 % a-C:Ti.

Annealing of the 1 % a-C:Ti sample does not lead to the formation of a TiC-like Ti environment up to 1100 K. From analysis of the near-edge region in Fig. 5.16a it is obvious that annealing is correlated with an increase of the edge energy E_0 even beyond the value of TiC up to 1100 K. Also the pre-edge feature at 4970 eV is developing with annealing temperature, but does not correspond to TiC. After annealing to 1300 K the near-edge region becomes more similar to TiC and E_0 shifted to a lower value. From the extracted | $\chi(R)$ | in Fig. 5.16b, it can be observed that the first coordination shell (oxygen) appears with higher intensity up to 1100 K, which is due to higher order and/or increasing coordination number. The larger Ti-O interaction is responsible for the increasing E_0. After annealing to 1300 K, the distance of the first coordination shell is slightly higher. This is consistent with the beginning of carbide formation, leading to carbon in the first-shell, a Ti-C distance similar to TiC and an E_0 value similar to TiC. Nevertheless, the second shell (Ti) is not well developed, which indicates a very small particle size (i.e. a large fraction of Ti at the surface of crystallites).

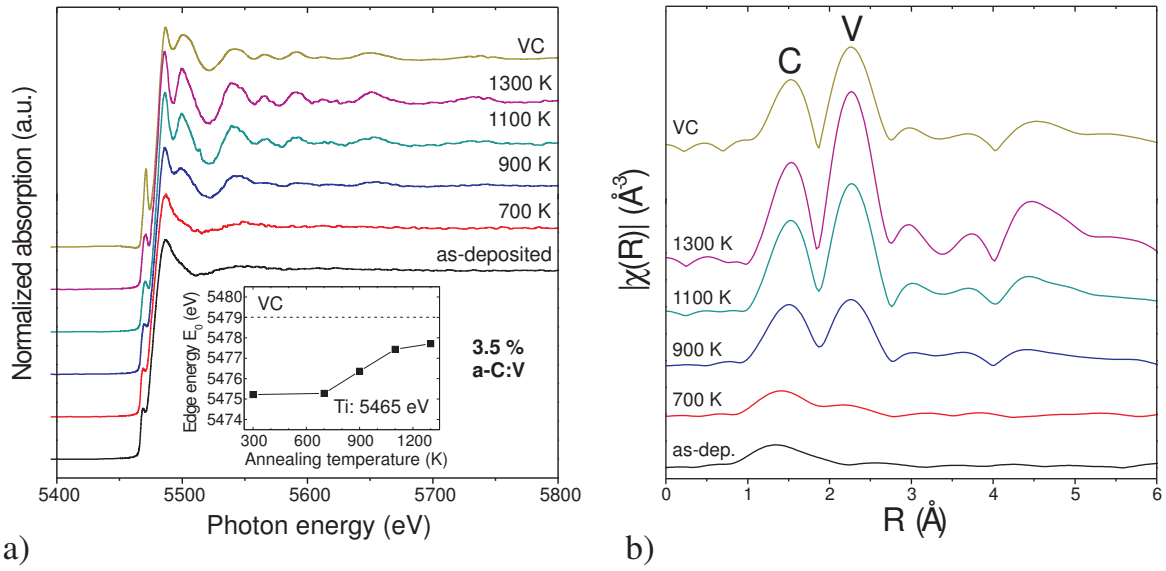

Figure 5.17: *a) Normalized V K-edge XAFS spectra of annealed 3.5 % a-C:V and TiC. As inset, the edge energy E_0 is shown for all spectra. b) EXAFS data presented as | $\chi(R)$ | in real space (after Fourier transformation of $k^2\chi(k)$, for k=2-8.5 Å^{-1}, not phase shift corrected).*

5.2.3.3 Investigation of a-C:V and a-C:Zr

In general, a-C:V and a-C:Zr films show a similar temperature-induced structuring compared to a-C:Ti. Fig. 5.17 shows data for 3.5 % a-C:V. An increase in E_0 with annealing is observed indicating higher V-C interaction, but the value for VC is slightly higher compared to the 1300 K annealed sample. From | $\chi(R)$ | in Fig. 5.17b, VC-like coordination of V is observed for ≥900 K. With higher temperature the intensity of the second neighbor (V) increases. Its lower intensity for 1300 K compared to VC could be explained by experimental damping during measurement of the carbide using electron yield. Since this detection method is surface sensitive, contribution of an oxidized surface layer might also be an explanation.

Similar evolution of | $\chi(R)$ | is observed for all a-C:V films, also for the 1.5 % a-C:V. In contrast to the 1 % a-C:Ti no significant influence of oxygen is observed. This can be explained by the higher V/O ratio compared to Ti/O (Tab. 5.1) and the lower oxygen affinity of V in contrast to Ti (ΔG_f=889 kJ mol^{-1} for TiO_2 and 710 kJ mol^{-1} for $\frac{1}{2}$ V_2O_5 at 300 K). Fig. 5.18 shows data for as-deposited a-C:V samples. E_0 remains almost constant, a VC-like coordination is achieved for doping with 19 % V.

This example shows, that relying only on information provided by XRD is not always justified. Both the as-deposited 19 % and 8.5 % a-C:V specimens give a measurable diffraction peak. But comparison of | $\chi(R)$ | in Fig. 5.18b shows, that in average, no proper VC-like coordination is present in the 8.5 % V sample. The XRD signal can explained by the existence of a low amount of small and distorted VC crystallites, but the majority of V is in amorphous environment.

Only limited XAFS data is available for a-C:Zr samples. Measurements of different campaigns are presented in one graph, and annealing times vary between 15 minutes and 2 h. Therefore, no discussion of E_0 is presented, because this parameter is very sensitive on the experimental conditions. Fig. 5.19a shows | $\chi(R)$ | for an annealing series of a 14 % a-C:Zr

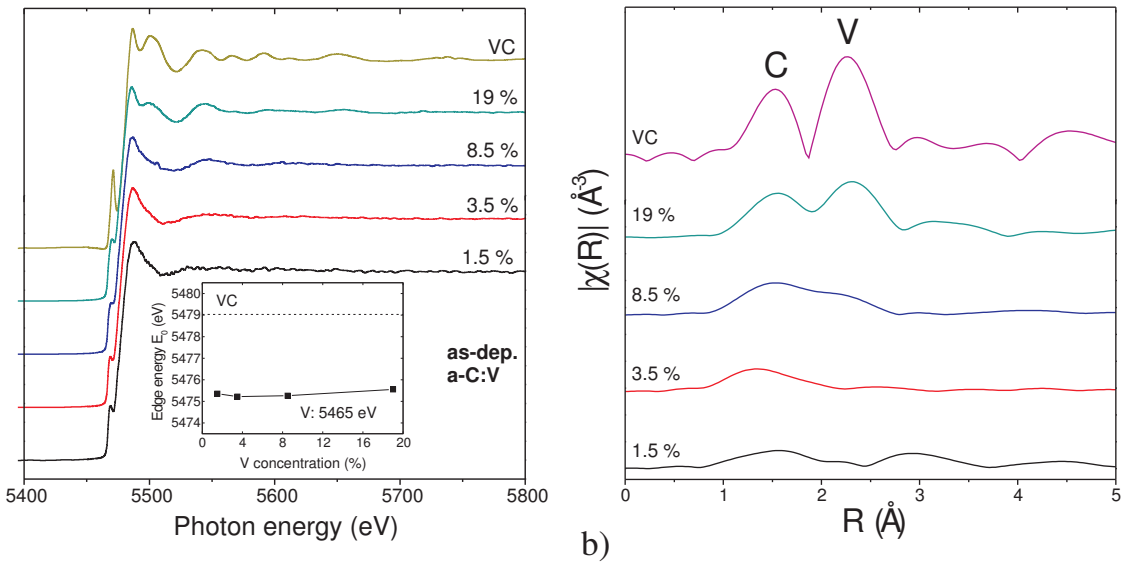

Figure 5.18: *a) Normalized V* K*-edge XAFS spectra of as-deposited a-C:V and VC. As inset, the edge energy E_0 is shown for all spectra. b) EXAFS data presented as | $\chi(R)$ | in real space (after Fourier transformation of $k^2\chi(k)$, for k=2-8.5 Å^{-1}, not phase shift corrected).*

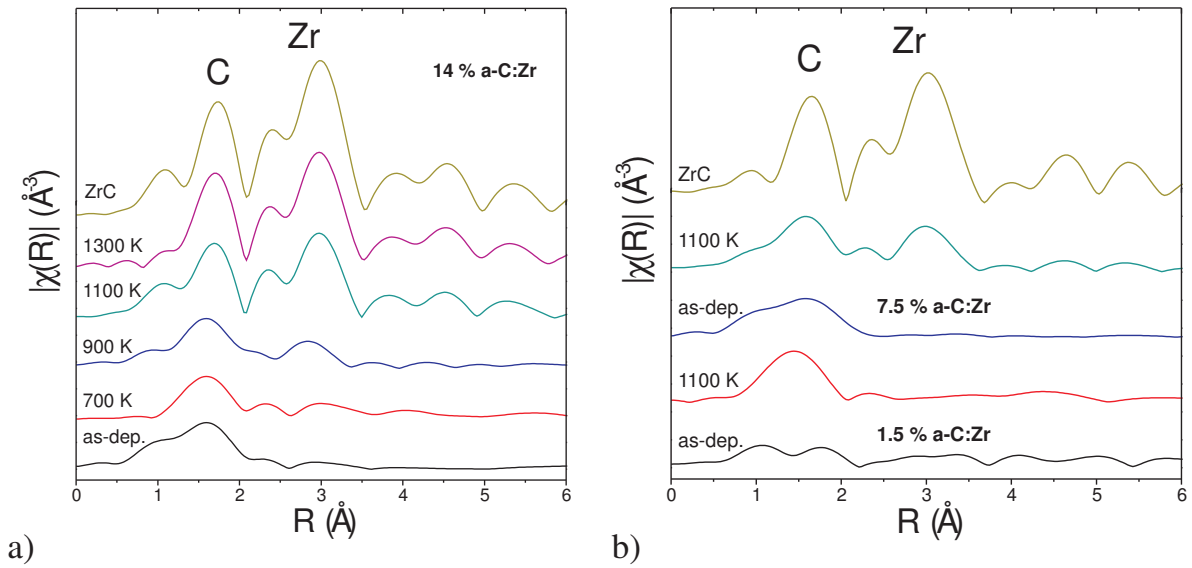

Figure 5.19: *a) | $\chi(R)$ | for an annealing series of a 14 % a-C:Zr multilayer sample and ZrC (after Fourier transformation of $k^2\chi(k)$, for k=2-8.5 Å^{-1}, not phase shift corrected). Different annealing times were used (700, 1100 K: 2h; 900, 1300 K: 15 min). b) | $\chi(R)$ | for 1.5 % and 7.5 % a-C:Zr, as-deposited and after annealing to 1100 K for 15 min.*

multilayer specimen. The first neighbor (C) is present with relatively high intensity already after deposition, indicating a strong Zr–C interaction. A clearly developed ZrC-like second shell (Zr) is only observed after annealing to 1100 K, but probably for some Zr atoms also at lower temperatures. The two maxima representing Zr seem to be already present with low intensity in the as-deposited sample. $\mid \chi(R) \mid$ for the as-deposited sample of 7.5 % a-C:Zr shows no indication of the second coordination shell (Fig. 5.19b). This is in contrast to the crystallinity detected by XRD in a 7 % Zr doped sample (see Fig. 5.7). The low amount of very small ZrC crystallites give rise to a diffraction peak, although the majority of Zr is in amorphous environment.

For a 1.5 % doped a-C:Zr, no ZrC-like environment is created after annealing to 1100 K, as shown in Fig. 5.19b. Similar to 1 % a-C:Ti, an ordered oxygen environment is probably present in the first shell, but also without formation of larger oxide particles as indicated by the low intensity at R >2 Å. The low intensity of the next Zr neighbor after annealing of the 7.5 % a-C:Zr sample is in line with the generally small ZrC particle size in annealed a-C:Zr films, determined by XRD (Fig. 5.7).

5.2.3.4 Investigation of a-C:W

As outlined in section 5.2.2, it is not possible to unambiguously define the crystallographic phase of formed tungsten carbides in a-C:W films. Most likely, during deposition very small and strongly distorted carbide particles are formed which are possibly a mixture of different phases. Analysis of the W L_1-edge NEXAFS spectra in Fig. 5.12 revealed W in W_2C-like local geometry after annealing to 1300 K. NEXAFS spectra at the W L_3 edge (as measured at HASYLAB) were not very sensitive on the local W symmetry. The edge is dominated by a strong feature (the so-called *white line*, see Fig. 5.20a) due to transitions into d levels. Therefore, the NEXAFS region is not a good measure for slight changes of the local W-C interaction, and an evolution of E_0 is not considered.

Fig. 5.20 shows XAFS spectra and the corresponding $\mid \chi(R) \mid$ for an annealing series of a 9.5 % a-C:W sample. The XAFS spectra show only small temperature-induced changes, the spectrum for the as-deposited specimen already shows a relatively strong maximum after the white line. This indicates strong W-C interaction already present after deposition. The $\mid \chi(R) \mid$ is dominated by an intensive first maximum at low temperatures. No indication for a defined second neighbor exists up to 700 K. Since the samples do not appear amorphous in XRD (very broad, but intensive features), this shows that a high degree of disorder and/or different phases are present in very small carbide particles. This damps the EXAFS quickly after the first atomic neighbor. After annealing to 900 K, the second neighbor (W) seems to appear. As for Zr, scattering at W gives two maxima in $\mid \chi(R) \mid$, which is obvious for the graph of the W_2C standard. A clear correspondence to the first two neighbors with W_2C is only obvious after annealing to 1300 K, which is in line with the L_1 NEXAFS presented in Fig. 5.12. Nevertheless, the first maximum of the W neighbor is still not as intensive as for the W_2C standard, which can be explained by a very small particle size and/or still a high degree of disorder. Comparison of spectra of as-deposited samples with different concentrations show no significant variation from the 9.5 % a-C:W spectrum. For a sample with 14.5 % W, a W_2C like coordination seems to be present already at 1100 K. At lower concentrations (2.5 %, 4 % W) annealing to 1300 K leads to W_2C-like maxima of $\mid \chi(R) \mid$ for the first two coordination shells, but with much lower intensity for W. Generally, annealing leads to ordering of the atomic W environment, but to a much lower extend compared to the other dopants. Low

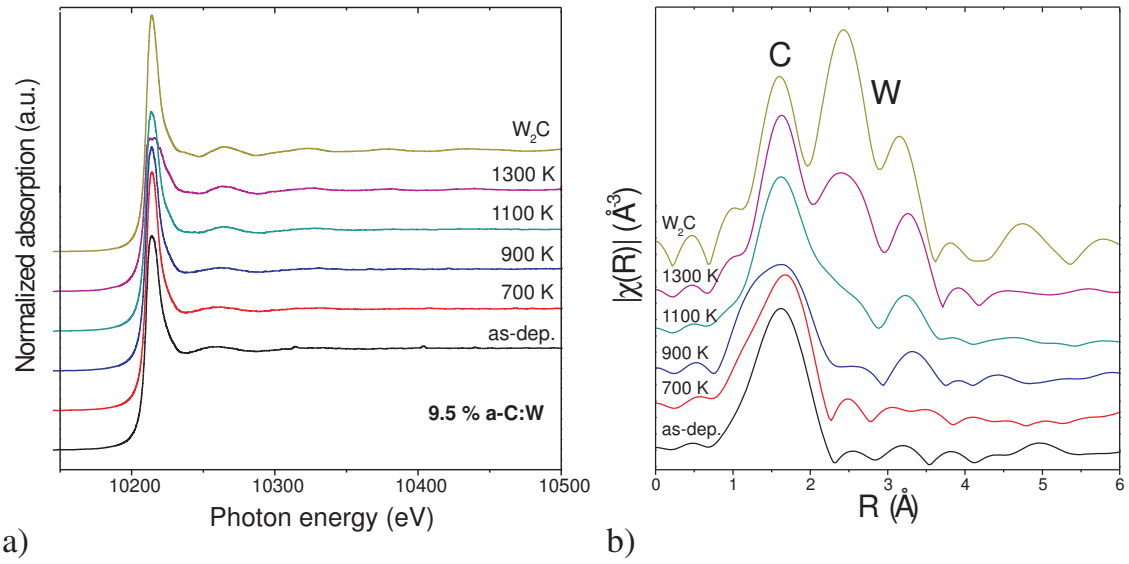

Figure 5.20: *a) Normalized W L_3-edge XAFS spectra of 9.5 % a-C:W and W_2C. b) EXAFS data presented as | $\chi(R)$ | in real space (after Fourier transformation of $k^2\chi(k)$, for k=2-8.5 $Å^{-1}$, not phase shift corrected).*

atomic mobility of W in a-C seems to be responsible.

5.2.3.5 Summary of XAFS investigation

For a-C:Ti and a-C:V, the results of qualitative comparison of | $\chi(R)$ | are summarized in table 5.2. (-) indicates amorphous metal environment, (++) a well-developed carbide coordination. (∘) gives an intermediate state, where the second shell starts to evolve. The results show that the indication for crystallinity received by XRD gives quite a good indication about crystallinity in the films. Nevertheless, some deviations occur, e.g. for the 1100 K annealed 3.5 % a-C:Ti sample, where definitely a TiC-like environment is present, but the particles are probably too small to give a distinct diffraction peak in XRD.

For a-C:Zr, the results indicate a similar behavior as for a-C:Ti. This is reasonable due to their chemical affinity, as they are both elements of the same group in the periodic table. As for 1 % a-C:Ti, also the 1.5 % Zr-doped sample has oxygen present in the first shell up to 1100 K.

The XAFS results for a-C:W show a different behavior compared to the other dopants. A very strong local W-C interaction is present already in the as-deposited samples but annealing does not lead to the formation of larger particles of a defined carbide phase. The W environment is characterized by strong disorder up to annealing to 1100 K. Nevertheless, it has to kept in mind that the XAFS technique gives information about the average over all W atomic environments. Since XRD gives evidence of significant crystallinity in the samples, the XAFS results can also be interpreted as result of a mixture of different crystallite phases with different W coordination. This would explain the damped | $\chi(R)$ | for R >2 Å. The average C-W distance is similar in all carbide phases, therefore | $\chi(R)$ | has a strong maximum around 1.5 Å. But for larger scattering distances, the | $\chi(R)$ | is strongly diminished, due to different crystalline environments and the probably large amount of disorder present in the crystallites.

Table 5.2: *Summary of atomic metal environment for a-C:Ti and a-C:V films, derived from qualitative analysis of | χ(R) |. The symbols indicate an amorphous metal environment (−), a well-developed carbide-like coordination (+ / ++) and an intermediate state (∘). Indicated by (X) is the lowest temperature, for which the samples exhibit crystallinity in XRD. Oxygen coordination is indicated as Ti-O for 1 % a-C:Ti.*

a-C:Ti	as-dep.	700 K	900 K	1100 K	1300 K
1 %	Ti-O	Ti-O	Ti-O	Ti-O	−∘
3.5 %	−	−	∘	+	++ (X)
7.5 %	−	−∘	+(X)	++	++
13 %	−∘	+(X)	+	++	++

a-C:V	as-dep.	700 K	900 K	1100 K	1300 K
1.5 %	-	-	∘ (X)	+	++
3.5 %	-	∘	+(X)	++	++
8.5 %	∘ (X)	+	++	++	++
19 %	+(X)	++	++	++	++

Therefore, some uncertainty remains for the description of the phase and atomic environment in a-C:W samples. Most probably, distorted tungsten carbide crystallites are formed already during deposition. Annealing to 1300 K leads to an ordering to a W_2C-like coordination.

5.2.4 XES investigations

In contrast to well-developed and frequently used techniques like XRD, XAFS and XPS, X-ray emission spectroscopy (XES) is still under development and has not been applied for the analysis of a-C:Me films up to now. XES measurements were performed at ESRF on a-C:V films in order to test if the "ligand approach" described in section 2.3.2 could be used to quantify the amount of V atoms in carbide environment. This would give the possibility to gain similar information as in a XPS measurement, but being not restricted to the surface-near region. The investigated V Kβ satellite lines arise from metal and ligand electrons contributing to the p density of occupied states [74], as described in section 2.3.2.

Fig. 5.21a shows XES spectra for several vanadium standard materials: V metal, VC and V_2O_5. It is clearly visible that for the carbide and oxide, the Kβ" peak appears at different energies, depending on filling of the core hole by a 2p electron of the carbon or oxygen ligand. The K$\beta_{2,5}$ peak probes the HOMO, the highest occupied molecular orbital. Therefore, the position shifts for the different compounds. Its intensity is a measure for the amount of V orbitals in p symmetry contributing to the HOMO and should reflect the amount of V atoms contributing to carbide or oxide clusters.

Fig. 5.21b shows the V Kβ satellite lines region for 3.5 % a-C:V annealed up to 1300 K. Annealing to 700 K leads to decreased intensity at energies characteristic for oxygen ligands. A distinct carbon ligand peak is observed for the samples annealed to ≥900 K with increasing

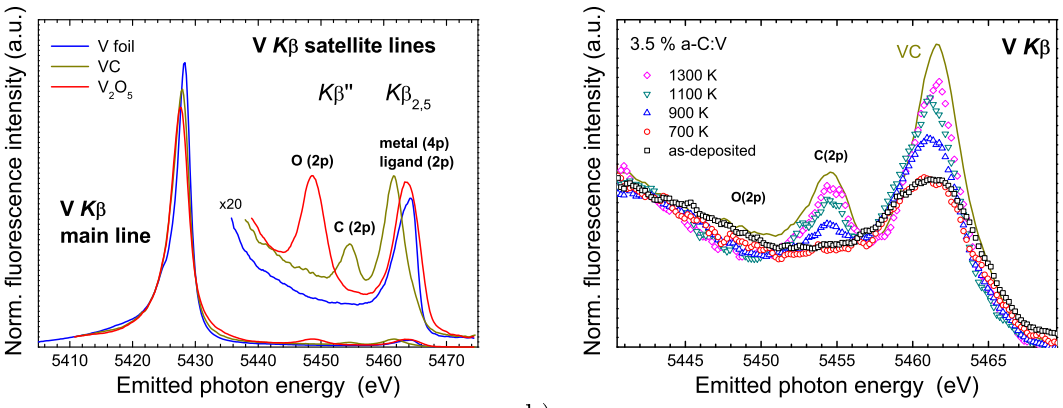

Figure 5.21: *a) X-ray emission spectra of V standard materials: V metal, VC, V_2O_5. The latter is the most stable oxide with V having the formal oxidation number +5. b) XES spectra for an annealing series of 3.5 % a-C:V and VC. All spectra were normalized to the area of the complete Kβ region.*

intensity, and also the K$\beta_{2,5}$ peak develops with annealing. This corresponds to carbide crystallite formation and crystallite growth and is in agreement with EXAFS results, which indicate that VC-like coordination is present after annealing to 900 K.

Peak fitting was applied to extract quantitative information from the spectra. A fitted spectrum is exemplarily shown in Fig. 5.22a. The fit includes peaks for oxide, carbide, K$\beta_{2,5}$ and a background from the Kβ main line. The peak amplitude of the carbide and oxide peak should give a quantitative measure for the amount of C and O present as ligands of V. The peak intensity of the K$\beta_{2,5}$ peak should be proportional to the VC cluster size [74]. It should be noted that fitting of the V spectrum also required a low intensity of the carbide peak, and for the VC spectrum an low oxygen contribution was included. This might be related to a background intensity which was not taken into account.

Fig. 5.22b presents the fitted peak intensities for 4 different a-C:V films annealed up to 1300 K. An increasing K$\beta_{2,5}$ component is observed with annealing and increasing V concentration. The K$\beta_{2,5}$ intensity equals the value for pure VC for the 19 % a-C:V annealed to 1300 K. The carbide peak intensity also increases with annealing and V concentration. The data points of the carbide peak for 1300 K are an exception. Here, the highest value is obvious for the sample with the lowest concentration (1.5 %). This is in accordance with the unexpected large carbide particle size, observed in this sample by TEM and XRD (see Figs. 5.7 and 5.8). Nevertheless, it remains unclear why this is not reflected in the K$\beta_{2,5}$ peak. For the 1.5 % a-C:V sample at lower annealing temperatures, low peak intensities are derived compared to samples with higher V concentration. This seems to be a result from oxygen contaminations present in the sample, which is also reflected in the oxygen peak amplitude. Interestingly, the O contribution is not strongly reduced even at 1300 K. This would mean, that in the formed VC crystallites oxygen atoms are incorporated, which could not be observed from the XAFS data, probably due to the although high degree of order present in the large carbide crystallites. Nevertheless, the poor signal/noise ratio for this low concentrated sample could also have an influence. A decreasing O peak intensity is found for increasing V content, which is reasonable due to the increasing V/O ratio (Tab. 5.1).

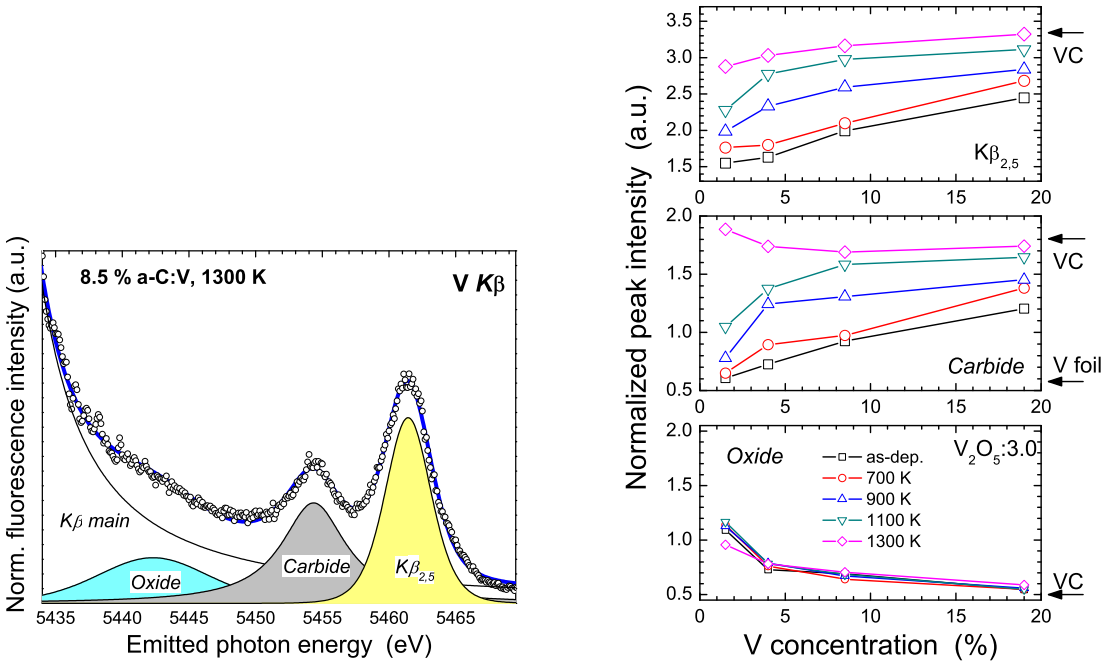

Figure 5.22: *a) Example of a peak-fitted spectrum using PearsonVII profiles for Kβ" O and C peaks and $K\beta_{2,5}$ signal. A background accounting for the Kβ main line is also included. The spectrum is normalized to the whole Kβ area. b) Fitted peak amplitudes for $K\beta_{2,5}$, carbide and oxide as function of V concentration and annealing temperature. The values derived for the standard materials are indicated by arrows on the right axis.*

The main difference in the interpretation of the XES results compared to XAFS is that no abrupt change in the peak intensity of K$\beta_{2,5}$ and Kβ" is observed when carbide crystallite formation starts. Inspection of the $\mid \chi(R) \mid$ for a-C:V and pure VC gives an good indication when – in average – a VC-like coordination is present around a V atom. For that case, $\mid \chi(R) \mid$ is similar for the annealed film and pure VC. In contrast to that finding, the XES fit results show a relatively smooth increase with increasing V concentration and annealing temperature for K$\beta_{2,5}$ and carbide peaks. This seems reasonable, since also in amorphous state, the next neighbor of V is a carbon atom. But nevertheless, only for the 1300 K annealed 19 % a-C:V sample similar values as for the VC standard are derived, although nm-sized carbide crystallites have formed in other films at lower temperature. This finding could be a result of the high sensitivity on the local symmetry. It could be speculated that, even if a VC-like coordination is present, small deviations from a perfect VC structure (which are negligible for qualitative XAFS analysis) could result in lower fluorescence intensities of the Kβ" peaks.

A more detailed analysis of the data and comparison with calculations has to be performed to transform the data in terms of *bonds per atom.* This might be helpful for a more quantitative interpretation. Nevertheless, this first measurements on a-C:Me films show that XES is a sensitive probe for this material and especially the contribution of oxygen is visualized, which is not possible to achieve from a-C:V XAFS data.

5.2.5 Summary

In section 5.2, results of XRD, TEM, XAFS and XES investigations were presented which are now briefly summarized.

Metal bonding

After deposition, the bonding character of the metal is generally carbide-like, the formation of metallic clusters in the carbon matrix can be excluded. For a sample with only 1 % Ti, the XAFS edge position indicates that the metal is mainly bonded to oxygen. For that sample, the bonding state changed to carbidic only after annealing to 1300 K. Fitting of XES spectra revealed, that also in the 1.5 % a-C:V sample significant V–O bonding exist, even after annealing to 1300 K.

Metal distribution

Generally, the atomic metal environment in the as-deposited samples can be characterized as amorphous. Only for high metal concentrations (e.g. 19 % V,) the metal is mainly situated in carbide crystallites. Annealing leads to formation and growth of TiC, VC, ZrC crystallites in the case of Ti, V, and Zr-doping. The occurrence of a carbide peak in the XRD spectrum is in good agreement with the carbide-like local atomic environment, given by EXAFS. Analysis of the FWHM of the carbide peaks can be applied to monitor the carbide crystallite size, which is in the range of several nm. Generally, the crystallite size increases in the order ZrC$<$TiC$<$VC. The largest crystallites are observed for 1.5 % a-C:V, annealed to 1300 K. Evaluation of the crystallite size by TEM gives values in the range of $\pm$40 % of the size determined by XRD.

Tungsten carbide phase

From analysis of a-C:W films by XRD it is not possible to identify the crystallographic carbide phase. Broad peaks in the diffractograms even for as-deposited samples indicate some order, but probably strong distortion and/or a mixture of different carbide phases (W_2C, WC_{1-x}) occur. Therefore, no size determination is possible. For TEM micrographs of a 1100 K annealed 9.5 % a-C:W film, indication for crystalline particles < 2 nm exist. The local atomic environment of the two next atomic W neighbors is similar to W_2C after annealing to 1300 K. Comparison of W L_1-edge NEXAFS spectra with standard materials also revealed local W_2C coordination after annealing to 1300 K. WC is formed in a sample annealed to 1700 K.

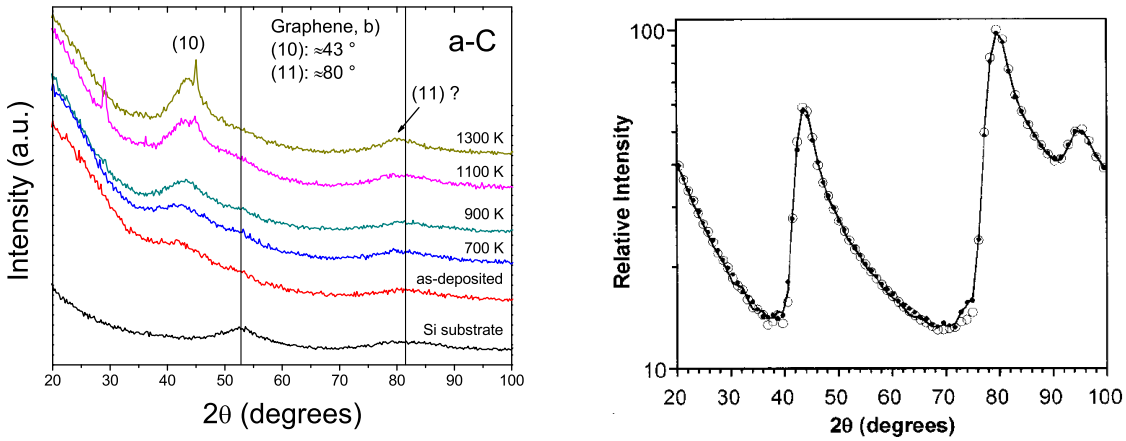

a) b)

Figure 5.23: *a) Gracing incidence XRD patterns of an annealing series of a-C acquired at 1° incidence angle. A diffractogram of an uncoated silicon wafer is given at the bottom. Si was used as substrate material and exhibits an amorphous SiO_2 film on its surface. Spectra are shifted vertically on the linear y-axis. The spikes visible in 1100 and 1300 K spectra are reflections of the Si wafer. b) Scattering intensities from single graphene-layer molecules (taken from [153]).*

5.3 Investigation of the carbon matrix

In this part, investigations of the carbon structure are presented. XRD reveals some crystallinity in a-C, aromatic clustering of the sp^2 phase depends on dopant metal and concentration as shown by Raman spectroscopy. Surface sensitive NEXAFS and XPS experiments are presented at the end of this section.

5.3.1 Crystallinity

X-ray diffraction is commonly used to investigate the crystalline structure of carbon materials like graphites or non-graphitic carbon materials. Due to the lack of long-range order, it is usually not applied for amorphous carbon films. Nevertheless, some features could be detected for a-C when optimizing the experimental setup for the measurement of thin films. Applying gracing incidence with parallel beam geometry, the diffractograms presented in Fig. 5.23a were derived for a-C films annealed up to 1300 K. Measurement of a pure Si wafer proved, that the broad peaks around 53° and 82° are related to the substrate (probably the thin SiO_2 layer on top).

As can be seen in Fig. 5.23a, a peak around 43° originates from a-C. It is already visible in the as-deposited film and develops with annealing temperature. This peak should be related to two-dimensional order in graphene-like regions and is therefore most likely assigned as the (10) reflection of a graphene plane. No reflection resulting from a stacking of graphene planes (the c direction of graphite) is observed, indicating only two-dimensional order. Nevertheless, it cannot be excluded that strong distortion in the stacking of graphene planes could also be responsible. For the spectra of the 1100 and 1300 K annealed samples, also the (11) peak might be visible around 80°.

This results can be explained with the existence of small, two-dimensional graphene-like crystallites in an amorphous, distorted carbon matrix. The (10) peak intensity increases and the peak width slightly decreases with annealing; thermally-induced ordering and growth of graphene-like regions should be primarily responsible, but also the release of strain in a highly stressed material like a-C could contribute. Quantitative analysis of the (10) peak is not possible, because the peak shape is asymmetric, which cannot be resolved in the spectra. This is demonstrated in Fig. 5.23b, where the calculated scattering intensities of small graphene-like molecules (e.g. coronene) are depicted (taken from [153]). A reasonable estimation of the size of graphene-like domains is only possible by analytical simulation of the diffractograms [154].

The observations correspond to STM investigations performed by Cho et al. [155] which showed 2-4 nm large hexagonal honeycomb structures on the surface of a-C films.

Due to overlapping of carbide peaks with the (10) reflection, no information about the graphene-like regions can be gained from diffractograms of a-C:Me. Therefore, Raman spectroscopy is probably the only bulk sensitive technique to investigate structural changes of carbon in doped amorphous carbon films, as outlined in the next chapter.

5.3.2 Aromatic clustering analyzed by Raman spectroscopy

Raman spectroscopy is a commonly used tool to study the structure of amorphous carbon films, because it is a quick and non-destructive method and can be applied in air without any sample preparation. It requires no crystalline order, which makes it applicable to disordered materials like a-C. The intensity ratio of the observed peaks, I(D)/I(G), and the position of the G peak, G_{max}, are parameters linked to the carbon structure as described in section 2.2.2.

After the description of the influence of metal-doping on the Raman signal intensity and the evaluation of different fitting methods, the influence of metal-doping and annealing on the carbon structure is discussed.

5.3.2.1 Raman signal intensity

The most eye-catching difference when measuring metal-doped carbon films is the decreased intensity of the Raman signal compared to undoped carbon. This is demonstrated in Fig. 5.24a for pure a-C and different a-C:Ti films.

The strong decrease in Raman intensity at even low amounts of metal is observed also for doping with V, Zr and W. Increased light absorption in the layer due to metal incorporation would result in a linear dependence of the signal intensity on the metal content. This is not observed. In contrast, at higher metal concentrations saturation occurs. The main reason for the decreased Raman intensity is the increasing surface reflectivity of the films when introducing metals. Therefore, a larger portion of the laser beam is reflected at the surface and can not generate a Raman signal reaching the detector. This was confirmed by reflectometry measurements: Fig. 5.24b shows how the intensity at 1900 cm^{-1} (left y-axis, denoted as background level) is correlated with the increase of reflectivity (right y-axis, given relative to a-C). For reflectometry measurements a wavelength of 515 nm was chosen, according to the Raman laser wavelength of 514.5 nm.

The different Raman signal intensities also reveal the need of peak fitting to separate the contribution of D and G peak for different spectra, which is shown in the next section.

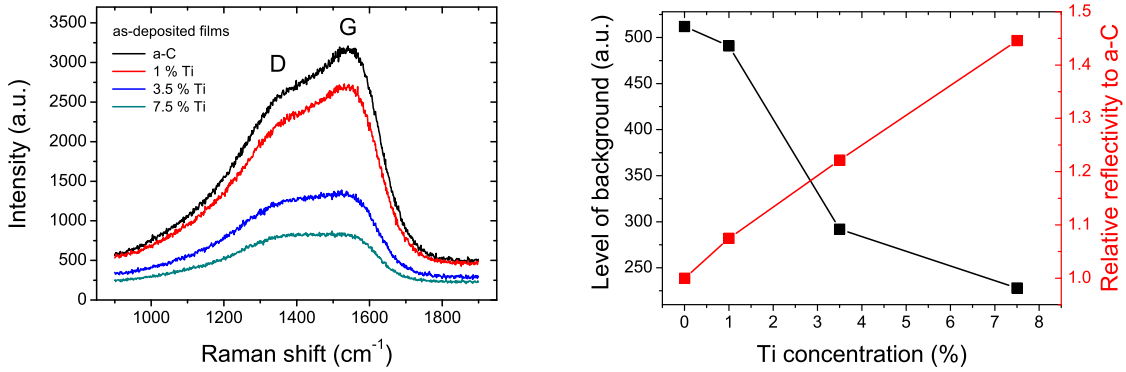

a) b)

Figure 5.24: *a) Raman spectra of a-C and a-C:Ti films after deposition. Two or three spectra, recorded on different sample positions, were averaged. b) Background intensity at 1900 cm^{-1} and reflectivity at 515 nm as function of Ti content.*

5.3.2.2 Different fitting approaches

As described in section 2.2.3, peak fitting is essential to derive quantitative information from a Raman spectrum: the intensity ratio of D and G peak at the peak maximum, I(D)/I(G), and the G peak position, G_{max}. The evolution of both parameters is correlated with changes in the carbon structure, as described by a model published in 2000 by Ferrari and Robertson (FR-model) [54].

The XRD results give no hint that a change of the carbon structure in a-C occurs from amorphous carbon into nanocrystalline graphite during annealing. Therefore, we assume that the carbon structure in the annealed a-C films is always described by stage 2 of the FR-model and annealing increases order and clustering of sp^2 sites in aromatic rings. In this case, a continuously increasing I(D)/I(G) ratio should be observed for increasing annealing temperature.

As described in section 2.2.3, various possibilities exist for fitting Raman spectra. In order to check the influence of different fitting approaches on the developing of I(D)/I(G), three sets of fitting functions have been tested with an annealing series for pure a-C:

1. A linear function for the background combined with two Gaussians for D and G peak
2. As 1. but with two additional Gauss peaks to improve fit quality
3. A linear function, a Breit-Wigner-Fano (BWF) function for the G peak and a Lorentzian for D peak, as applied by Ferrari and Robertson (see section 2.2.3).

During all fits, no constraints were used, i.e. all peak parameters were free variables. The fits for spectra of as-deposited and 1300 K annealed samples are shown in Fig. 5.25, all I(D)/I(G) values are summarized in Tab. 5.3.

The fit with two Gaussians showed poor fit quality, especially in the range of the maxima, leading to an unsatisfactory description of the intensity of D and G peak. I(D)/I(G) increases with increasing annealing temperature until 900 K and decreases then for higher temperatures.

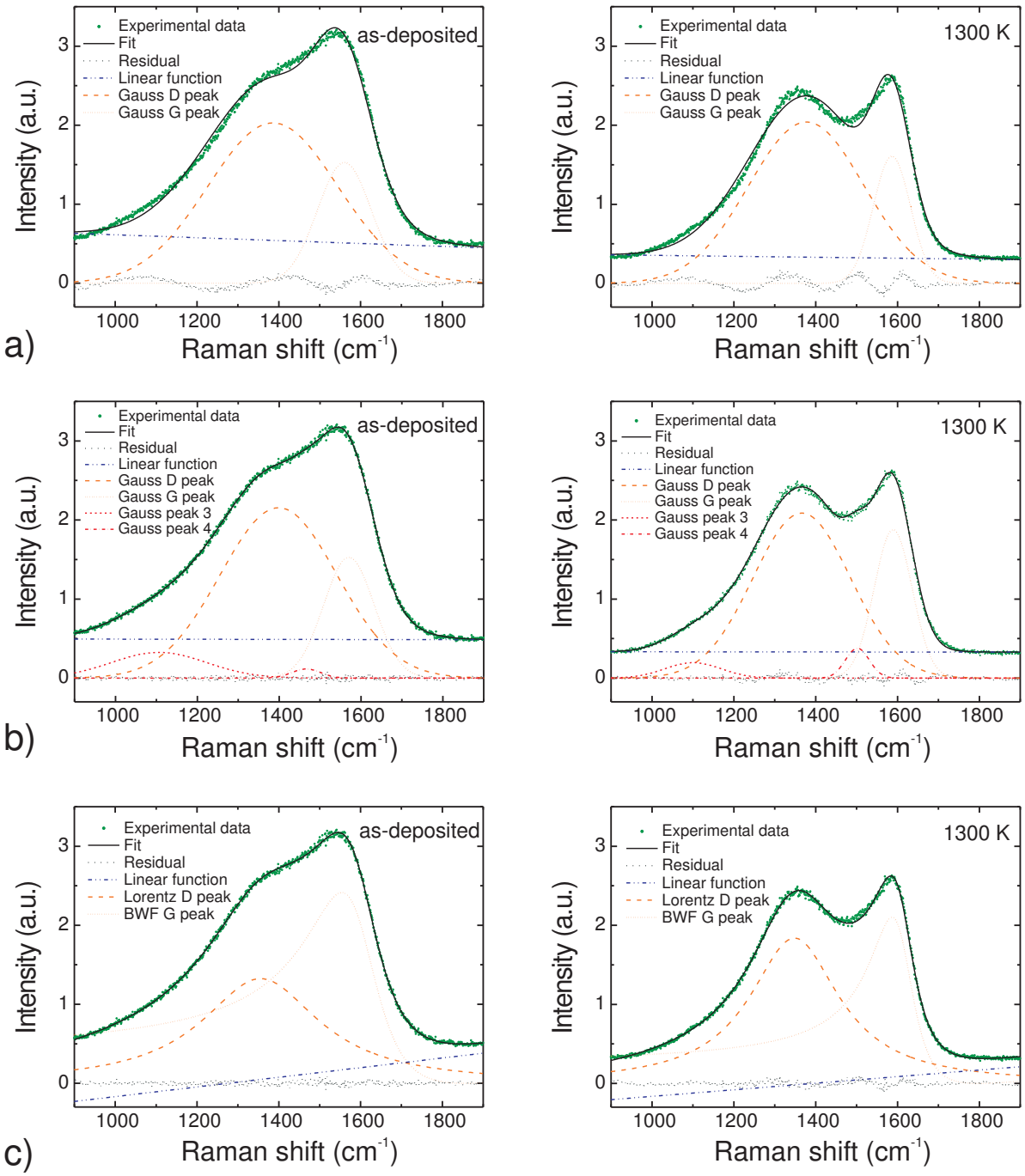

Figure 5.25: *Raman spectra of as-deposited and 1300 K annealed a-C, fitted with a linear function and a) two Gauss peaks, b) four Gauss peaks and c) BWF and Lorentz peaks.*

Table 5.3: *I(D)/I(G) values for an annealing series of a-C, derived by applying different fitting procedures as shown in Fig. 5.25. The ratios are calculated for the peak intensity at the maximum. For Gauss fits, values based on peak areas are given in brackets.*

	I(D)/I(G)		
Annealing temperature (K)	2 Gauss	4 Gauss	BWF+Lorentz
as-deposited	1.33 (3.20)	1.41 (3.26)	0.64
700	1.37 (3.80)	1.33 (3.47)	0.78
900	1.38 (4.11)	1.31 (3.74)	0.90
1100	1.37 (4.10)	1.25 (3.52)	0.95
1300	1.27 (3.93)	1.11 (2.86)	0.98

This is also the case if the I(D)/I(G) is calculated using the peak areas (see values given in brackets in Tab. 5.3).

Two additional Gauss peaks around 1080-1100 cm^{-1} and 1470-1500 cm^{-1} were introduced for the fit with 4 Gaussians. As it is obvious from Fig. 5.25b, the description of the spectral shape is sound, but the relative D peak increase is not reflected in the I(D)/I(G) ratio: Calculation based on peak intensities lead to decreasing I(D)/I(G) with annealing temperature. This is mainly caused by a strong reduction of the D peak FWHM, which requires an increase in intensity of the G peak. Calculating I(D)/I(G) using the areas of the Gaussians leads to a maximum at 900 K.

As outlined above, a continously increasing I(D)/I(G) with ordering is a basic requirement for the FR model. This is not the case for fitting methods based on Gaussians, which were therefore not used for the evaluation of Raman spectra of a-C:Me films.

Fig. 5.25c shows the fitting using BWF, Lorentzian and linear function. An increasing I(D)/I(G) ratio with temperature is derived, which is in line with the assumed increasing aromatic cluster size. In the next section the influence of dopant concentration and annealing temperature is described in detail for a-C and a-C:V films.

5.3.2.3 Variation of I(D)/I(G) and G_{max} for a-C and a-C:V

Fig. 5.26 summarizes data for I(D)/I(G) and G_{max} obtained by peak fitting (Linear, BWF and Lorentz functions) for undoped a-C (i.e, 0 %) and a-C:V. An estimation of the aromatic cluster size according to equation 2.3 is given on the right y-axis.

Annealing of a-C:V alters I(D)/I(G) in a different way as for a-C, where I(D)/I(G) continuously increases. For 1.5 % a-C:V, annealing increases I(D)/I(G) only up to 900 K. For films containing ≥8.5 % V, annealing has the opposite effect compared to a-C: I(D)/I(G) drop from 1.09 to 0.97. As it is obvious from Fig. 5.26a, films annealed to 1300 K have nearly the same I(D)/I(G), almost independent of dopant concentration.

Considering the samples after deposition, V-doping leads to an increase of I(D)/I(G) up to 1.09 for 8.5 % V. The lower value for the highest V concentration (19 %) implies a limit concentration beyond further doping decreases I(D)/I(G).

In Fig. 5.26b the evolution of G_{max} is shown for the same data-set. For pure a-C, annealing leads to an increase in G_{max} from about 1554 cm^{-1}(after deposition) to 1587 cm^{-1}(1300 K), which indicates stronger C=C bonding due to less bonding distortion as expected from the FR-model. This increase with annealing temperature is also seen for all V-doped samples. For

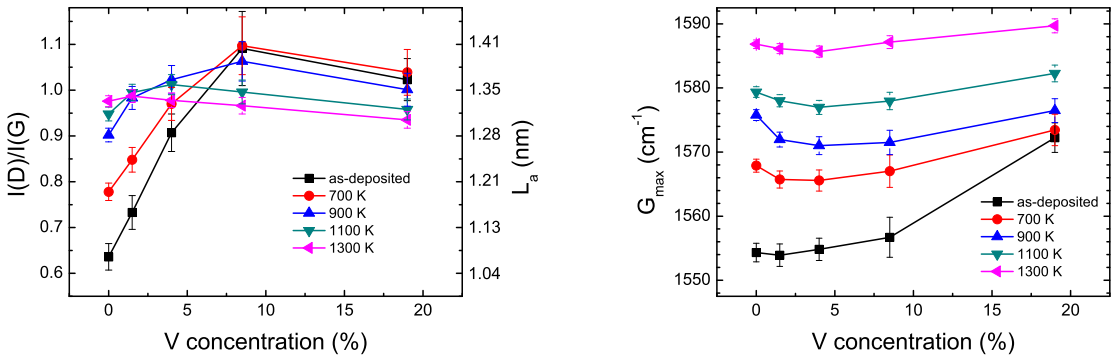

a) b)

Figure 5.26: *a) I(D)/I(G) and b) G_{max} position for a-C and a-C:V samples after deposition and annealed at different temperatures.*

the as-deposited samples, increasing the V content leads to an increase of G_{max}, with a drastic rise from 8.5 to 19 % V. Comparing annealed samples with different concentrations, a slightly different development is observed: They show a lowering of G_{max} at low V concentrations compared to pure a-C; for 3.5 % V a minium value is reached. Higher V concentrations increase the G_{max} position.

The analysis of I(D)/I(G) and G_{max} data of a-C and a-C:V can be summarized as follows:

1. For undoped a-C, annealing leads always to an increase of I(D)/I(G), i.e. to an increase in aromatic cluster size.

2. V-doping drastically increases I(D)/I(G) for the as-deposited samples. Aromatic clustering during deposition is even more enhanced by doping than by annealing of undoped a-C. Around 8.5 % a maximum value is achieved, further increase of V concentration leads to a lower cluster size.

3. The positive effect of annealing to aromatic clustering is more and more suppressed with increasing V concentration. For ≥8.5 % V, annealing leads to decreasing I(D)/I(G). Samples annealed at 1300 K have similar aromatic cluster sizes – independent of the amount of V. This is an indication that these a-C:V films can be considered as a nanocomposite of a-C and VC.

4. Annealing increases G_{max} for all samples, indicating lower bonding distortion and shorter C=C bonding distance. Doping leads to decreasing of G_{max} for low V concentrations; for higher concentrations an increasing of G_{max} is observed.

5.3.2.4 I(D)/I(G) and G_{max} for different dopants

Fig. 5.27a summarizes I(D)/I(G) (and corresponding L_a) values for a-C and a-C:Me for all metal dopants and annealing temperatures. The data for the layers after deposition shows the strongest influence of the metal type. Up to ≈4 % metal concentration I(D)/I(G) increases from 0.6 to ≈0.9 for Ti, V and Zr. At higher metal concentrations doping with Ti and Zr increases I(D)/I(G) stronger than V and W, up to ≈1.6 for 14.5 % Zr. As an exception, doping

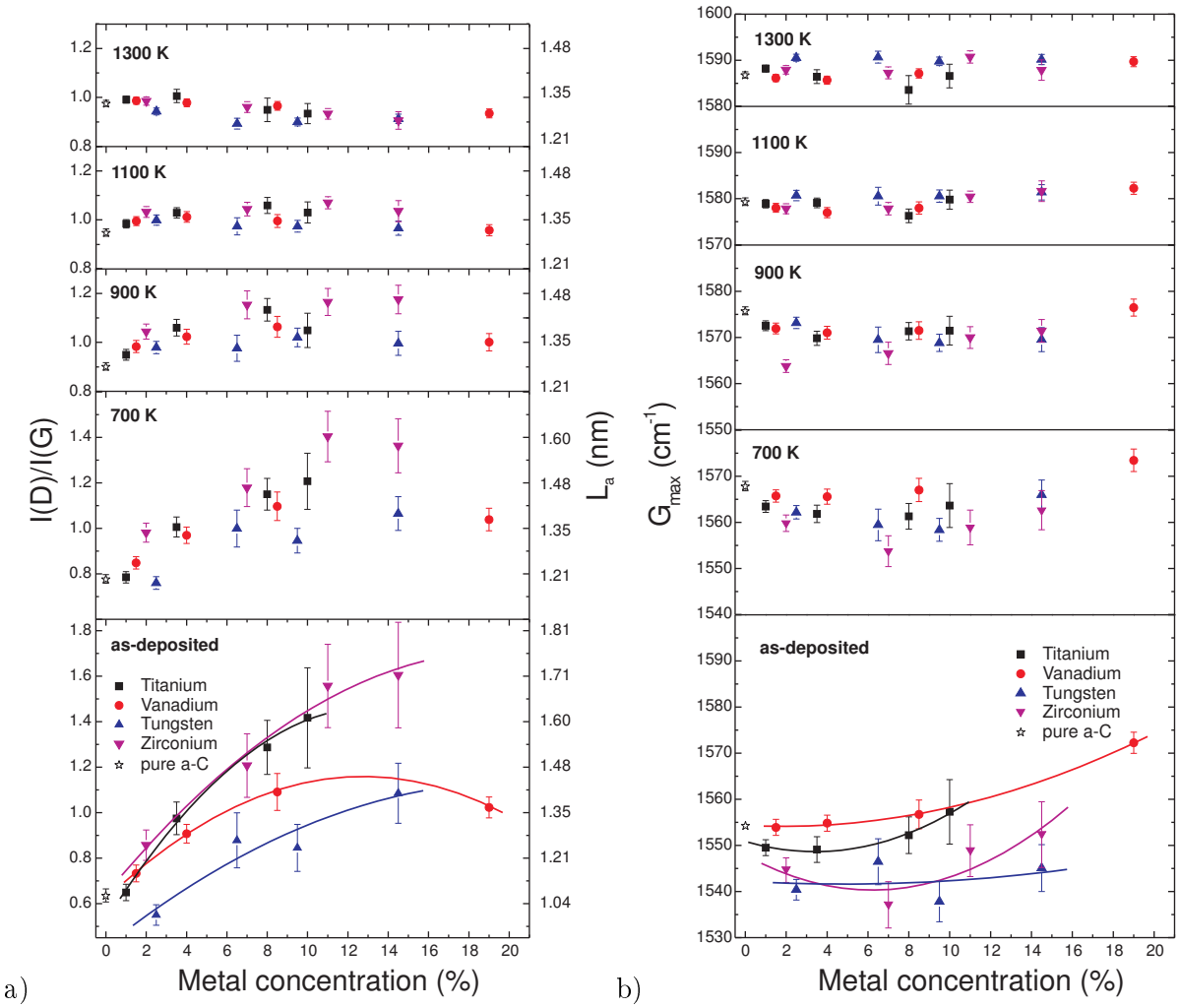

Figure 5.27: *Fit results for all investigated samples annealed up to 1300 K. a) I(D)/I(G) and L_a, b) G_{max}. For both graphs, the y-scaling is kept constant to the as-deposited data set. The error bars indicate the uncertainty introduced by the fitting procedure. For as-deposited data the lines are to guide the eye.*

with 2.5 % W results in a decrease of I(D)/I(G) compared to pure a-C. The similar behavior of Zr and Ti and the difference of Ti and V indicates that the effect of the different dopants on I(D)/I(G) is not related to the atomic mass.

With increasing annealing temperature the differences in I(D)/I(G) vanishes. I(D)/I(G) of the doped layers converge gradually to the value of pure a-C. At 1300 K they lie all between 0.9 and 1.0, the data for a-C:W at the lower end.

The corresponding G_{max} positions are shown in Fig. 5.27b. Considering the data after deposition, doping leads first to a decrease of G_{max} compared to pure a-C for low metal concentrations. With higher concentrations it increases to values even higher than pure a-C. For a-C:V this G_{max} minimum is negligible (1.5 %), a bit more distinct for Ti at 3.5 %. Zr and W shows a more pronounced decrease of G_{max}. For Zr a minimum around 9.5 % occurs, whereas the values scatter more for W.

The data can be roughly classified in 2 groups: a) the light-weight elements V and Ti with low reduction of G_{max} and b) the heavy-mass elements W and Zr, which stronger affects G_{max}. This suggests a correlation of G_{max} with the atomic mass of the dopant metal.

As depicted for the I(D)/I(G) data, also the differences in G_{max} position are reduced with increasing annealing temperature. For 1300 K, all values are similar as for a-C around 1585-1590 cm^{-1}.

5.3.2.5 Discussion of the influence on I(D)/I(G)

As it is obvious from the as-deposited data in Fig. 5.27a, the addition of metals during film growth of amorphous carbon influences I(D)/I(G) and therefore the size of aromatic clusters (L_a). This effect is dependent on the type of metal. Ti and Zr promote clustering of sp^2 hybridized carbon in aromatic rings stronger than V, and W has the smallest effect. Low W concentrations even decrease the cluster size compared to a-C. Therefore, the following order of the metals in promoting aromatic clustering during deposition can be made: W < V < Ti ≈Zr.

In annealing experiments of a-C:Me films with high metal content and carbon-metal sandwich layers a catalytic effect of the metals is observed, which transforms amorphous carbon into "graphite-like" carbon [156–159]. The ability of the metals to act as catalyst is often explained by the formation of a metastable carbide which decomposes into a stable carbide and graphite. For some experiments also the metal itself should be responsible. The importance of metals acting as catalysts in the synthesis of carbon nanotubes [160–162] and other graphitic materials [163–165] is well known even if there is still discussion about the mechanisms.

Garcia-Rosales et al. [24] investigated the catalytic effect of four carbides (TiC, VC, ZrC, WC) for the production of carbide-doped graphites with high thermal conductivity. The carbides were added as µm-sized particles and improved the thermo-mechanical properties after graphitization (> 2900 K) in respect to the undoped graphite. XRD measurements of the graphitic crystallite height L_c was used as a measure for the catalytic graphitization strength. The following order of increasing catalytic activity was found: WC < VC < TiC < ZrC. The reason for the different graphitization strength is not clear.

The qualitative correspondence in graphitization strength of the metal carbides found by Garcia-Rosales et al. and the ability of the metals to promote aromatic clustering during a-C:Me film growth is obvious. This similarity could be attributed to the fact that a basic requirement of the catalytic effect is a certain mobility of the metal or the metal carbide during the ordering process. During graphitization of carbide-doped graphites this mobility

is facilitated by the high temperature which is above the eutectic temperature. This makes it likely that a liquid phase plays a key role, similar to the solid-liquid-solid mechanism proposed for the growth of carbon nanotubes [161].

The production of a-C:Me films by magnetron sputtering is a process far away from the thermodynamic equilibrium. The atoms building up the film have a certain mobility to move on the surface until they reach their final position. Even if the deposition is near room temperature, the average energy of the impacting atoms is around half of their bonding energy in the sputtered material, i.e. a few eV (corresponding to several 10000 K). Reflected Ar ions from the metal sputter target also contribute significantly to the energy deposited during deposition which also increases the atom mobility. Therefore, high metal atom mobility should exist, with possible influence on the carbon structure. The observation of a similar ordering effect of the metals on carbon structure during a-C:Me film growth and catalytic graphitization of graphites seems reasonable – even if no explanation of the underlying process can be given. The similar influence of Ti and Zr indicates a chemical origin, both belong to group 4 of the periodic table of elements.

The lowest ordering effect of tungsten in a-C:W could be explained by the rapid formation of very small, distorted carbide crystallites already during deposition, as discussed in section 5.2.2 and 5.2.3.4. This strong W-C interaction could lead to a decreased mobility of W through the carbon matrix during film growth. Therefore, the catalytic effect is reduced. The formation of carbide crystallites already during deposition is also found for the 19 % V-doped sample (see section 5.2.3.5). This explains the decrease of aromatic cluster size compared to 8.5 % a-C:V (Fig. 5.27a).

Annealing of a-C:Me films after deposition reduces the differences in I(D)/I(G). This can be explained by successive formation and growth of carbide crystallites due to annealing. Carbide crystallite growth requires diffusion of metal through the a-C phase which destroys the initial carbon structure. The mobility of the metal atoms during this process is much smaller than during layer formation by sputtering, and only provided by temperature. Ordering of the a-C phase is therefore more and more determined by the annealing temperature. After annealing to $\geq$1100 K the layer structure is a composite of nm-sized carbide crystallites in an a-C phase.

5.3.2.6 Discussion of the influence on G_{max}

The influence of metal-doping on G_{max} for samples after deposition (Fig. 5.27b) is similar for the light elements Ti/V and the heavy elements W/Zr. This could be explained if we bring to mind that the relative motion of connected sp^2 sites is responsible for the G peak. If metal atoms are located near sp^2 sites they could slow down the relative sp^2 movement due to their inertia. This effect should be stronger for the more heavy elements W and Zr. For a-C:Zr a minimum value is achieved at around 8 %; further increase leads to higher G_{max} position. This could be due to the fact that for higher concentrations very small carbide-like clusters start to form which reduces the amount of metal linked to sp^2 bonded carbon. Since it might be possible that in a-C:W distorted carbide crystallites are present already after deposition and at low concentrations (section 5.2.2), the only weak increase in G_{max} with concentration seems reasonable.

With increasing annealing temperature the differences in G_{max} diminish – similar to the I(D)/I(G) data. This is in line with the gradual formation and growth of carbide crystallites, where most of the metal is present inside the crystallites, and hence not able to influence C=C vibrations.

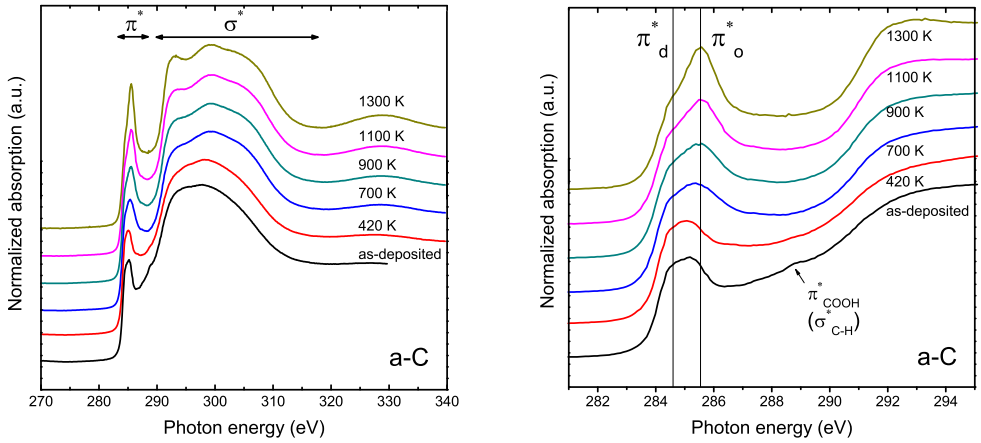

Figure 5.28: *Carbon K-edge NEXAFS spectra of an annealing series of a-C. On the right side the area between 281 and 295 eV is shown in magnification. Spectra are normalized to 320 eV.*

5.3.3 Carbon NEXAFS and XPS experiments

In this section, results of carbon *K*-edge NEXAFS and XPS investigations are presented, which were performed during a measurement campaign at the Synchrotron Radiation Source Daresbury, UK. Both techniques are not sensitive on medium or long-range order (as Raman or XRD), but to the local electronic structure. The strength of NEXAFS is to separate between sp^2 and sp^3 bonded carbon which makes it possible to estimate the sp^2 content. XPS was mainly applied for a rough quantification of the composition (derived from survey spectra) and used to follow changes in the C 1s peak shape. In contrast to other experiments in this work, annealing was performed in-situ in UHV with subsequent measurement of NEXAFS and XPS spectra. Therefore, metal surface agglomeration and oxidation should be minimized (see section 5.1.1). This is of great importance since both techniques are surface sensitive – in contrast to XAFS, XRD and Raman spectroscopy. The information depth of NEXAFS in carbon materials (using total electron yield detection) is reported to be roughly 5 nm [59]. A similar depth sensitivity is assumed for the survey and Ti photoemission spectra using 600 eV photons. The C 1s signal was acquired at 400 eV photon energy, leading to a more surface sensitive signal (1-2 nm).

5.3.3.1 Carbon NEXAFS and surface composition

Fig. 5.28 shows NEXAFS spectra of undoped a-C annealed up to 1300 K. The first feature of the carbon near edge structure is the π^* resonance at 285 eV, due to the transition of a C 1s electron into the anti-bonding π^* orbital of sp^2 hybridized carbon atoms (C=C). Absorption between ≈290-320 eV covers 1s→σ^* transitions, occurring for σ bonds in both sp^2 and sp^3 hybridized carbon (C=C and C-C bonds). Annealing leads to the formation of a significant fine structure in the σ^* region, which is an indication of increased local order due to clustering of the sp^2 phase in aromatic "graphene-like" regions. The broad peak occurring with increasing intensity at 330 eV is due to a multi-electron transition and is related to developing short range-order beyond the next neighboring carbon atoms [166].

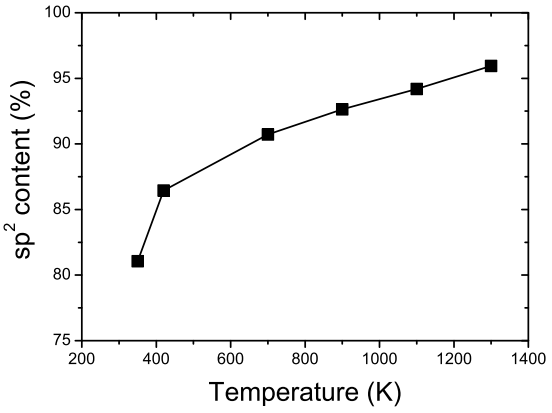

Figure 5.29: *sp^2 content determined from relative π^* intensity of a-C NEXAFS spectra. A spectrum of pure graphite was used as 100 % sp^2 reference.*

The thermally induced changes of the π^* resonance are depicted magnified on the right side of Fig. 5.28. Annealing to 420 K reduced adsorbed or chemisorbed surface contaminations due to film storage in air for several months. Carboxylic carbon species (COOH) have their resonance energies at ≈288.7 eV [167] and decompose at relatively low temperatures (>400 K) [168]. Nevertheless, this reduction is not reflected in the O concentration, determined by XPS, as shown in Tab. 5.4. Non-carbonaceous oxygen contaminations could be the reason but also single-bonded oxygen: hydroxy groups could account to intensity around 295 eV [72]. It should be noted, that the $\sigma^*_{\text{C-H}}$ transition resulting from adsorbed hydrocarbons could also contribute to intensity at around 289 eV [169].

With increasing annealing temperature, the π^* peak becomes more asymmetric, a result of increasing intensity at 285.5 eV. This is attributed to the existence of different π^* states occurring from sp^2 bonded carbon atoms in different local order. It suggests an increasing fraction of sp^2 carbon atoms which are well ordered in respect to their next neighbors. Since the peak maximum of graphite is located at 285.4 eV, this ordered state is labeled as π^*_{o}. A sp^2 carbon bonding state with a more disordered local environment should be responsible for the resonance around 284.7 eV, π^*_{d}.

The sp^2 content was determined by comparison of the relative π^* intensity with graphite (100 % sp^2) as described in section 4.2.3.2. During annealing, it increased from ≈80 % (as-deposited) to ≈95 % (1300 K) as shown in Fig. 5.29.

Recent investigations on the temperature-induced evolution of the C=C π^* feature in a-C films by Diaz et al. [59] and Gago et al. [56] distinguish at least 2 different underlying bonding states and they also found increasing intensity with annealing temperature between 285 and 285.5 eV. They attribute π^* intensity <285 eV to carbon atoms in sp^2 sites with defects [59] or to carbon in chain-like structures or single C=C pairs [56]. Intensity in the π^* resonance between 285 and 285.5 eV is attributed to the promotion of sp^2 carbon atoms in disordered "graphite-like" environments like aromatic rings.

Fig. 5.30 shows the evolving NEXAFS spectra of a 7.5 % doped a-C:Ti film annealed up to 1300 K. Pure TiC has two sharp peaks at about 285.5 eV and 289 eV and a shoulder at 282.5 eV, due to transition of a C 1s electron into Ti-C hybrid orbitals [170]. Therefore, overlapping of

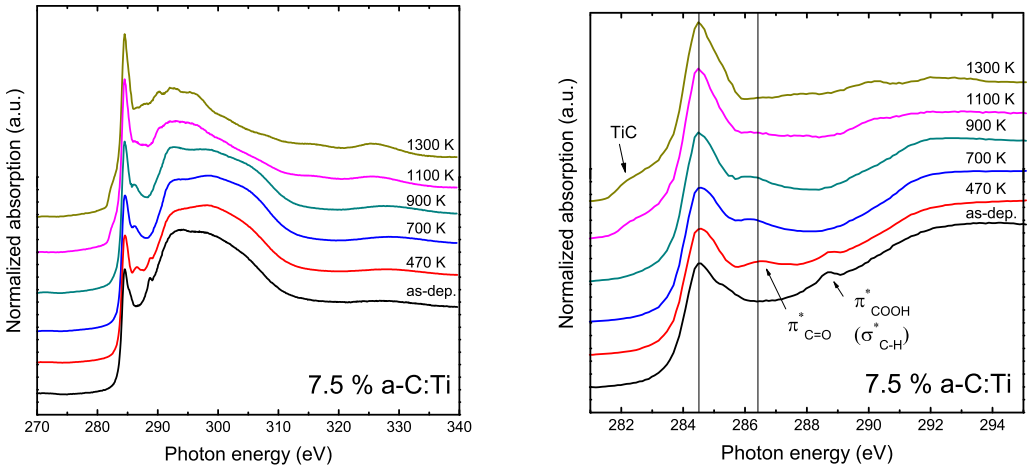

Figure 5.30: *Carbon K-edge NEXAFS spectra of an annealing series of 7.5 % a-C:Ti. On the right side the area between 281 and 295 eV is shown in magnification. Spectra are normalized at 320 eV.*

a-C and TiC resonances at ≈285 eV complicates detailed π^* analysis and sp^2 quantification for a-C:Ti, especially after annealing to 900 K and higher. For these temperatures, XAFS indicates TiC crystallite formation (see section 5.2.3.5). Fig. 5.30 shows a shoulder at 282.5 eV for the spectra taken after annealing to 1100 and 1300 K, which is a clear evidence for carbide formation.

For the as-deposited 7.5 % a-C:Ti sample, the π^* region between 284 and 286 eV shows a maximum at 284.6 with a shoulder at 285.4 eV similar to the spectrum of a-C. The higher intensity at 284.6 could be an indication for more carbon atoms in a disordered π^*_d state. But in contrast to a-C, no increase in intensity at 285.4 eV occurs with annealing. Also the relative intensity of the whole peak is larger, especially for the annealed samples. Calculation of the sp^2 ratio reveals values >100 %, even for the as-deposited sample. This precludes any

Table 5.4: *Sample composition as determined from XPS survey spectra. The difference to 100 % is given by carbon. Due to unknown sensitivity factors for the used setup, values has to be taken as rough estimate. *For a-C, the temperature was 420 K.*

	Atomic concentration (%)						
Temperature (K)	a-C	1 % a-C:Ti		3.5 % a-C:Ti		7.5 % a-C:Ti	
	O	Ti	O	Ti	O	Ti	O
as-dep.	42	n.d.	39	1	34	2	41
470*	42	n.d.	40	2	28	3	38
700	12	n.d.	21	4	19	4	31
900	6	n.d.	9	5	18	8	32
1100	2	n.d.	<2	6	21	12	22
1300	<2	n.d.	<2	6	<2	10	<2

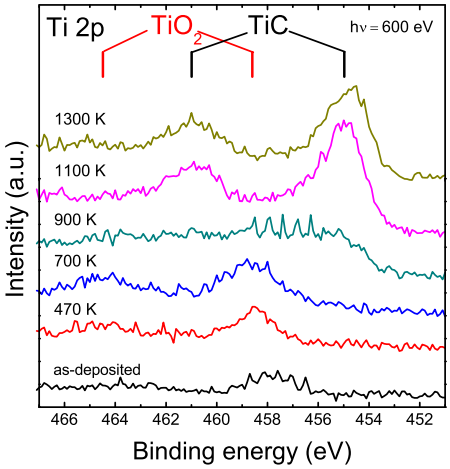

Figure 5.31: *Ti 2p photoemission spectra for the annealing series of the 7.5 % a-C:Ti sample. The positions ($2p_{1/2,3/2}$) for TiO_2 and TiC are indicated. The 900 K spectrum shows distortions resulting from measurement electronics.*

sp^2 quantification similar to a-C in a-C:Ti. This is an indication that Ti-C interactions occur, leading to intensity around 285 eV although no carbide crystallites have formed (see sections 5.2.1 and 5.2.3).

The as-deposited 7.5 % a-C:Ti sample shows a more pronounced peak at ≈288.7 eV (COOH) compared to a-C (Fig. 5.30). Annealing to 470 K reduces this peak slightly, but a new peak occurs at 286.5 eV indicating the formation of C=O bonds, present in carbonyl functionalities [167]. This suggests that physisorbed oxygen containing species (e.g. H_2O, O_2) react with carbon and form stable C=O bonds, probably due to the increased polarity (and therefore reactivity) through Ti-doping. After annealing to 700 K, COOH groups are removed, and the $\pi^*_{C=O}$ resonance is slightly shifted towards lower energy. It is important to note, that the formation of this new peak after annealing to 470 K is not reflected in the respective C 1s spectrum (see below). This is attributed to the higher surface sensitivity of the C 1s measurements, which would mean that the C=O bonds are mainly present in a depth of some nm, and are not probed during the C 1s measurements. On the other hand, it can not be excluded that the origin of this NEXAFS peak at 286.5 eV is related to other effects (e.g. formation of oxy-carbides or an electronic state which is related to a strongly disordered C-Ti bonding).

The high oxygen concentration compared to a-C up to 1100 K is confirmed by XPS, which can not be explained by simple TiO_2 formation. Results of quantified survey spectra for all samples are given in Tab. 5.4. The XPS Ti 2p signal of the 7.5 % a-C:Ti sample, Fig. 5.31, indicates mainly Ti-O bonding up to 700 K. At ≥1100 K, Ti is in carbide environment. The spectrum after annealing to 900 K suffers from an electronic distortion, but probably both Ti-O and Ti-C bonds are present. The increasing Ti concentration between 700 K and 1100 K and the decrease at 1300 K (Tab. 5.4) could be a result of carbide grain growth, associated with Ti diffusion.

After annealing to 1100 K, the C=O functionalities seem also to be reduced (Fig. 5.30) which is in line with the reported decomposition temperature >1000 K [168]. Since RBS did

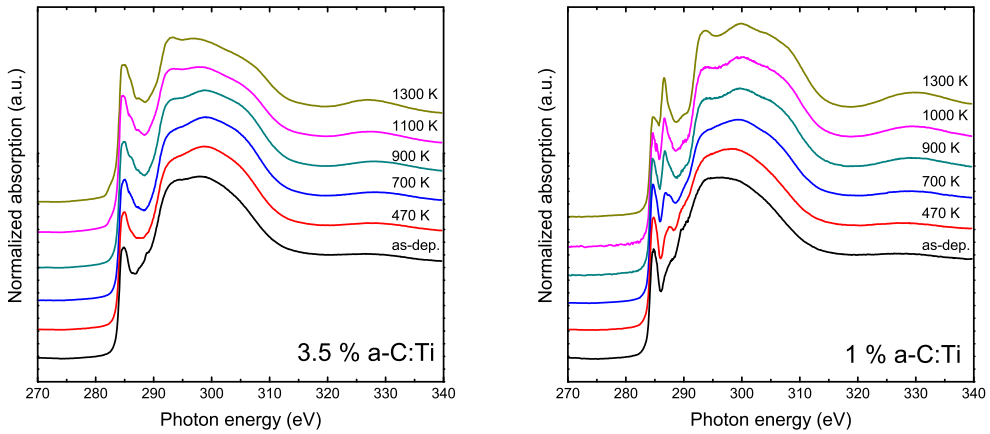

Figure 5.32: *Carbon* K*-edge NEXAFS spectra of an annealing series of 3.5 % and 1 % a-C:Ti.*

not show an increased oxygen content in the bulk of the a-C:Ti film after annealing (section 5.1.1), the high O concentrations are restricted to the surface-near region, which is probed by NEXAFS and XPS.

Fig. 5.32 shows NEXAFS spectra for 3.5 and 1 % a-C:Ti films. In the annealing series for 3.5 % a-C:Ti no distinct peak related related to carbonyl bond formation can be observed, only a slightly increased intensity in that region. At 1100 K, the shoulder at 282.5 eV indicates TiC formation. Generally, the evolution of the spectra lies between a-C and the 7.5 % a-C:Ti sample.

The annealing series for the 1 % a-C:Ti film shows an unexpected behavior: With increasing annealing temperature, a peak between 287 and 288 eV evolves, whose origin is unclear. The σ^* region develops similar to a-C. XPS reveals no other elements, even Ti could not be detected. Further measurements have to be performed to clarify the origin of the described NEXAFS peak.

5.3.3.2 Development of the C 1s photoemission peak

Measurements of the C 1s photoemission region were performed at 400 eV photon energy. For that energy, the grating monochromator provided maximal beam intensity and therefore allowed fast measurements. On the other hand, it resulted in a higher surface sensitivity (≈1-2 nm) compared to NEXAFS. Hence, possible surface-related effects could influence the spectra. For example, Ti surface agglomeration could occur at higher annealing temperatures, or the formation of a thin surface carbide layer instead of small carbide crystallites. The size of the formed TiC crystallites exceed the information depth of the C 1s XPS measurement for the highest annealing temperatures: The average TiC particle size measured for 7.5 % a-C:Ti by XRD is ≈2.5 nm after annealing to 1100 K, and ≈4 nm for 1300 K. But these values have been determined for the bulk of the sample. Keeping all this uncertainties in mind, the following interpretations have to be taken with care.

Fig. 5.33 shows the development of the C 1s region with annealing temperature for a-C and 7.5 % a-C:Ti samples. The spectra are normalized to maximum intensity and on the x-axis

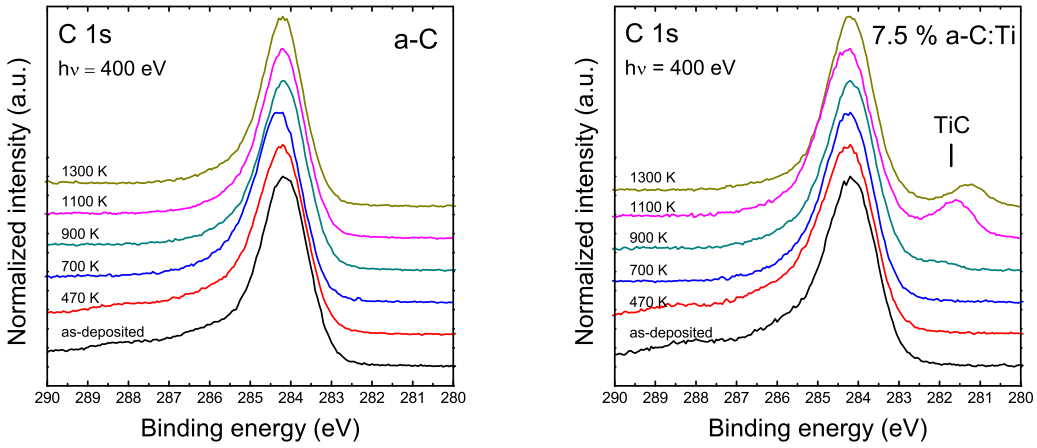

a) b)

Figure 5.33: *C 1s XPS spectra of the annealing series of a) a-C and b) 7.5 % a-C:Ti. All spectra were normalized to maximum intensity and the maximum to a binding energy of 284.2 eV.*

to 284.2 eV, due to slight shifts in the energy scale of the measured spectra. Spectra taken after annealing to 700 K and higher exhibit reduced intensity between 286 and 289 eV, which is correlated with the decomposition of oxygen-containing carbon species [59, 171, 172]. Due to storage in air, the surface is contaminated with such adsorbates. Evolution of a carbidic carbon signal appears for the 7.5 % a-C:Ti sample (Fig. 5.33b) after annealing to 900 K and higher. Ti is probably mainly present as oxide for lower temperatures (Fig. 5.31). The carbidic peak shifts to lower binding energy with increasing annealing temperature: 282.2 eV (900 K), 281.6 eV (1100 K) and 281.3 eV (1300 K).

The peak position of pure TiC is about 281.7 eV [173]. The low intensity at 900 K is due to the fact that Ti is partly oxygen-bonded and not in carbidic state (Fig. 5.31). The higher bonding energy compared to pure TiC could be explained by effects of small cluster sizes [174], or by a distorted Ti-C bonding state: Carbide crystallite formation starts at 900 K, but a fraction of Ti is assumed to be still in amorphous, or strongly distorted TiC arrangement. A not fully developed TiC-like bonding could be responsible for the observed shift in binding energy. Luthin et al. assign a peak around 282.4 eV to originate from other Ti-C phases [175]. For TiC/a-C composites, some authors report about an additional "TiC*" peak around 282.5 eV [42, 98, 176]. Its origin is still unclear, they propose that the existence of an interlayer between TiC particles and a-C is responsible.

After annealing to 1100 K the position and increased intensity of the carbide peak indicates mainly TiC environment for Ti. At 1300 K the relative carbide peak intensity decreased, and a further shift to lower binding energy is observed. Depletion of titanium by diffusion deeper into the layer (due to carbide grain growth) could be the reason, but this is not observed for the 3.5 % Ti-doped sample, where XRD revealed an even larger TiC crystallite size in the bulk (≈6 nm). The origin of the lower binding energy compared to pure TiC (< 281.7 eV) is unclear.

For a more detailed analysis of the non-carbidic carbon signal, peak fitting was applied. The main signal is described by two peaks at 284.2 and 285.1 eV, corresponding to carbon atoms bonded to carbon. In analogy to many publications, they are labeled as P_{sp2} and

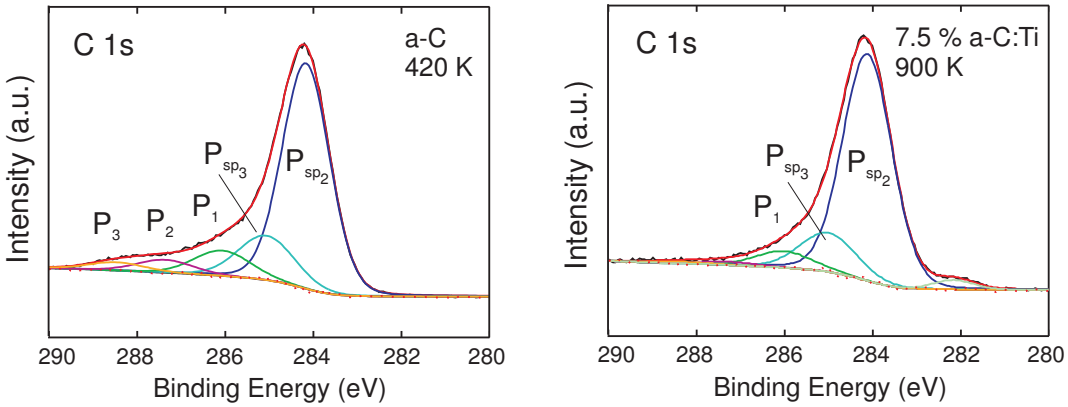

Figure 5.34: *Examples of the spectra fitting for a-C and 7.5 % a-C:Ti. Peak positions of P_{sp3} and P_{1-3} were fixed, also their FWHM (1.5 eV).*

P_{sp3}, according to an assignment originating from different carbon hybridization states. But this classification is most likely oversimplified, and therefore no sp^2 content was calculated. Speranza et al. [143] point out, that the C 1s peak depends on different factors (neighboring atom, hybridization, order, dangling bonds) which precludes simple analysis by two peaks. Linsmeier [177, 178] relates the peak P_{sp3} to disordered sp^2-bonded carbon.

To account for different O-containing species, 3 peaks (P_{1-3}) were introduced at 286.1, 287.4 and 288.5 eV (similar to [59]). The FWHM of P_{1-3} and P_{sp3} were fixed to 1.5 eV. This was done in order to prevent the peaks to become very broad. Fitting with fixed peak width is also in accordance with fitting approaches found in literature (e.g. [143]). Fig. 5.34 exemplarily shows two fits between 280 and 290 eV for a-C and 7.5 % a-C:Ti. P_1 and P_2 (occurring probably from adsorbed oxygen-containing species) do not contribute significantly to the fits of samples annealed to 700 K and higher. Since these impurities could also have influence on the other peaks, only fit results of spectra from samples annealed to $\geq$700 K were considered.

Changes in the carbon structure should be reflected in the ratio P_{sp3}/P_{sp2} and the FWHM of P_{sp2}. Fig. 5.35 shows their development with annealing temperature and Ti content. On the right y-axis the relative area of the carbide peak is given.

Three main observations could be made for P_{sp3}/P_{sp2}:

1. For a-C, annealing leads to a slight linear decrease of the relative P_{sp3} area from 0.25 to 0.2.

2. For T $\geq$900 K, Ti-doping leads to P_{sp3}/P_{sp2} ratios $\leq$0.2.

3. For the 7.5 % a-C:Ti sample annealed to 1100 K, P_{sp3}/P_{sp2} drops to only 0.05, associated with an significant increase of the carbide signal from 3 to 11 %.

This could be interpreted in a way that annealing leads to an increase of sp^2 content in a-C, which is in line with the corresponding NEXAFS results (Fig. 5.29). As annealing to $\geq$900 K leads to carbide formation, the decrease of P_{sp3}/P_{sp2} indicates that preferably sp^3 bonded carbon reacts to TiC. Following the interpretation of Linsmeier, this result suggests that disordered sp^2 bonded carbon reacts to TiC. Such a behavior was also observed by Goldstrass et al. [179] during annealing of a carbon film on beryllium.

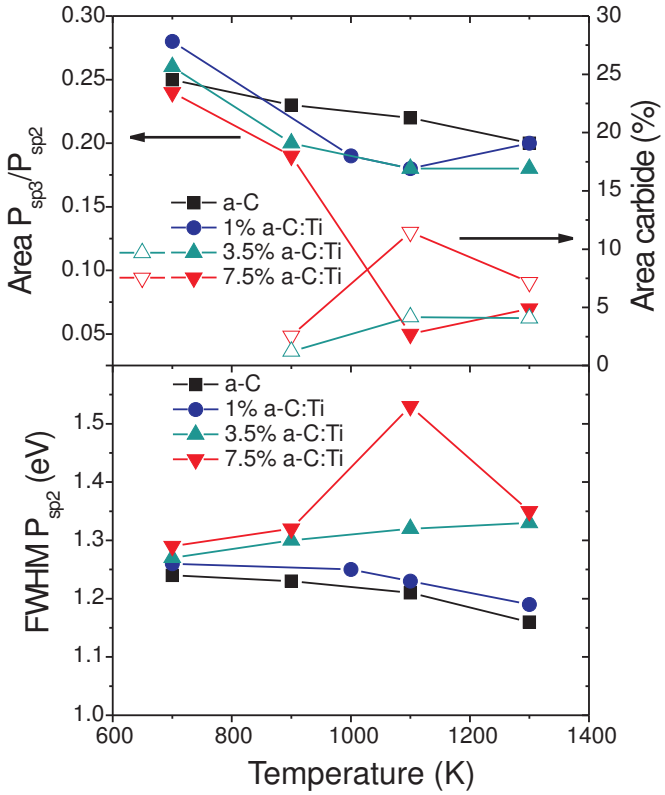

Figure 5.35: *Results of peak fitting for C 1s spectra. Development of P_{sp3}/P_{sp2} (top) and FWHM P_{sp2} (bottom) for a-C and a-C:Ti with annealing temperature. On the top right y-axis the peak area of the carbide peak is given.*

It should be noted that the peak P_1 – introduced to account for O-containing species – contributes to ≈10 % for all spectra of as-deposited and 470 K samples. For higher annealing temperatures it still accounts for 5 % peak area, independent of Ti concentration. Since at least for a-C, O contamination could be excluded after annealing to 1300 K, this indicates that the peak P_1 also contributes to intensity of sp^3 (or disordered sp^2) bonded carbon. Nevertheless, the ratio $(P_1+P_{sp3})/P_{sp2}$ gives the same qualitative development as depicted in Fig. 5.35.

According to Diaz et al. [180], the FWHM of the peak P_{sp2} is related to sp^2 bond disorder. The bottom graph in Fig. 5.35 shows the P_{sp2} FWHM as a function of annealing temperature and Ti concentration. For a-C, annealing leads to a slight decrease from 1.25 (700 K) to 1.15 (1300 K). The FWHM of 1 % a-C:Ti is only slightly increased compared to a-C. Doping with 3.5 and 7.5 % Ti increases the FWHM significantly. Whereas for 3.5 % a-C:Ti a linear increase is observed, for 7.5 % a-C:Ti a drastic increase at 1100 K occurs, probably related to the increase of TiC peak area. This results suggest, that thermally induced ordering leads to a decrease of sp^2 bond disorder in the case of a-C and 1 % a-C:Ti. Doping with 3.5 and 7.5 % Ti results in an increase of sp^2 bond disorder with annealing, probably related to diffusion of Ti and the formation and growth of a crystalline carbide phase. These processes counteract the ordering in the carbon phase of a-C:Ti.

It should be kept in mind that all interpretations are deduced from spectra which reflect the surface-near region of the films. This is especially apparent in the role of oxygen contaminations. Also the formation of carbide crystallites with particle sizes larger than the assumed depth sensitivity has to be considered. Therefore, this results can not be easily transferred to explain structural changes in the bulk of the sample. XPS measurements with high photon energies – as possible in the new experiment HIKE at BESSY – could help to close this gap.

5.3.4 Summary

Results of XRD, Raman, NEXAFS and XPS investigations to analyze the carbon matrix are briefly summarized.

Crystallinity

The presence of small, 2-dimensional graphene-like crystalline regions in as-deposited a-C is indicated by a diffraction peak. The number of such regions increases with annealing.

Aromatic clustering

Raman spectrosopy revealed the influence of doping and annealing on the aromatic clustering of the sp^2 phase in a-C:Me. Addition of up to 15 % metal leads to a continuous increase of the average aromatic cluster size in the as-deposited samples, compared to pure a-C. The strongest effect is observed for Ti and Zr. W-doping has the lowest effect. Annealing diminishes the differences of the different dopants regarding the clustering of the sp^2 phase. After heating to ≥1100 K, the aromatic cluster size is the same as for a-C, independent of metal type and content. For that temperature, the a-C:Me film structure can be described as nanocomposite of carbide crystallites embedded in an a-C matrix; the carbon structure is then only determined by the annealing temperature.

Carbon bonding

NEXAFS and XPS experiments gave information about the local carbon structure. For a-C an increase of the of the sp^2 content from about 80 % (as-deposited) to 95 % (1300 K) is estimated, associated with increasing bonding order. No sp^2 quantification is possible for Ti-doped films. NEXAFS spectra of the 7.5 % a-C:Ti sample indicate formation of carbonyl functionalities after annealing to 470 K. XPS indicate that preferably sp^3 bonded carbon reacts to TiC during annealing of a-C:Ti.

Chapter 6

Erosion investigations

In this chapter results of erosion investigations of a-C:Me films are presented. In the first section, the main objective is the comparison of the total erosion yield Y_{IBA} (determined by quantification of the eroded material using ex-situ ion beam analysis) with the CD_4 production yield Y_{CD_4} (determined by in-situ mass spectrometry). This gives information about the relative amount of carbon which reacts to CD_4. The second section is devoted to investigations dealing with the influence of the a-C:Me nanostructure on the erosion yield. Erosion was performed in a deuterium low-pressure plasma. The erosion yield of as-deposited a-C:Me films is compared with the erosion of specimen annealed to 1100 K before the experiment. Thus it is possible to study the influence of the film nanostructure on the erosion yield. In the last section of this chapter results of erosion investigations with doped graphite and CFC materials are presented.

For all erosion investigations it is important to bring to mind the applied D fluence. Different fluence scales have to be considered and the two effects of the doping has to be distinguished: The *chemical influence* on the erosion mechanism (lowering the activation energy for hydrogen release) and *metal enrichment* due to preferential erosion of carbon, leading to a protective surface layer. The fluence to achieve an effective enrichment depends on the protecting carbide particle size. Whereas the chemical influence is always active, the effect of metal enrichment becomes only dominant for higher fluences. Metal enrichment should not influence the temperature-dependent measurements in section 6.1.1 (4-7·10^{21} D m^{-2} for each temperature step) and mainly the chemical influence is measured. For the comparison of the total erosion yield and the CD_4 production yield (section 6.1.2) and during plasma erosion experiments (6.2) fluences of about 5-10·10^{23} D m^{-2} were applied. Here, an significant additional effect of metal enrichment can be assumed. For the highest fluences applied during erosion of doped graphites and CFC (10^{24}-10^{25} D m^{-2}), the effect of protective metal-containing surface layer becomes dominant.

6.1 Deuterium ion beam erosion of a-C:Me

6.1.1 Temperature dependence of the methane production yield

Fig. 6.1 summarizes the temperature dependence of the normalized CD_4 production yield, Y_{CD_4}, with 200 eV D for a-C and a-C:Me films. Y_{CD_4} shows a maximum at 830 K of about 0.08 for a-C. For even low dopant concentrations, Y_{CD_4} decreases strongly – especially at temperatures around the maximum. The maximum in the temperature dependency shifts to lower

temperatures with increasing dopant concentration for all a-C:Me films. This is explained with a reduction of the activation energy for the hydrogen release of the chemical sputtering process at elevated temperatures (see section 3.2). Also the a-C:V concentration series shows the described shift to lower temperatures for higher V concentrations. The following order in shifting the maximum (and lowering Y_{CD_4}) is observed: V < Ti < Zr (W). This order is in agreement with the observed carbide crystallite size. As shown in section 5.2.1, for similar metal concentrations the carbide crystallite size increase in the order Zr < Ti < V. The larger the carbide crystallites the smaller is the expected influence on the chemical sputtering mechanism. Therefore, the ability to lower the activation energy for hydrogen release should be the lowest for V-doping. The stronger influence on Y_{CD_4} with increasing metal concentration is plausible.

On the other hand, Y_{CD_4} is enhanced for the first temperature step (about 320 K). This is most pronounced for Ti, lower for V and hardly visible for Zr and W-doping. A strong enhancement of Y_{CD_4} for a-C:Me films at temperatures $\leq$500 K was observed for similar experiments at 30 eV D [39, 125]. In that investigations also a shift of the maximum was observed; for a-C:W and higher metal concentrations of a-C:V and a-C:Ti the maximum vanished completely. No mechanistic explanation was given for the increased CD_4 production at lower temperatures during 30 eV D erosion.

For some specimens, the effect of dopant enrichment at the surface due to preferential erosion of the carbon during 200 eV D bombardment was checked by determining the methane signal at room temperature once more after measuring the temperature dependence and cooling down. No significant increase was observed, hence, metal enrichment has only a small effect for fluences below $10^{23}\,\mathrm{D\,m^{-2}}$.

In principle, the increase of CD_4 production at room temperature can be explained either by an increased erosion or by a shift of the erosion species to CD_4 at the expense of higher hydrocarbons C_xH_y. For that purpose, measurements of the total erosion yield were performed at fixed temperatures and compared with the respective CD_4 production yield as described in the next section.

6.1.2 Comparison of total and methane production yield

Fig. 6.2 shows the total and CD_4 production yield of a-C and a-C:W films for four erosion conditions: 30 and 200 eV D impact at RT and elevated temperature. The accumulated fluences on the doped films are about $5\text{-}7{\cdot}10^{23}\,\mathrm{D\,m^{-2}}$. Therefore, metal enrichment due to preferential erosion of carbon is observed.

The total erosion yields of pure carbon films are comparable to the published yields from pyrolytic graphite [117]. For 200 and 1000 eV D physical sputtering contributes to the erosion of carbon, as indicated in Fig. 6.2. At 200 eV D, the physical sputtering yield is about 0.015 for C. The estimation of this contribution on the doped films is not possible due to the low total erosion and the effect of metal enrichment due to preferential sputtering of carbon. Also sputtering of the metal (assumed to be present as carbide) occurs: The physical sputtering yield for the metal is about 0.008 for Ti, 0.007 for V, 0.0005 for Zr, and negligible for W [37].

The a-C:W films show a significantly reduced total erosion yield (Fig. 6.2). For 200 eV D, Y_{IBA} is about 3 times smaller for RT and about 9 times smaller for 750 K. At 30 eV D, total erosion is even more reduced: about a factor of 7 for RT. For 620 K, Y_{IBA} is about 15 times smaller.

A different behavior is observed for the CD_4 production yield. As obvious from Fig. 6.2,

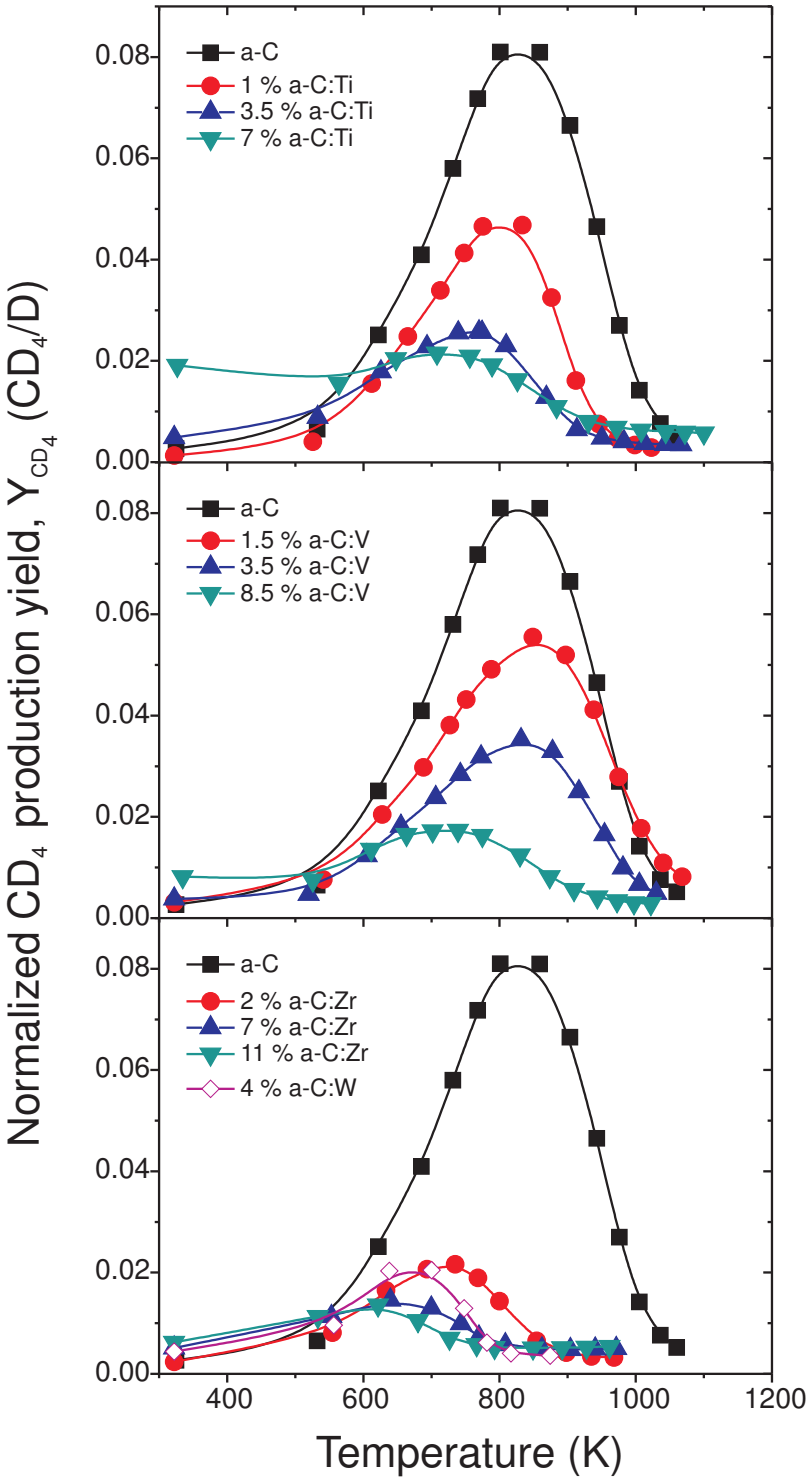

Figure 6.1: *Normalized CD_4 production yield (Y_{CD_4}) for a-C and a-C:Me films as function of temperature under 200 eV D impact. D fluence increases with temperature and is about 4-7·10^{21} D m^{-2} for each temperature step.*

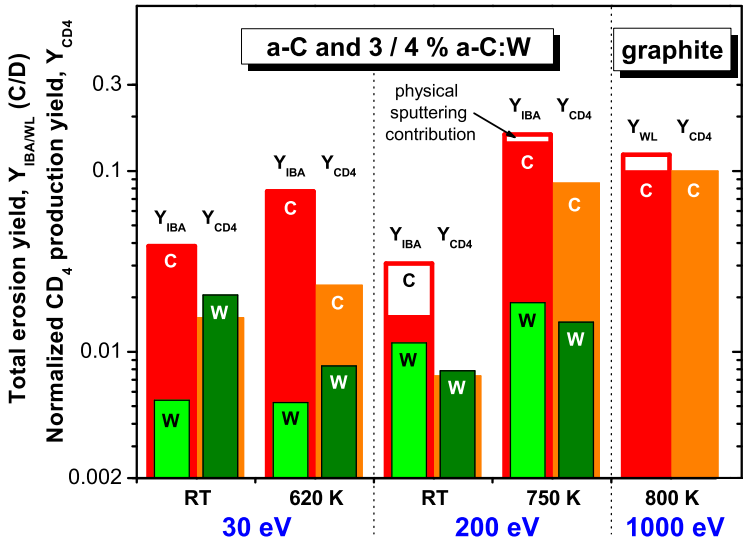

Figure 6.2: *Total erosion yield (Y_{IBA} for a-C and a-C:W, Y_{WL} for graphite) and normalized CD_4 erosion yield (Y_{CD_4}, average for the experiment). W concentration 3 % (30 eV) and 4 % (200 eV).*

Y_{CD_4} is not reduced for RT erosion at both ion energies, but is even slightly increased. A reduction of about a factor 3 (30 eV D) and factor 6 (200 eV D) is observed for elevated temperatures. The different development of Y_{CD_4} and Y_{IBA} indicates a change in erosion species distribution to CD_4.

Y_{CD_4} for 4 % a-C:W at RT and 200 eV is higher than the respective data point in Fig. 6.1, which was measured at a 10 times lower fluence. This can be explained by dopant enrichment at the surface, leading to a higher effective W concentration. It was shown in [39,125] that an increase in W concentration leads to higher Y_{CD_4}. The time evaluation of the CD_4 signal is also in accordance with this observation. A similar behavior for Y_{CD_4} with fluence (leading to increased metal concentration due to enrichment) is observed for the 4 % V and 2 % Zr-doped films. For 4 and 7 % a-C:Ti no increased Y_{CD_4} occurs with enrichment.

Fig. 6.3 summarizes results for all investigated a-C:Me films given as the erosion relative to a-C, i.e. the ratio Y_{dopant}/Y_C for Y_{IBA} and Y_{CD_4}. It is obvious from Fig. 6.3a, that doping always reduces the total erosion significantly compared to a-C, i.e. all values are <1. This effect is stronger at elevated temperature. For W and Ti-doped films, the decrease in erosion is stronger for 30 eV D compared to 200 eV D. Considering the 200 eV D data in Fig. 6.3a, the total erosion is smaller in the case of W/Zr-doping compared to Ti/V for similar concentrations.

The total erosion yields of the metals for bombardment with 200 eV D were obtained from metal loss, measured by IBA. Physical sputtering should be the erosion process, but the metal yields at 750 K are about doubled compared to those at RT erosion. This is unexpected and has to be further studied. The formation of hydrides could be an explanation in the case of Ti and V-doping. It could be speculated that local metal-hydrogen interaction increase the metal mobility especially at higher temperatures. Nevertheless, the metal yields are always

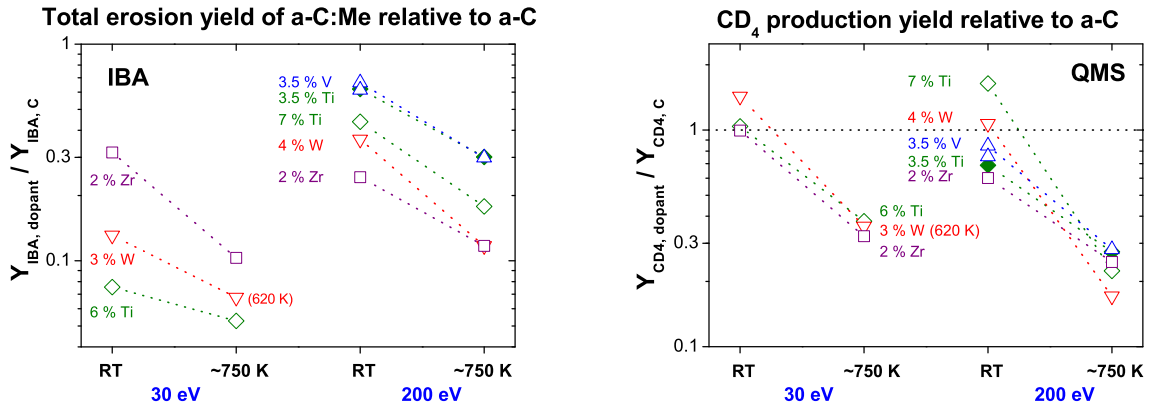

Figure 6.3: *Ratio of erosion yields of a-C:Me to a-C for a) the total erosion yield Y_{IBA} and b) CD_4 production yield Y_{CD_4}. For 3.5 % a-C:V two independent experiments were performed for 200 eV D at RT. A ratio of 1 indicates the erosion yield of pure a-C.*

well below the physical sputtering yield for the pure metals at 200 eV: 0.0018 (7 % Ti), 0.0007 (3.5 % Ti), 0.0009 (3.5 % V), 0.0001 (2 % Zr), <0.0001 (4 % W).

The influence of doping on the CD_4 production is presented in Fig. 6.3b. As already shown for the a-C:W data in Fig. 6.2, also Ti and Zr-doping lead to a increased CD_4 production for 30 eV D erosion at RT. At 200 eV D and RT an almost doubled CD_4 production could be observed for 7 % a-C:Ti (Fig. 6.3b). For erosion at 750 K, a reduced CD_4 production is observed for both ion energies. This is in accordance with the low-fluence data in Fig. 6.1.

To compare the relative development of both erosion yields, the ratio of the normalized CD_4 production yield to the total erosion yield was calculated. This ratio, Y_{CD_4}/Y_{IBA}, is presented in Fig. 6.4 for all investigated films. For pure carbon, Y_{CD_4}/Y_{IBA} is in the range between 0.2 and 0.5, which is consistent with the reported ratio of heavier hydrocarbon to CD_4 measured with QMS (1.5-4 for 30 and 200 eV) and of the total yield to CD_4 (8 for 200 eV) [104, 116, 181].

In principal, the erosion products could be divided in four groups, which are defined by their observability: CD_4, CD_3 radicals, heavier hydrocarbons detectable in the residual gas, and erosion products with high sticking probability at the walls. Y_{CD_4}/Y_{IBA} equal to 1 means that the contribution of CD_4 to the distribution of erosion species is the same as for carbon eroded with 1000 eV D at 800 K. It is reported that the total erosion yield under these conditions is only around 3 times larger than the methane production yield [181] .

For a-C:Me films, Y_{CD_4}/Y_{IBA} is increased up to 5, i.e. by more than a factor of 10 compared to pure C films especially for 30 eV D. The increase means that the distribution of erosion species is shifted from heavier hydrocarbons and radicals to more CD_4 production by doping. The observed factor of 10 is too large to be explained by shifting only the heavier hydrocarbons into the CD_4 signal (max. a factor of 4 should be observed by QMS measurements as mentioned above). Also the reported erosion products with high sticking probability and methyl radicals have to be transferred to the reaction channel of CD_4 production [117]. Another indication for a change in the product distribution can be gained from mass 18 observed by QMS, which can be used as an indicator for CD_3 radicals and heavier hydrocarbons [139]. For doped

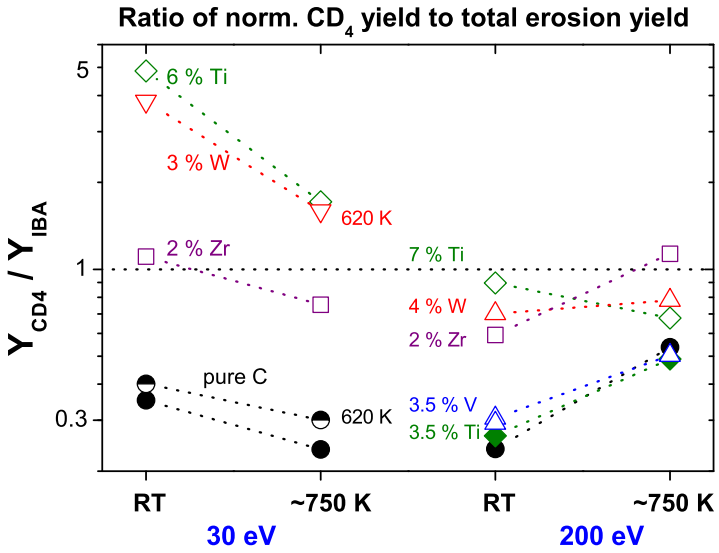

Figure 6.4: *Ratio of normalized CD_4 production yield to total erosion yield, Y_{CD_4}/Y_{IBA}, for all investigated samples.*

films, the ratio of mass 18 to mass 20 is increasing significantly compared to pure carbon at temperatures >600 K (30 eV D) and >750 K (200 eV D). It should be noted, that this ratio seems to be very sensitive on experimental conditions (especially at RT) and its reproducibility is not very good. Nevertheless, the general trend is obvious.

The comparison of both erosion yields demonstrates, that using only the CD_4 production yield as indicator for chemical sputtering leads to wrong conclusions. As an example, Y_{CD_4} at 30 eV D is increased by about 40 % for 3 % a-C:W compared to a-C. But the total erosion yield is reduced by a factor of 7. This clearly shows that doping significantly changes the distribution of erosion products.

6.1.3 Investigation of erosion morphology

The surface morphology of Ti, V and W-doped samples with similar concentration was investigated by AFM before and after erosion of 200 eV D as shown in Fig. 6.5 and Fig. 6.6. Much effort was spent to ensure that the presented graphs are representative for morphology in the erosion spot. Therefore, at least 3 different positions were measured, which gave qualitatively similar results. The applied D^+ fluence was about $5\text{-}9{\cdot}10^{23}$ D m^{-2} for all presented films, except a-C for erosion at 750 K (only $2{\cdot}10^{23}$ D m^{-2} due to high erosion yield).

Whereas the surface morphology and roughness is comparable for all as-deposited samples (R_q between 3 and 4 nm), it varies strongly for the eroded samples. Erosion at RT leads to an extremely smooth surface for a-C; after erosion at 750 K the surface morphology appears similar as before erosion, with a slightly decreased roughness. Except for a-C:W, this is a general trend: roughness R_q is lower for erosion at RT compared to erosion at 750 K. This might be related with the amount of removed carbon which is about twice larger for erosion at 750 K for a-C, Ti- and V-doped films (due to the different erosion yields). It is given in the

captions of Figs. 6.5 and 6.6.

More fascinating than comparing R_q is the observation, that the appearance of the surface depends on erosion conditions and dopants. Comparing the morphologies for the same erosion conditions but different films, large variations are obvious. After erosion at RT, finer structures can be observed on the surface for a-C, a-C:Ti and a-C:V. Very surprising is the appearance of the a-C:W film eroded at RT. The surface is not characterized by small grains, but shows a canyon-like structure with depths of up to 80 nm. For a-C:W, finer surface structures are observed after erosion at 750 K.

Many factors influence the observed morphology, and erosion is due to chemical and physical processes. Any attempt for an explanation of the different morphology has to be very complex – especially for a heterogeneous material as a-C:Me films. This was beyond the scope of this work.

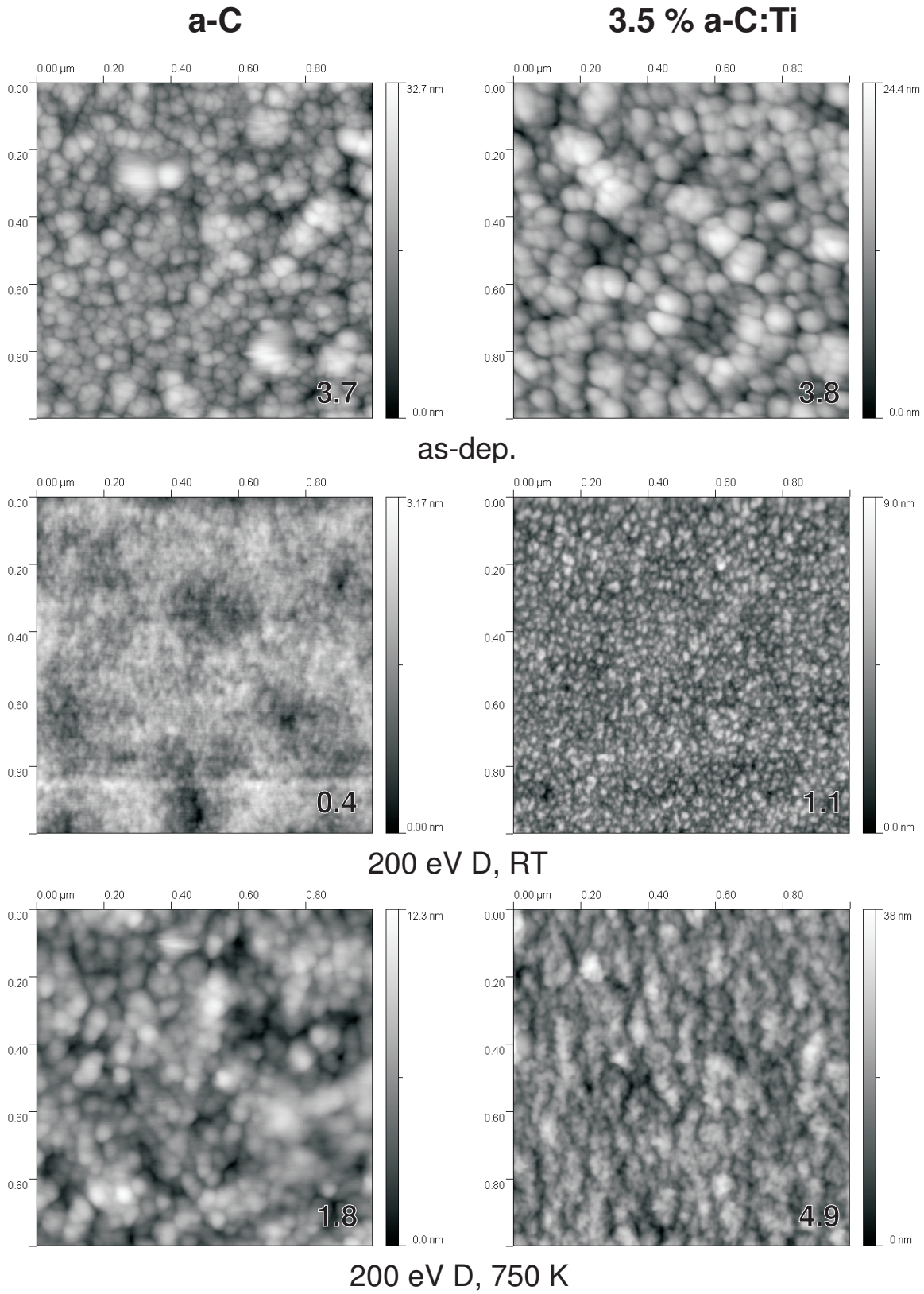

Figure 6.5: *Surface morphology of a-C and 3.5 % a-C:Ti films before and after erosion with 200 eV D measured by contact-AFM. Surface roughness R_q (in nm) is given as inset. Removed carbon amount (in 10^{18} cm^{-2}, RT/750 K): a-C 1.9/3.8; a-C:Ti 1.7/4.3.*

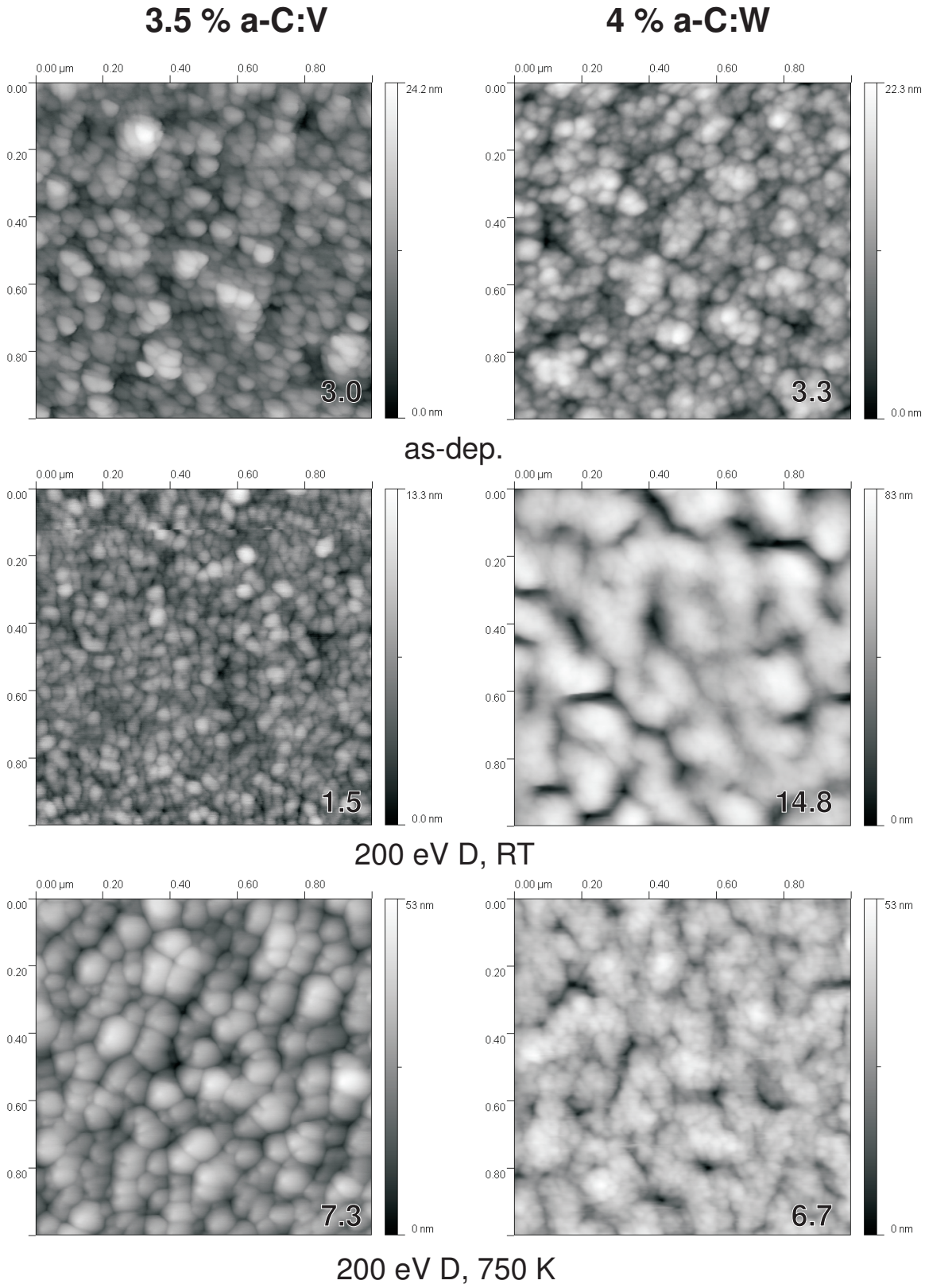

Figure 6.6: *Surface morphology of 3.5 % a-C:V and 4 % a-C:W films before and after erosion with 200 eV D measured by contact-AFM. Surface roughness R_q (in nm) is given as inset. Removed carbon amount (in 10^{18} cm^{-2}, RT/750 K): a-C:V 1.4/3.7; a-C:W 0.7/0.9.*

6.2 Deuterium plasma erosion of a-C:Me

The plasma erosion behavior of a-C:Me films was studied at the University of Augsburg. The erosion environment is different compared to ion beam experiments: The plasma contains not only 30 eV D_x^+ ions (mainly D^+), but also about 170 times more neutral atomic and molecular deuterium.

The main objective of this measurements was to study the influence of metal distribution on the erosion. Whereas the as-deposited films exhibit an atomically disperse dopant distribution, annealing to 1100 K before the erosion experiment leads to the formation of nm-sized carbide crystallites in the carbon matrix (section 5.2.1). Therefore, for Ti and V-doped films, two sets of samples were prepared and investigated.

Pure a-C films were also eroded. Unfortunately, due to experimental problems and the very fast erosion of a-C, no reliable data was produced during these erosion experiments.

Figs. 6.7a and b summarizes the erosion yields as function of D ion fluence of a-C:Ti and a-C:V samples with and without pre-annealing. For a-C:W, only as-deposited films were eroded, shown in Fig. 6.7c. To compare with a pure carbon material, the erosion yield of fine-grain graphite (0.045, determined in [141]) is indicated as solid line.

All doped films show significant lower erosion yields compared to graphite and the yield is decreasing with metal content and fluence. Annealing leads to higher erosion yields for a-C:V.

6.2.1 Influence of fluence and metal concentration

First of all, only samples without pre-annealing are considered, the others were discussed in the next section. Since the experimental setup has a stabilization phase of several minutes, the data points at fluences below $\approx 2 \cdot 10^{23}$ m^{-2} have to be taken with care. With increasing metal concentration, the total fluence applied for a sample decreased. This is due to the lower erosion yield and therefore, the detection limit of the spectroscopy was achieved faster. The decreasing erosion yield with fluence is due to metal enrichment at the surface – a result of preferential erosion of carbon. This was confirmed by surface sensitive RBS measurements with 500 keV He^+. Fig. 6.8 shows a RBS spectrum of the eroded 3.5 % a-C:Ti sample. Simulation of the spectrum to quantify the metal conent revealed an enrichment zone of ≈30 nm. The first 5 nm were fitted with pure TiO_2. This has most likely formed from pure Ti after storage of the film in air. Oxide formation during plasma exposure seems unlikely, because of the large amount of hydrogen which results in a chemically reducing atmosphere. The next 25 nm was fitted by 12 % Ti together with about 24 % O. For other samples the enrichment profile is similar: A several nm thin metal oxide film is followed by a 10-30 nm thick metal oxide enriched carbon layer. The bulk concentration is not altered. XPS investigation of the eroded 1.5 % a-C:V sample showed only V_2O_5 at the surface, no carbide or metal signal was observable. This result justifies fitting of the RBS spectra with a pure metal oxide surface. Generally, the samples with higher metal content exhibit a smaller enrichment zone, which should be due to the lower fluences achieved.

As it is obvious from Fig. 6.7, all layers achieved erosion yields lower than 0.01 at the highest applied fluence, except the films with lowest concentrations. The 6.5 % and 9.5 % a-C:W films have their first data point even below 0.008. These low yields are accompanied by a high uncertainty which could explain the almost similar values for these two samples. For a few data points error bars are given, which represents errors in the ion flux determination and of the spectroscopy.

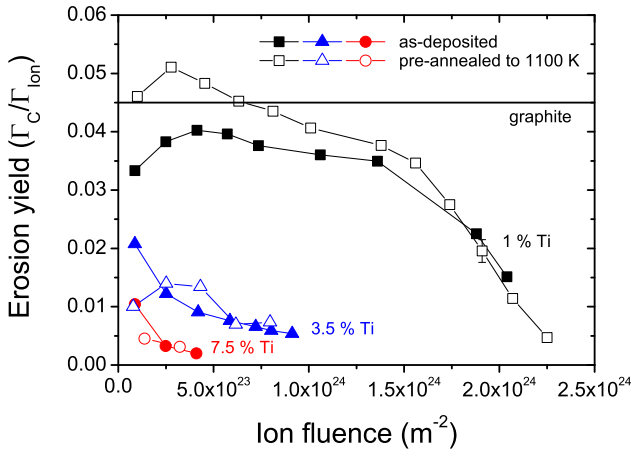

a)

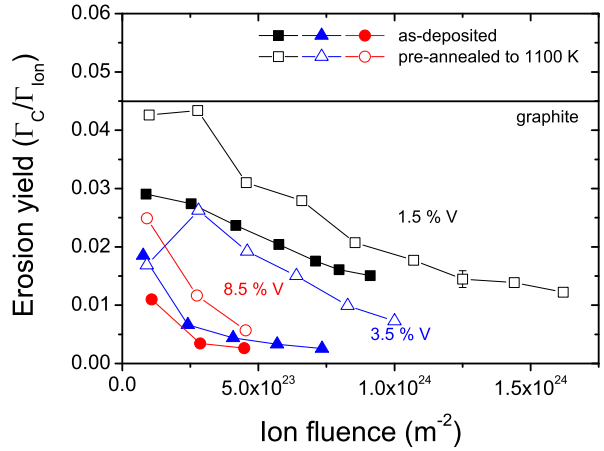

b)

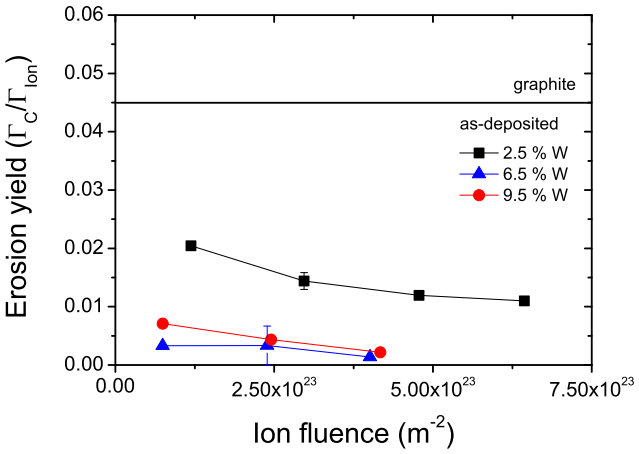

c)

Figure 6.7: *Fluence dependence of the erosion yield during plasma erosion at 350 K of a) a-C:Ti and b) a-C:V films with different dopant concentration and distribution. c) Erosion yield data for as-deposited a-C:W. The solid lines represent the erosion yield of graphite. Filled symbols: films were eroded as-deposited, open symbols: films were annealed to 1100 K before erosion.*

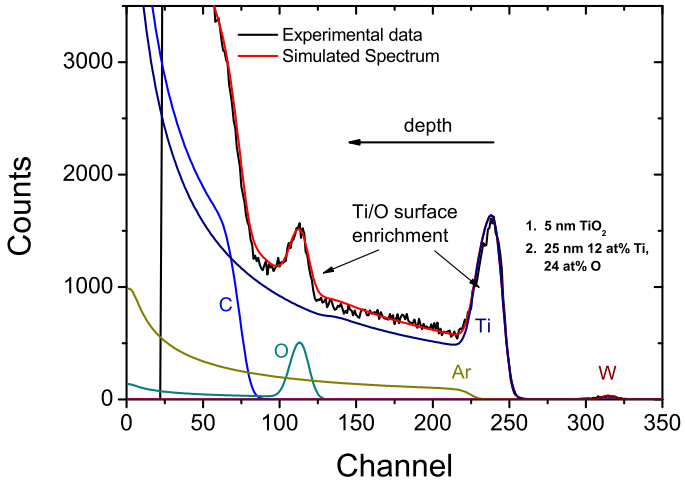

Figure 6.8: *500 keV He^+ RBS spectrum of plasma eroded 3.5 % a-C:Ti sample together with simulated spectrum for quantification of surface composition. A 30 nm thick surface layer is enriched in titanium and oxygen. The fit contains a 5 nm TiO_2 surface followed by 25 nm thick Ti/O enriched layer: 12 % Ti, 24 % O. A slight W contamination (<1 mono-layer) is also visible.*

The increasing erosion yield for some samples in the beginning of an experiment could be due to the plasma start-up phase, until a thermal equilibrium between plasma, sample and wall is achieved.

6.2.2 Influence of pre-annealing

For a-C:Ti samples, pre-annealing before the erosion experiment seems only to influence the erosion yield of the 1 % doped specimen for fluences $<1.5{\cdot}10^{24}$ m^{-2}. Considering the uncertainty of the erosion yield no conclusion for the higher doped samples can be drawn.

For the a-C:V samples an increased erosion yield can be observed, which is attributed to the formation of nm-sized carbide crystallites during pre-annealing. As shown in section 5.2.1, the size of the formed crystallites is significantly larger for the V-doped films compared to a-C:Ti. This should be the reason why only for a-C:V films an effect on the erosion yield is observed.

The increased erosion yield can be explained by the agglomeration of metal in carbide particles during annealing. Therefore, the chemical effect of vanadium on suppressing chemical sputtering of carbon is less pronounced, since a large amount of metal is inside carbide crystallites with less possibilities for interaction on the carbon erosion mechanism. Metal erosion is also observed and shows an influence of pre-annealing, as discussed in the next section.

6.2.3 Metal erosion

Tab. 6.1 summarizes the eroded fraction of carbon and metal for a-C:Ti and a-C:V films as measured by RBS with 1.5 MeV H^+ after the erosion experiment. The layer thickness is almost identical for different metal concentrations (see Tab. 5.1). Less material is removed

Table 6.1: *Removed fraction of carbon and metal for eroded a-C:V and a-C:Ti as quantified by 1.5 MeV H^+. The ratio of eroded metal to carbon and the ion fluence are also given.*

		as-deposited				1100 K pre-annealed			
Dopant	Metal	Removed fraction		Ratio	Fluence	Removed fraction		Ratio	Fluence
	%	C	Me	Me/C	$10^{24}\,m^{-2}$	C	Me	Me/C	$10^{24}\,m^{-2}$
Ti	1.0	0.96	0.56	0.58	2.04	1	0.65	0.65	2.25
	3.5	0.13	0.09	0.69	0.91	0.11	0.22	2	0.79
	7.5	0.03	0.02	0.67	0.41	0.03	0.03	1	0.32
V	1.5	0.27	0.13	0.48	0.91	0.50	0.41	0.82	1.62
	3.5	0.06	0.04	0.67	0.74	0.20	0.21	1.05	1.00
	8.5	0.04	0.02	0.50	0.45	0.08	0.09	1.13	0.45

with increasing metal concentration, due to the lower erosion yield and the lower fluence (Fig. 6.7 and Tab. 6.1). For 1 % a-C:Ti, almost all carbon was removed during both erosion experiments. Also more than half of the titanium vanished. For all unheated films, the removed metal amount is about $\frac{2}{3}$ to $\frac{1}{2}$ of carbon. Since physical sputtering of Ti and V by 30 eV D^+ can be excluded, erosion by He^+, impurity atoms (O, N species) or self sputtering by ionized carbon has to be considered. Therefore, comparison of the erosion yields with ion beam experiments is not possible. As indicated in section 6.1.2 for the ion beam erosion, local hydride formation could also be an explanation for metal erosion. It is known that TiH_2 and VH are formed at atmospheric pressure when the metal is exposed to molecular hydrogen at 600-700 K [182]. During erosion it is likely, that the metal enriched at the surface is in an chemically activated state. Therefore, reaction with atomic hydrogen could lead to hydrides at even lower temperatures. It could be speculated that, if the metal is present as hydride at the surface (and not in metallic or carbidic state), it is more easily removed thermally or by a lower effective sputtering threshold.

The pre-annealed samples show generally higher metal erosion compared to the un-annealed samples: Here, about the same relative material loss is observed for carbon and metal. One possible explanation is the loss of metal-containing particles. Once the carbide particles are exposed at the surface they can become negatively charged and are removed by the electrical field. In the case of films with atomically disperse metal distribution, this effect would be much lower because the metal enrichment leads to a more dense layer without exposed particles. Further investigations have to be performed to clarify this observation. The higher metal erosion compared to carbon for the annealed 3.5 % a-C:Ti film (Tab. 6.1) cannot be explained.

For a-C:W films measurable metal erosion is only observed for the 2.5 % W-doped film (0.02), but much less compared to carbon (0.16). This can be attributed to the higher sputtering threshold for W, therefore sputtering by impurity species should be much lower compared to Ti/V. W does also not form a hydride, therefore no influence of local tungsten-hydrogen interaction is expected.

6.2.4 Morphology

Because of the low surface roughness, the morphology of the eroded samples was mainly studied by AFM. SEM analysis was only possible for the 1 % a-C:Ti and 1.5 % a-C:V since the roughness and therefore topography contrast was high enough. Fig. 6.9 shows SEM micro-

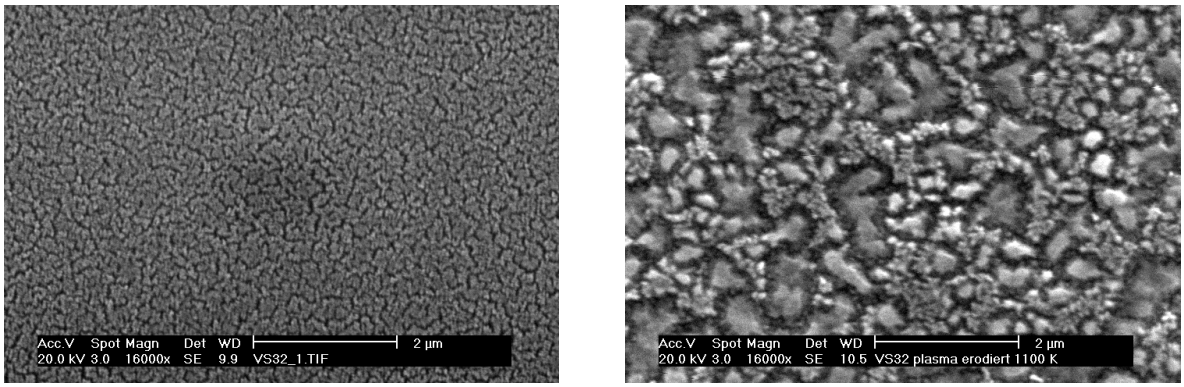

Figure 6.9: *SEM micrographs of 1.5 % a-C:V films after plasma erosion. Left: film without pre-treatment, right: with pre-annealing to 1100 K.*

graphs of the 1.5 % a-C:V films after plasma erosion. Both show a meander-like structure, the pre-annealed sample exhibits a more structured surface on a larger length scale. This could be due to the pre-structuring, but also a result from the longer erosion time: the applied fluence was more than 50 % higher (Tab. 6.1). The eroded 1% a-C:Ti layers showed a similar structure, but since almost all carbon was eroded, the surface is formed by remaining TiO_2.

Films with higher metal concentrations could only be analyzed by AFM. Erosion of pre-annealed films alters its morphology, which is demonstrated in Fig. 6.10 for the 7.5 % a-C:Ti and 8.5 % a-C:V samples. The overall roughness R_q is comparable for all shown surfaces, but the topography is different: Whereas the eroded samples exhibit smoother structures without pre-annealing, the surface morphology show finer structures if annealed before the erosion experiment. This could be explained by the carbide crystallites present in the annealed films, which lead to a less homogeneous and therefore a more structured surface.

Also the visible surface color is different for both sets of eroded samples. Whereas without pre-annealing the surface remains shiny silver, pre-annealing leads to a dark purple color. Adhesion and hardness of the films were also altered: with pre-annealing, the surface of the film became very soft during erosion. The layer could easily scratched and contact AFM scans (used for all other pristine and eroded films) were not possible. Therefore, the respective a-C:V picture in Fig. 6.10 was done in non-contact mode on a AFM at University of Augsburg. An increased hydrogen content could be the reason for the softening. Quantification of the total trapped deuterium content with 1000 keV $^3He^+$ in both eroded 8.5 % a-C:V films showed about 60 % more D in the pre-annealed layer ($1.3{\cdot}10^{16}$ D cm^{-2} compared to $8.3{\cdot}10^{15}$D cm^{-2}). But the total area density of carbon for both films is about 1000 times higher compared to D. Therefore, only a small fraction of carbon is bonded to deuterium. Since a visible amount of the film could be removed by simple rubbing an explanation for the low adhesion could be that the interface to the Si substrate is weakened during annealing. Argon desorption and metal diffusion are processes which occur and could lead to small vacancies. During plasma erosion neutral atomic deuterium could diffuse at the interface region and react with carbon leading to the observed less adhesive film.

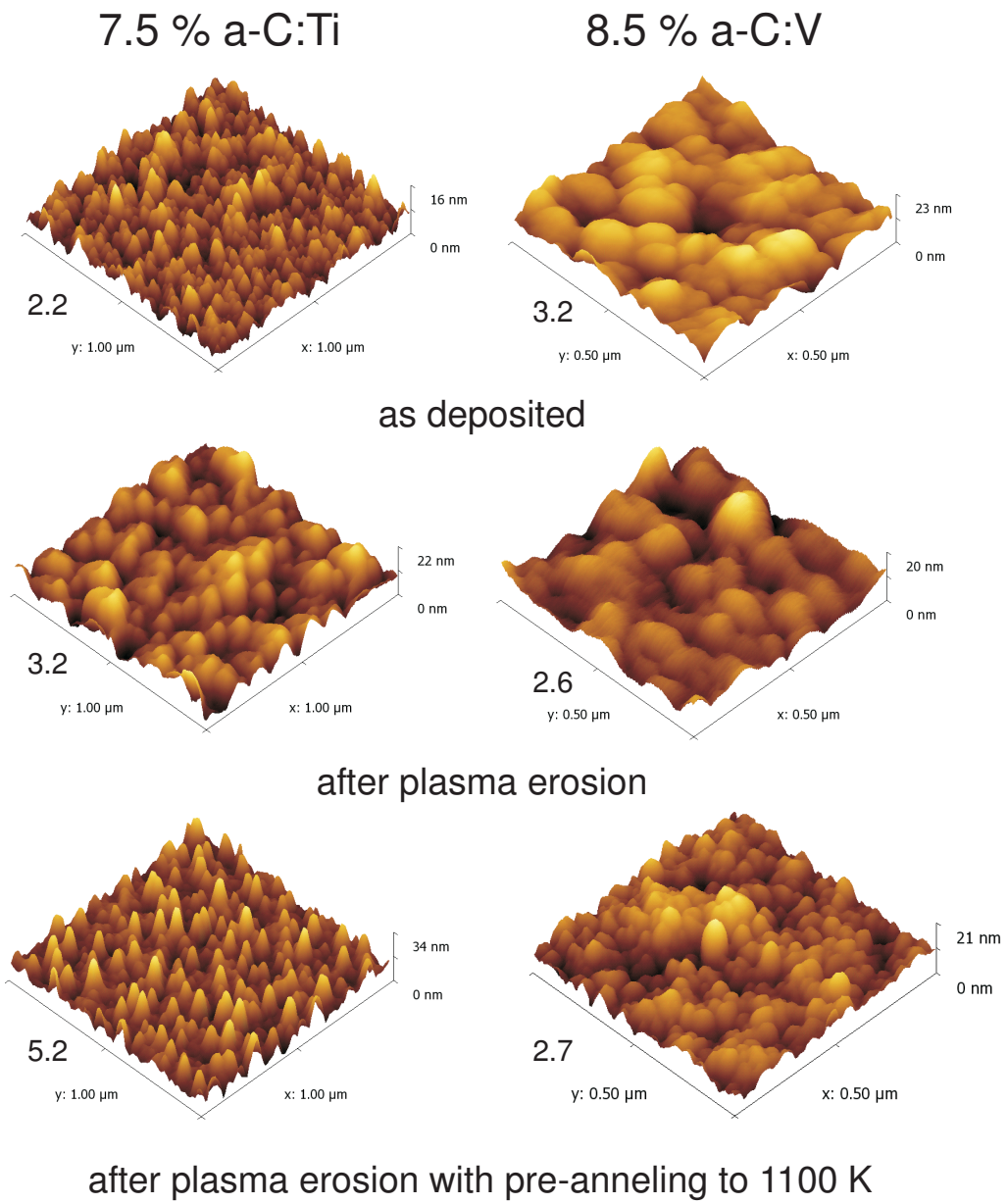

Figure 6.10: *AFM pictures of the surface morphology for pristine and eroded 7.5 % a-C:Ti (1x1 µm) and 8.5 % a-C:V films (0.5x0.5 µm). Plasma erosion was performed at 350 K surface temperature. Pre-annealing leads to a more structured surface after plasma erosion. Due to the soft film surface after erosion, the AFM scan of the pre-annealed a-C:V scan was done with another AFM in non-contact mode. The roughness R_q (in nm) is given for each picture.*

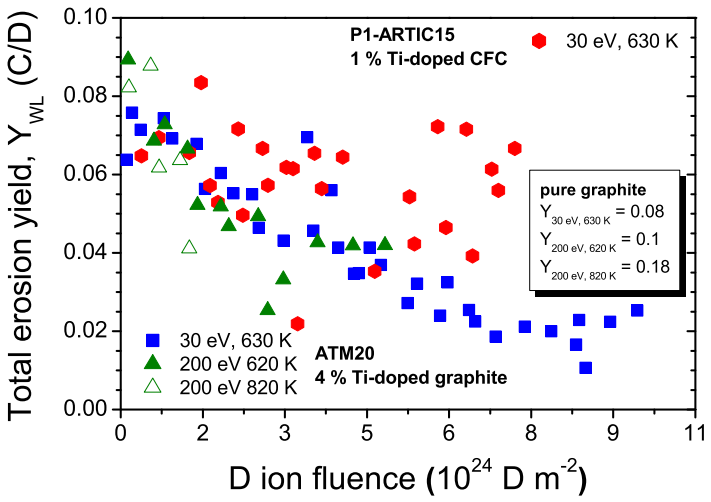

Figure 6.11: *Total erosion yield (Y_{WL}) for Ti-doped graphite (4 % Ti, ATM20) and CFC (1 % Ti, P1-ARTIC15) for 30 and 200 eV D at elevated temperature. The erosion yields of pure graphite are given for comparison.*

6.3 Erosion resistance of doped graphites and CFC

In the frame of ExtreMat the erosion resistance of doped fine-grain graphites and CFC materials was investigated using the high current ion source. Total erosion yields were determined at elevated temperature as function of D ion fluence by measuring the weight-loss (Y_{WL}) of the specimen as described in section 4.3.1. Fig. 6.11 shows the fluence-dependent total erosion yields of 4 % Ti-doped graphite and 1 % Ti-doped CFC at elevated temperatures.

The total erosion yield of undoped graphite at 30 eV D and 630 K – the temperature-maximum of total erosion – is 0.08 [117]. A decreasing erosion yield with ion fluence is observed for the 4 % Ti-doped graphite. After a fluence of $\approx 1 \cdot 10^{25}$ D m^{-2} a constant Y_{WL} of 0.02 is reached for 30 eV D. This indicates that a steady-state erosion yield is achieved, which is four times lower compared to pure graphite. This can be explained by preferential erosion of carbon and protective TiC grain enrichment at the surface. The surface morphology before and after erosion is shown in Fig. 6.12. The carbide grains enrich at the surface and protect the underlying carbon from further erosion. Inside the erosion spot a macroscopically homogeneous surface has formed, as shown in Fig. 6.13a. Since Y_{WL} is about the value for pure graphite at the beginning of the experiment, no chemical influence of the dopants on Y_{surf} is expected.

Erosion experiments with 200 eV D were performed at 620 and 820 K. The latter temperature corresponds to the maximum in the temperature-dependent erosion yield for pure carbon. For erosion at a sample temperature of 620 K, indication for a yield of about 0.04 exist. This corresponds to a reduction by about a factor of 2 compared to pure carbon.

Erosion at 820 K shows a similar reduction, even if the accumulated fluence is not high enough to reach a constant Y_{WL} . The first data points for 200 eV D at 820 K are much lower than 0.18, the erosion yield for pure graphite. At this low fluences, no pronounced shielding

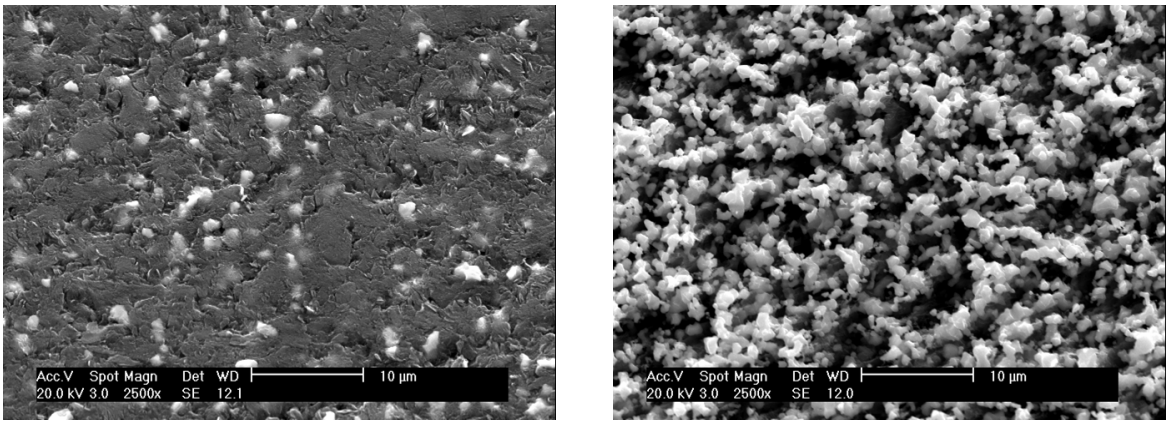

Figure 6.12: *Ti-doped graphite (4 % Ti, ATM20) before (left) and after 30 eV D bombardment (630 K, $1{\cdot}10^{25}$ D m^{-2}).*

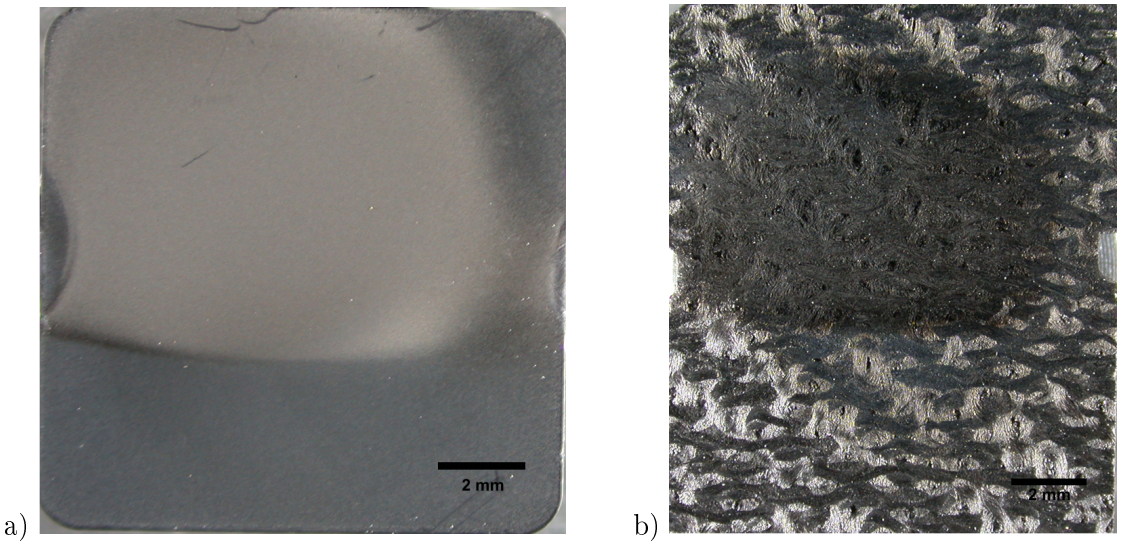

Figure 6.13: *Photographs of a) 4 % Ti-doped graphite (12x12 mm^2) and b) 1 % Ti-doped CFC (12x15 mm^2) after 30 eV D erosion at 630 K. CFC shows loss of matrix between fiber-bundles in the erosion spot.*

effect due to carbide enrichment is possible. Therefore, a chemical influence of doping seems to occur, which can be explained by a lowering of the activation energy for hydrogen release (section 3.2.3).

The erosion experiment of the Ti-doped CFC (30 eV D, 630 K) shows no reduced erosion yield with increasing fluence. This indicates that no significant surface enrichment occurred. Y_{WL} scatters within about 0.06±0.02, which is an indication for macroscopic particle loss. This is confirmed by inspection of the erosion spot shown in Fig. 6.13b. Voids have been created between the fiber bundles, probably due to loss of matrix particles. SEM micrographs of the surface morphology are shown in Fig. 6.14. The pictures on the left side were acquired using secondary electrons (SE mode), giving a good impression of the topography. The BSE mode (backscattered electrons, right side) gives a better material contrast. The un-eroded sample (a) shows that only a low amount of TiC is visible and that TiC particles are not evenly distributed. This is due to the fabrication process (section 4.1.2), where only the matrix is originally doped with TiC. The matrix has not completely penetrated between all fibers during matrix infiltration, therefore TiC is not always present between the fibers.

After erosion (Fig. 6.14b-c) TiC enrichment at the surface has occurred, but no dense surface layer has formed as in the case of graphite (Fig. 6.12). Two factors are responsible. First, the TiC distribution is not homogeneous throughout the sample. In some regions high TiC concentration is obvious, with probably good protection against D erosion. Other regions show no TiC presence. The second problem is the overall too low Ti content. Considering much higher fluences it seems unlikely, that all TiC particles remain on the surface if several fiber diameters have to be eroded before a full TiC surface is created. For the applied fluence about 2/3 of a fiber diameter was eroded. In Fig. 6.14c the typical morphology of eroded fibers is shown. A saw blade-like structure has formed on the fibers. In the BSE picture some TiC particles on top of the structures can be observed.

Summarizing the erosion results it can be concluded that the Ti-doped graphite ATM20 shows a very homogeneous TiC particle distribution which results in an evenly TiC-enriched protective surface region after 30 eV D bombardment at 630 K with a fluence of $1{\cdot}10^{25}$D m^{-2}. A chemical influence of TiC doping is observed for 200 eV D bombardment at 820 K: A reduced erosion yield by a factor of 2 is observed even at the beginning of the experiment at a very low fluence. TiC particles are not homogeneously distributed in the CFC sample P1-ARTIC15, the TiC crystallites are concentrated in 10-100 µm large agglomerates. Additionally, doping with only 1 % Ti seems to be too low to achieve a strong reduction of the erosion yield. To achieve a TiC enriched surface zone higher Ti concentration and better distribution have to be realized. The fiber-matrix adhesion has to be improved since the large scatter in the erosion yield and the observation of voids are indications for macroscopic loss of matrix particles.

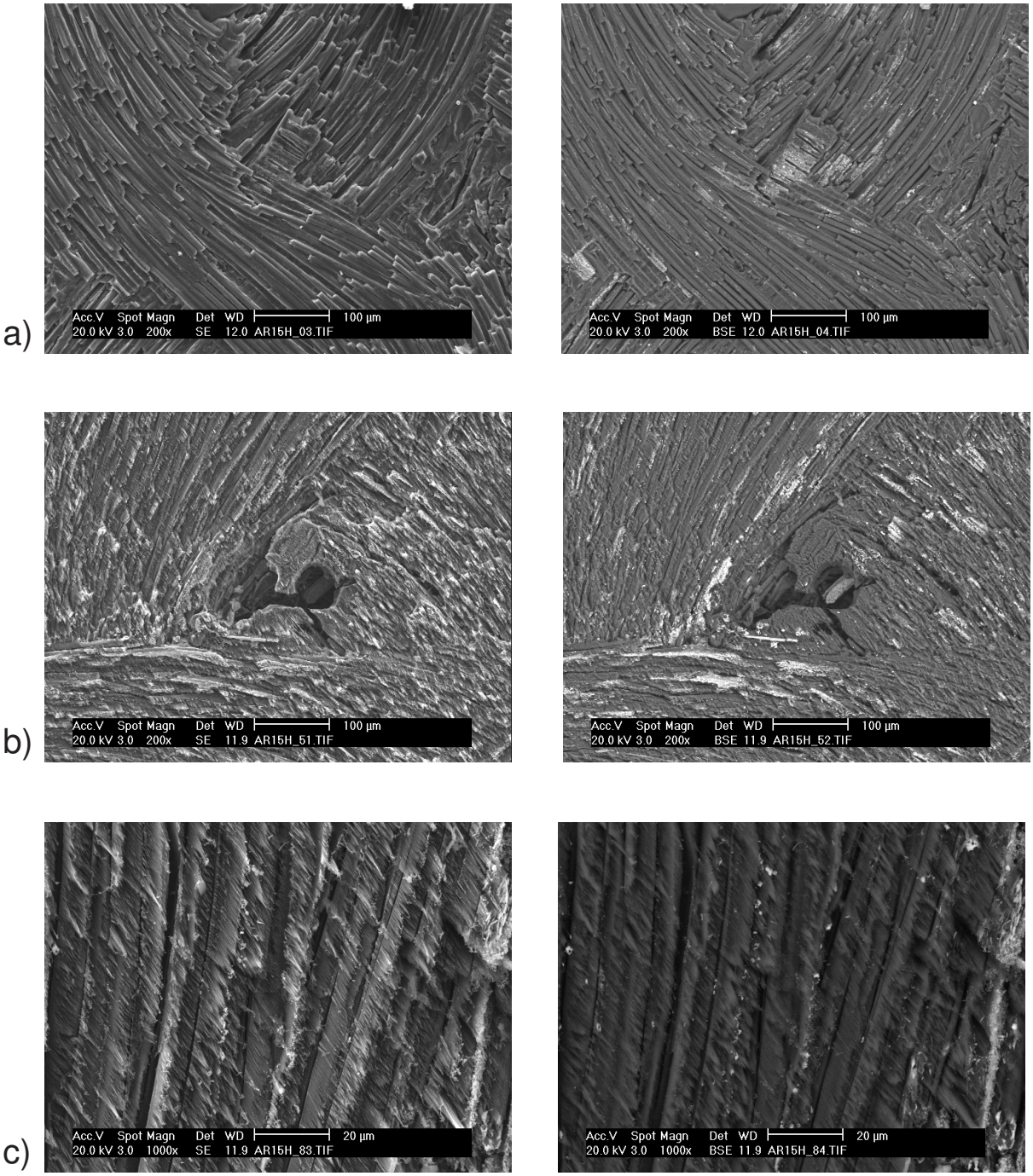

Figure 6.14: *SEM micrographs of Ti-doped CFC before (a) and after (b,c) 30 eV D erosion at 630 K ($7{\cdot}10^{24}$ D m^{-2}). The pictures are generated by detecting secondary electrons (SE, left side) or backscattered electrons (BSE, right side). SE enhances the topography and BSE the material contrast.*

Chapter 7

Conclusion

The main part of this work deals with structural investigations of metal-doped carbon films (a-C:Me), produced by magnetron sputter deposition. Investigations of the a-C:Me film structure found in literature were usually performed on films prepared under conditions to achieve high hardness and wear resistance (see section 3.1). A nanocomposite, consisting of nanometer-sized carbide crystallites in a carbon matrix is desired for such applications, and the metal content is generally >15 %.

However, for erosion investigations under hydrogen impact, films with low metal concentrations are preferred since already low amounts reduce the erosion yield strongly. Also, soft deposition parameters were applied (RT, no bias voltage) to achieve a very disperse metal distribution and to be able to affect the nanostructure by annealing. Therefore, investigations about a-C:Me film structure performed by other research groups are of limited value to clarify the structure of the films used at IPP for erosion studies. This leads to the main focus of this work: the detailed structural characterization of a-C:Me films. Various analytical techniques were applied to achieve a comprehensive view about the nanoscopic structure, dependent on doping metal (Ti, V, Zr, W), metal concentration (0-15 %) and post-annealing temperature (up to 1300 K), as summarized in Fig. 1.2.

The characterization results are divided in two main sections, dealing with investigations of the **metal distribution and phase** and the **structure of the carbon matrix**, and are discussed below.

Metal distribution and phase

The metal bonding state in a-C:Me XAFS and XES investigations – which probe the bulk of the samples – showed generally a carbide-like bonding character of the metal in all investigated a-C:Me films. Only for samples with very low metal concentrations (1 % Ti, 1.5 %V, 1.5 % Zr) the presence of about 2 % oxygen in the films give rise to significant Me–O bonding. The formation of metallic clusters can be excluded.

XPS measurements of a 7.5 % Ti-doped film revealed oxygen-bonded titanium for the as-deposited sample and specimens annealed up to 900 K. The bonding state changed to carbidic for samples annealed to higher temperatures. This observation – which is contrary to the XAFS investigation – is due to the high surface sensitivity of the XPS measurements of only a few nm. Oxygen contamination of the investigated film surface due to storage in air is perhaps responsible for the observed results. This demonstrates that the investigation of the sample

surface is often insufficient in monitoring the bulk properties of the sample. The application of different analytical techniques helps to avoid misleading interpretations.

Ti, V, and Zr distribution in the carbon matrix No crystallinity indicating the formation of carbide crystallites was observed by XRD in as-deposited samples containing Ti and $<8.5\,\%$ V. The corresponding EXAFS showed no significant order beyond the next carbon neighbor, i.e. the metal can be assumed to be mainly distributed atomically disperse in an amorphous environment after deposition. This was also confirmed by TEM investigations. XRD measurements indicate the existence of some very small carbide crystallites (< 1 nm) for Zr concentrations$\geq 7\,\%$. But from interpretation of the EXAFS spectra the distribution of the metal in as-deposited a-C:Zr films is better characterized as amorphous.

Annealing of Ti, V and Zr-doped films leads to formation and growth of carbide crystallites (TiC, VC, ZrC) of several nm in size, giving rise to diffraction peaks in XRD and the development of a local atomic environment similar to the one achieved in crystalline carbide. The carbide crystallite size increases in the order ZrC$<$TiC$<$VC for comparable metal concentrations.

W distribution and tungsten carbide phase XRD measurements performed on a-C:W films indicate formation of small carbide crystallites during deposition even at low tungsten concentrations. A diffraction peak developed with increasing annealing temperature, but even for 1300 K, it remained very broad and the carbide phase could not be resolved. A strong texture or a mixture of different carbide phases could be responsible for the observed peak. Only after annealing to 1300 K the local atomic coordination for the next two atomic neighbors of W is similar to W_2C as indicated by EXAFS. Tungsten L_1-edge NEXAFS measurements probed the local symmetry of W and showed, that formation of a local WC-like coordination only occurs after annealing to 1700 K. After annealing to 1300 K, the local symmetry is similar to W_2C, which confirms the EXAFS results. Calculations showed that also a local coordination as in WC_{1-x} cannot be excluded.

The results can be explained by the formation of very small and strongly distorted carbide crystallites already during deposition and/or a mixture of different carbide phases.

Structure of the carbon matrix

Crystallinity in a-C XRD measurements showed the existence of a crystalline carbon phase in a-C. It can be explained by a small amount of 2-dimensional graphene-like crystallites, present already after deposition. Their number increases with annealing temperature. However, the majority of the carbon is expected to be in an amorphous state, with the sp^2 phase clustered in small distorted aromatic rings and interconnected by a sp^3 network.

Influence of doping on aromatic clustering The addition of metal during C deposition affects the clustering of the sp^2 phase as investigated by Raman spectroscopy. Compared to a-C, the addition of metal leads to an increase of the average aromatic cluster size in the as-deposited films. Ti and Zr have the strongest effect on promoting aromatic clustering. This is in accordance with the observation that both elements are most effective as graphitization catalyst during production of fine-grain graphites at > 2900 K [24]. W has the smallest influence on aromatic clustering, which can be correlated with the formation of crystalline particles

already during deposition. With increasing annealing temperature – which leads to formation and growth of carbide crystallites – the influence of doping on the aromatic cluster size diminishes for all dopants and the carbon phase becomes similar to a-C. After annealing to $\geq$1100 K, the a-C:Me film can be described as a nanocomposite consisting of a-C and carbide. The carbon structure is only determined by the annealing temperature and is independent of doping.

Local carbon bonding state Surface sensitive carbon NEXAFS and XPS measurements were performed to investigate the local carbon bonding and hybridization. NEXAFS revealed an increase of the sp^2 content in pure a-C with annealing from about 80 % (as-deposited) to 95 % (1300 K). Two different sp^2 bonding states could be distinguished in the NEXAFS spectra, originating from sp^2 bonded carbon in an ordered and a more disordered environment. With annealing the ordered state gains in intensity. No quantification of the sp^2 content in a-C:Ti films by NEXAFS was possible. This is probably due to additional intensity arising from Ti–C interaction which overlaps with the energy range used for quantification of sp^2 bonded carbon. For a 7.5 % a-C:Ti sample the NEXAFS spectrum shows an additional peak after annealing to 470 K. This is explained by the formation of carbonyl functionalities in the near surface region due to reaction of non-carbonaceous oxygen with the carbon.

The change of carbon hybridization and sp^2 bonding disorder was investigated by analyzing C 1s XPS spectra for in-situ annealing series of a-C and a-C:Ti. Annealing leads to an increased and better ordered sp^2 component in the surface-near region of a-C. In the case of annealed a-C:Ti, preferably sp^3 bonded carbon atoms react to TiC. The temperature-induced diffusion processes lead to an increased sp^2 disorder.

The second part of this work deals with the **D erosion behavior** of a-C:Me films. It contains first measurements of the temperature dependent CD_4 production yield during 200 eV D impact, and a comparison of the total erosion yield with the CD_4 production yield. A set of plasma erosion experiments were performed, in particular to study the influence of the film nanostructure on the erosion yield.

The erosion behavior of TiC-doped graphite and CFC, produced in the frame of the ExtreMat project, was studied under D ion impact.

D erosion behavior

Temperature dependence of CD_4 production Erosion of pure a-C showed a maximum CD_4 production yield (Y_{CD_4}= 0.08) at 830 K for 200 eV D bombardment. For a-C:Me films, a decreased Y_{CD_4} was observed, especially at temperatures around the maximum. It is explained by a metal-induced decrease of the activation energy for hydrogen recombination (section 3.2.3). This maximum in the temperature dependency shifts to lower temperatures with increasing dopant concentration for all a-C:Me films. The following order in shifting the maximum (and lowering Y_{CD_4}) was observed for the different dopants: V < Ti < Zr (W). It is correlated with the decreasing carbide crystallite size in annealed doped films, found for this sequence. The lowest influence on the chemical sputtering mechanism for V-doping can be explained by the large VC crystallite size, which decreases the interaction of the metal on the chemical sputtering mechanism.

Comparison of total erosion and CD_4 production Metal-doping always leads to a reduced total erosion yield compared to a-C. It is more pronounced for 30 eV D compared to 200 eV D, and for elevated temperature compared to RT. For doped samples the relative decrease of the CD_4 production yield was always significantly lower, in some cases, the CD_4 production even increased. This is explained by a change of the erosion product distribution due to doping. The relative amount of carbon eroded as CD_4 increased mainly at the expense of higher hydrocarbon species.

Influence of nanostructure on the erosion yield An influence of the a-C:Me film nanostructure on the erosion yield during erosion in a RF low pressure plasma was observed for a-C:V films. Erosion of pre-annealed samples (with V present in 3-5 nm large carbide crystallites) led to higher erosion yields compared to erosion of as-deposited samples. This is explained by a lower influence of the dopant on the chemical sputtering mechanism if the metal is present in carbide crystallites. Similar experiments with a-C:Ti showed no influence of pre-annealing, probably due to the smaller carbide crystallite size.

Erosion of doped graphite and CFC The 4 % Ti-doped graphite ATM20 showed a very homogeneous TiC particle distribution which resulted in an evenly TiC-enriched surface region after 30 eV D bombardment at 630 K with a fluence of $1.2 \cdot 10^{25}$ D m^{-2}. After that fluence a total erosion yield of about 0.02 (compared to 0.08 for pure graphite) was achieved due to TiC surface enrichment. A chemical influence of TiC-doping was observed for 200 eV D bombardment at 820 K. The 1 % Ti-doped CFC P1-ARTIC15 suffered from inhomogeneous TiC distribution and a too low dopant concentration. Loss of macroscopic matrix particles during 30 eV D erosion resulted in a large scatter of the total erosion yield: 0.06 ± 0.02.

Chapter 8

List of publications, talks and posters

8.1 Publications

1. C. Adelhelm, M. Balden, M. Sikora. *EXAFS investigation of the thermally induced structuring of titanium-doped amorphous carbon films.* Materials Science and Engineering: C, 27(5-6):1423-1427, 2007.

2. C. Adelhelm, M. Balden, F. Kost, A. Herrmann, S. Lindig. *Thermal induced structural changes of a-C and a-C:Ti films analyzed by NEXAFS and XPS.* Journal of Physics: Conference Series, accepted.

3. C. Adelhelm, M. Balden, M. Rinke, M. Stüber. *Influence of metal-doping and annealing on the Raman spectra of amorphous carbon films*, to be submitted.

4. M. Balden, C. Adelhelm. *Characterization and erosion of metal-containing carbon films,* Physica Scripta T128:121-126, 2007.

5. M. Balden, C. Adelhelm, E. de Juan Pardo, J. Roth. *Chemical erosion by deuterium impact on carbon films doped with nanometer-sized carbide crystallites,* Journal of Nuclear Materials, 363-365:1173-1178, 2007.

6. M. Balden, C. Adelhelm, M. Sikora. *Thermal stability and nano-structure of metal-doped carbon layers,* Journal of Nuclear Materials, 367-370:1458-1462, 2007.

7. M. Balden, C. Adelhelm, T. Köck, A. Herrmann, J. Jaimerena-Muga. *Thermal nanostructuring of metal-containing carbon films and their nanoindentation testing*, Reviews on Advanced Materials Science, 15(2):95-104, 2007.

8. P. Starke, C. Adelhelm, M. Balden. *Erosion behavior of metal-doped carbon layers in deuterium low pressure plasmas and the determination by optical emission spectroscopy*, Contributions to Plasma Physics, 47(7):530-536, 2007.

9. C. García-Rosales, I. López-Galilea, N. Ordás, C. Adelhelm, M. Balden, G. Pintsuk, M. Grattarola, C. Gualco. *Ti-doped isotropic graphite: a promising armour material for plasma-facing components*, submitted.

8.2 Oral conference presentations

1. C. Adelhelm, M. Balden, F. Kost, A. Herrmann, S. Lindig, M. Rinke, M. Stüber. *Influence of metal doping and annealing on the structure of amorphous carbon films*, 17th International Vacuum Congress (IVC-17), 2.-6.07.2007, Stockholm, Sweden.

2. C. Adelhelm, M. Balden, P. Starke, A. Centeno, C. Blanco, I. López Galilea and C. García-Rosales. *Deuterium ion beam and plasma exposure experiments of metal-doped carbon materials relevant for fusion applications*, Euromat 2007, 10.-13.09.2007, Nürnberg.

8.3 Poster presentations

1. C. Adelhelm, M. Balden, E. de Juan Pardo. *Characterisation and erosion behavior of nano-structured metal doped carbon layers*, Nordic and European Summer School in Synchrotron Radiation, 13.-20.06.2005, Lund, Sweden.

2. C. Adelhelm, M. Balden. *Investigations on the thermally induced structuring of metal-doped amorphous carbon films*, HASYLAB Users Meeting, 26.-27.01.2006, Hamburg.

3. C. Adelhelm, M. Balden, M. Sikora. *EXAFS investigations on the thermally induced nano-structuring of metal-doped carbon films.* E-MRS Spring Meeting, Symposium A, 29.05.-02.06.2006, Nice, France.

4. M. Balden, C. Adelhelm, *Characterization of metal-doped carbon layers for chemical erosion studies*, E-MRS Spring Meeting, Symposium N, 29.05.-02.06.2006, Nice, France.

5. M. Balden, C. Adelhelm, E. De Juan Pardo, J. Roth. *Chemical erosion by deuterium impact of carbon films doped with nanometer-sized carbide crystallites*, 17th International Conference on Plasma Surface Interactions in Controlled Fusion Devices (PSI 17), 22.-26.05.2006, Hefei Anhui, China.

6. P. Starke, C. Adelhelm, M. Balden, U. Fantz, A. Centeno, C. Blanco. *Erosionsausbeuten dotierter Kohlenstoffmaterialien in Deuterium-Niedertemperaturplasmen*, Frühjahrstagung der DPG, 19.-23.03.2007, Düsseldorf.

7. P. Starke, C. Adelhelm, M. Balden, U. Fantz. *Chemical erosion of doped carbon layers in deuterium low pressure RF plasmas*, Euromat 2007, 10.-13.09.2007, Nürnberg.

8. C. Adelhelm, M. Balden, E. Cochran and S. Denis. *Protection of carbon films against chemical erosion by doping with transition metals*, E-MRS Spring Meeting, Symposium Q, 28.05.-01.06.2007, Strasbourg, France.

Bibliography

[1] International Energy Agency (IEA). *World Energy Outlook*. 2006.

[2] www.bgr.bund.de. Bundesanstalt für Geowissenschaften und Rohstoffe.

[3] Intergovernmental Panel on Climate Change (IPCC). *Climate Change 2007 - Mitigation of Climate Change: Working Group III Contribution to the Fourth Assessment Report of the IPCC*. Cambridge University Press, 2007.

[4] U. Schumacher. Status and problems of fusion reactor development. *Naturwissenschaften*, 88(3):102–112, 2001.

[5] G. Federici, A. Loarte, and G. Strohmayer. Assessment of erosion of the ITER divertor targets during type I ELMs. *Plasma Phys. Control. Fusion*, 45(9):1523–1547, 2003.

[6] V. Barabash, A. Peacock, S. Fabritsiev, G. Kalinin, S. Zinkle, A. Rowcliffe, J. W. Rensman, A. A. Tavassoli, P. Marmy, P. J. Karditsas, F. Gillemot, and M. Akiba. Materials challenges for ITER - current status and future activities. *J. Nucl. Mater.*, 367-370(Part 1):21–32, 2007.

[7] V. Barabash, G. Federici, R. Matera, A. R. Raffray, and Iter Home Teams. Armour materials for the ITER plasma facing components. *Phys. Scr.*, T81:74–83, 1999. l.

[8] R. Tivey, M. Akiba, D. Driemeyer, I. Mazul, M. Merola, and M. Ulrickson. ITER R&D: Vacuum vessel and in-vessel components: Divertor cassette. *Fusion Eng. Des.*, 55(2-3):219–229, 2001.

[9] M. Merola, G. Vieider, M. Bet, I. Bobin Vastra, L. Briottet, P. Chappuis, K. Cheyne, G. Dell'Orco, D. Duglue, R. Duwe, S. Erskine, F. Escourbiac, M. Febvre, M. Grattarola, F. Moreschi, A. Orsini, R. Pamato, L. Petrizzi, L. Plochl, B. Riccardi, E. Rigal, M. Rodig, J. F. Salavy, B. Schedler, J. Schlosser, S. Tahtinen, R. Vesprini, E. Visca, and C. H. Wu. European achievements for ITER high heat flux components. *Fusion Eng. Des.*, 56-57:173–178, 2001.

[10] Alberto Loarte. Implications of the use of carbon-based plasma facing components in next step fusion devices. *Phys. Scr.*, T111:13–22, 2004.

[11] G. Federici, C. H. Skinner, J. N. Brooks, J. P. Coad, C. Grisolia, A. A. Haasz, A. Hassanein, V. Philipps, C. S. Pitcher, J. Roth, W. R. Wampler, and D. G. Whyte. Plasma-material interactions in current tokamaks and their implications for next step fusion reactors. *Nucl. Fusion*, 41(12):1967–2137, 2001.

[12] V. Philipps, M. Stamp, A. Pospieszczyk, A. Huber, A. Kirschner, and E. Vietzke. Chemical erosion behaviour of carbon materials in fusion devices. *J. Nucl. Mater.*, 313-316:354–359, 2003.

[13] *Radiological Source Terms 2002 ITER Technical Basis. ITER EDA Documentation Series No. 24.* IAEA, 2002.

[14] T. Tanabe, N. Bekris, P. Coad, C. H. Skinner, M. Glugla, and N. Miya. Tritium retention of plasma facing components in tokamaks. *J. Nucl. Mater.*, 313-316:478–490, 2003.

[15] R. D. Penzhorn, N. Bekris, U. Berndt, J. P. Coad, H. Ziegler, and W. Nagele. Tritium depth profiles in graphite and carbon fibre composite material exposed to tokamak plasmas. *J. Nucl. Mater.*, 288(2-3):170–178, 2001.

[16] C. H. Skinner and G. Federici. Is carbon a realistic choice for ITER's divertor? *Phys. Scr.*, T124:18–22, 2006.

[17] C. Grisolia, G. Counsell, G. Dinescu, A. Semerok, N. Bekris, P. Coad, C. Hopf, J. Roth, M. Rubel, A. Widdowson, and E. Tsitrone. Treatment of ITER plasma facing components: Current status and remaining open issues before ITER implementation. *Fusion Eng. Des.*, In Press, Corrected Proof.

[18] K. Krieger, W. Jacob, D. L. Rudakov, R. Bastasz, G. Federici, A. Litnovsky, H. Maier, V. Rohde, G. Strohmayer, W. P. West, J. Whaley, and C. P. C. Wong. Formation of deuterium-carbon inventories in gaps of plasma facing components. *J. Nucl. Mater.*, 363-365:870–876, 2007.

[19] M. J. Rubel, J. P. Coad, P. Wienhold, G. Matthews, V. Philipps, M. Stamp, and T. Tanabe. Fuel inventory and co-deposition in grooves and gaps of divertor and limiter structures. *Phys. Scr.*, T111:112–117, 2004.

[20] M. Balden. Overview on the effects of dopants on chemical erosion and RES of carbon-based materials. *Phys. Scr.*, T81:64–69, 1999.

[21] C. Garcia-Rosales and M. Balden. Chemical erosion of doped graphites for fusion devices. *J. Nucl. Mater.*, 290:173–179, 2001.

[22] J. P. Bonal, C. H. Wu, and D. Gosset. Simulation experimental investigation of plasma off-normal events on advanced silicon doped CFC-NS31. *J. Nucl. Mater.*, 307-311:100–105, 2002.

[23] I. Lopez-Galilea, C. Garcia-Rosales, G. Pintsuk, and J. Linke. Development of finely dispersed Ti- and Zr-doped isotropic graphites for the divertor of next step fusion devices. *Phys. Scr.*, T128:60–65, 2007.

[24] C. Garcia-Rosales, N. Ordas, E. Oyarzabal, J. Echeberria, M. Balden, S. Lindig, and R. Behrisch. Improvement of the thermo-mechanical properties of fine grain graphite by doping with different carbides. *J. Nucl. Mater.*, 307:1282–1288, 2002.

[25] Q. G. Guo, J. G. Li, N. Noda, Y. Kubota, J. L. Chen, Z. J. Liu, L. Liu, and J. R. Song. Selection of candidate doped graphite materials as plasma facing components for HT-7U device. *J. Nucl. Mater.*, 313:144–148, 2003.

[26] G. N. Luo, X. D. Zhang, D. M. Yao, X. Z. Gong, J. L. Chen, Z. S. Yang, Q. Li, B. Shi, and J. G. Li. Overview of plasma-facing materials and components for EAST. *Phys. Scr.*, T128:1–5, 2007.

[27] W. Bohmeyer, A. Markin, D. Naujoks, B. Koch, G. Krenz, M. Baudach, and G. Fussmann. Decomposition and sticking of hydrocarbons in the plasma generator PSI-2. *J. Nucl. Mater.*, 363-365:127–130, 2007.

[28] M. J. Baldwin, R. P. Doerner, D. Nishijima, K. Schmid, D. G. Whyte, J. G. Kulpin, and G. Wright. Mixed-material layer formation on graphite exposed to deuterium plasmas containing beryllium. *J. Nucl. Mater.*, 358(2-3):96–105, 2006.

[29] F. W. Meyer, L. I. Vergara, and H. F. Krause. Recent ORNL measurements of chemical sputtering of ATJ graphite by slow atomic and molecular D ions. *Phys. Scr.*, T124:44–49, 2006.

[30] J. Pamela, G. F. Matthews, V. Philipps, and R. Kamendje. An ITER-like wall for JET. *J. Nucl. Mater.*, 363-365:1–11, 2007.

[31] A. Kallenbach, R. Dux, J. Harhausen, C. F. Maggi, R. Neu, T. Pütterich, V. Rohde, K. Schmid, and E. Wolfrum. Spectroscopic investigation of carbon migration with tungsten walls in ASDEX Upgrade. *J. Nucl. Mater.*, 363-365:60–65, 2007.

[32] H. J. N. van Eck, W. R. Koppers, G. J. van Rooij, W. J. Goedheer, B. de Groot, P. Smeets, J. Scholten, M. van de Pol, S. Brons, R. Koch, B. Schweer, U. Samm, V. Philipps, R. A. H. Engeln, D. C. Schram, N. J. Lopes Cardozo, and A. W. Kleyn. Pre-design of Magnum-PSI: A new plasma-wall interaction experiment. *Fusion Eng. Des.*, In Press, Corrected Proof.

[33] E. de Juan Pardo, M. Balden, B. Cieciwa, C. Garcia-Rosales, and J. Roth. Erosion processes of carbon materials under hydrogen bombardement and their mitigation by doping. *Phys. Scr.*, T111:62–67, 2004.

[34] M. Balden, C. Garcia-Rosales, R. Behrisch, J. Roth, P. Paz, and J. Etxeberria. Chemical erosion of carbon doped with different fine-grain carbides. *J. Nucl. Mater.*, 290:52–56, 2001.

[35] M. Balden, J. Roth, and C. H. Wu. Thermal stability and chemical erosion of the silicon doped CFC material NS31. *J. Nucl. Mater.*, 258-263(Part 1):740–744, 1998.

[36] R. Schwörer, H. Plank, and J. Roth. Reduction of the chemical erosion of doped graphite due to surface modification during low energy D+ bombardment. *J. Nucl. Mater.*, 241-243:1156–1159, 1997.

[37] W. Eckstein, C. Garcia-Rosales, and J. Roth. *Sputtering Data, Tech. Rep. IPP 9/82.* 1993.

[38] J. Roth, J. Bohdansky, and K. L. Wilson. Erosion of carbon due to bombardment with energetic ions at temperatures up to 2000 K. *J. Nucl. Mater.*, 111-112:775–780, 1982.

[39] M. Balden, E. D. Pardo, I. Quintana, B. Cieciwa, and J. Roth. Deuterium-induced chemical erosion of carbon-metal layers. *J. Nucl. Mater.*, 337-39(1-3):980–984, 2005.

[40] M. Balden, B. T. Cieciwa, I. Quintana, E. de Juan Pardo, F. Koch, M. Sikora, and B. Dubiel. Metal-doped carbon films obtained by magnetron sputtering. *Surf. Coat. Technol.*, 200(1-4):413–417, 2005.

[41] D. Nilsson, F. Svahn, U. Wiklund, and S. Hogmark. Low-friction carbon-rich carbide coatings deposited by co-sputtering. *Wear*, 254(11):1084–1091, 2003.

[42] M. Stüber, H. Leiste, S. Ulrich, H. Holleck, and D. Schild. Microstructure and properties of low friction TiC-C nanocomposite coatings deposited by magnetron sputtering. *Surf. Coat. Technol.*, 150(2-3):218–226, 2002.

[43] J. S. Zabinski and A. A. Voevodin. Recent developments in the design, deposition, and processing of hard coatings. *J. Vac. Sci. Technol. A*, 16(3):1890–1900, 1998. Part 2.

[44] A. A. Voevodin, C. Rebholz, J. M. Schneider, P. Stevenson, and A. Matthews. Wear-resistant composite coatings deposited by electron enhanced closed field unbalanced magnetron sputtering. *Surf. Coat. Technol.*, 73(3):185–197, 1995.

[45] www.extremat.org.

[46] J. C. Vickerman. *Surface Analysis - The Principal Techniques.* Wiley, Chichester, 2000.

[47] H. Bubert, H. Jennet, editor. *Surface and Thin Film Analysis. Principles, Instrumentation, Applications.* Wiley-VCH, Weinheim, 2002.

[48] J.W. Edington. *Practical Electron Microscopy in Materials Science.* CBLS, Marietta, 2007.

[49] C. B. Williams, D. B. Carter. *Transmission Electron Microscopy. A Textbook for Materials Science*, volume 1-4. Springer, New York, 1996.

[50] B.D. Cullity. *Elements of X-Ray Diffraction.* Addison-Wesley. 1967.

[51] M. Birkholz. *Thin Film Analysis by X-Ray Scattering.* Wiley-VCH, Weinheim, 2006.

[52] Y. Lifshitz. Pitfalls in amorphous carbon studies. *Diamond Relat. Mater.*, 12(2):130–140, 2003.

[53] B. Schrader. *Infrared and Raman Spectroscopy.* VCH, Weinheim, 1995.

[54] A. C. Ferrari and J. Robertson. Interpretation of Raman spectra of disordered and amorphous carbon. *Phys. Rev. B*, 61(20):14095–14107, 2000.

[55] F. Tuinstra and J. L. Koenig. Raman spectrum of graphite. *J. Chem. Phys.*, 53(3):1126–1130, 1970.

[56] R. Gago, M. Vinnichenko, H. U. Jager, A. Y. Belov, I. Jimenez, N. Huang, H. Sun, and M. F. Maitz. Evolution of sp(2) networks with substrate temperature in amorphous carbon films: Experiment and theory. *Phys. Rev. B*, 72(1):014120–9, 2005.

[57] H. X. Li, T. Xu, C. B. Wang, J. M. Chen, H. D. Zhou, and H. W. Liu. Annealing effect on the structure, mechanical and tribological properties of hydrogenated diamond-like carbon films. *Thin Solid Films*, 515(4):2153–2160, 2006.

[58] S. Prawer, K. W. Nugent, Y. Lifshitz, G. D. Lempert, E. Grossman, J. Kulik, I. Avigal, and R. Kalish. Systematic variation of the raman spectra of DLC films as a function of sp(2):sp(3) composition. *Diamond Relat. Mater.*, 5(3-5):433–438, 1996.

[59] J. Diaz, S. Anders, X. Zhou, E. J. Moler, S. A. Kellar, and Z. Hussain. Analysis of the pi* and sigma* bands of the x-ray absorption spectrum of amorphous carbon. *Phys. Rev. B*, 64(12):125204–19, 2001.

[60] C. Ziebert, M. Rinke, M. Stüber, S. Ulrich, and H. Holleck. Interfaces and temperature stability of stepwise graded DLC films studied by nanoindentation and Raman spectroscopy. *Surf. Coat. Technol.*, 200(1-4):1127–1131, 2005.

[61] T. E. Doyle and J. R. Dennison. Vibrational dynamics and structure of graphitic amorphous-carbon modeled using an embedded-ring approach. *Phys. Rev. B*, 51(1):196–200, 1995.

[62] R. N. Tarrant, O. Warschkow, and D. R. McKenzie. Raman spectra of partially oriented sp(2) carbon films: Experimental and modelled. *Vib. Spectrosc.*, 41(2):232–239, 2006.

[63] R. O. Dillon, J. A. Woollam, and V. Katkanant. Use of Raman-scattering to investigate disorder and crystallite formation in as-deposited and annealed carbon-films. *Phys. Rev. B*, 29(6):3482–3489, 1984.

[64] D. G. McCulloch, S. Prawer, and A. Hoffman. Structural investigation of xenon-ion-beam-irradiated glassy-carbon. *Phys. Rev. B*, 50(9):5905–5917, 1994.

[65] M. V. Klein. *Light Scattering in Solids III*, volume 51 of *Topics in Applied Physics*. Springer-Verlag, Berlin, 1982.

[66] C. Lenardi, P. Piseri, V. Briois, C. E. Bottani, A. L. Bassi, and P. Milani. Near-edge x-ray absorption fine structure and raman characterization of amorphous and nanostructured carbon films. *J. Appl. Phys.*, 85(10):7159–7167, 1999.

[67] G. Abrasonis, R. Gago, M. Vinnichenko, U. Kreissig, A. Kolitsch, and W. Moller. Sixfold ring clustering in sp(2)-dominated carbon and carbon nitride thin films: A Raman spectroscopy study. *Phys. Rev. B*, 73(12):125427–13, 2006.

[68] M. Newville. Fundamentals of XAFS. http://xafs.org/Tutorials, 2004.

[69] http://en.wikipedia.org/wiki/XAFS, 2007.

[70] D.C. Koningsberger and R. Prins. *X-Ray Absorption. Principles, Applications, Techniques of EXAFS, SEXAFS and XANES*, volume 92 of *Chemical Analyis*. John Wiley & Sons, New York, 1988.

[71] http://leonardo.phys.washington.edu/feff/. FEFF8, 2006.

[72] J. Stöhr. *NEXAFS spectroscopy*. Springer Series in Surface Sciences. Springer, Berlin, 1992.

[73] B. Watts, L. Thomsen, and P. C. Dastoor. Methods in carbon K-edge NEXAFS: Experiment and analysis. *J. Electron Spectrosc. Relat. Phenom.*, 151(2):105–120, 2006.

[74] P. Glatzel and U. Bergmann. High resolution 1s core hole x-ray spectroscopy in 3d transition metal complexes - electronic and structural information. *Coord. Chem. Rev.*, 249(1-2):65–95, 2005.

[75] U. Bergmann, C. R. Horne, T. J. Collins, J. M. Workman, and S. P. Cramer. Chemical dependence of interatomic x-ray transition energies and intensities - a study of Mn K beta" and K beta(2,5) spectra. *Chem. Phys. Lett.*, 302(1-2):119–124, 1999.

[76] M.P. Seah and W.A Dench. Quantitative electron spectroscopy of surfaces: A standard data base for electron inelastic mean free paths in solids. *Surf. Interface Anal.*, 1(1):2–11, 1979.

[77] M. Tesmer, J.R. Nastasi, editor. *Handbook of Modern Ion Beam Materials Analysis.* Materials Research Society, Pittsburgh, US, 1995.

[78] W.-K. Chu, J.W. Mayer, and M.-A. Nicolet. *Backscattering Spectrometry.* Academic Press, New York, 1978.

[79] M. Mayer. *SIMNRA User's Guide, Tech. Rep. IPP 9/113.* 1997.

[80] J.E. Mahan. *Physical Vapor Deposition of Thin Films.* Wiley, New York, 2000.

[81] M. Ohring. *The Materials Science of Thin Films.* Academic Press, San Diego, US, 1992.

[82] P. Sigmund. Sputtering by ion bombardment: Theoretical concepts. In R. Behrisch, editor, *Sputtering by Particle Bombardment I: Physical Sputtering of Single-Element Solids*, volume 47 of *Topics in Applied Physics.* Springer, Berlin, 1981.

[83] W. O. Hofer. Angular, energy, and mass distribution of sputtered particles. In R. Behrisch, editor, *Sputtering by Particle Bombardment III: Characteristics of Sputtered Particles, Technical Applications*, volume 64 of *Topics in Applied Physics.* Springer, Berlin, 1981.

[84] S.R.P. Silva. *Properties of Amorphous Carbon*, volume 29 of *EMIS Datareviews Series.* 2003.

[85] J. Diaz, O. R. Monteiro, and Z. Hussain. Structure of amorphous carbon from near-edge and extended x-ray absorption spectroscopy. *Physical Review B*, 76(9), 2007. 094201.

[86] J. C. Han, W. Gao, J. Q. Zhu, S. H. Meng, and W. T. Zheng. Density-functional theory study of the microstructure, electronic structure, and optical properties of amorphous carbon. *Physical Review B*, 75(15), 2007. 155418.

[87] J. Robertson and E. P. Oreilly. Electronic and atomic-structure of amorphous-carbon. *Phys. Rev. B*, 35(6):2946–2957, 1987.

[88] M. Cote, J. C. Grossman, M. L. Cohen, and S. G. Louie. Theoretical study of a three-dimensional all-sp(2) structure. *Physical Review B*, 58(2):664–668, 1998.

[89] P. K. Chu and L. H. Li. Characterization of amorphous and nanocrystalline carbon films. *Mater. Chem. Phys.*, 96(2-3):253–277, 2006.

[90] VDI-Richtlinie VDI 2840. Kohlenstoffschichten. Grundlagen, Schichttypen und Eigenschaften, 2005.

[91] H. Dimigen, H. Hubsch, and R. Memming. Tribological and electrical-properties of metal-containing hydrogenated carbon-films. *Appl. Phys. Lett.*, 50(16):1056–1058, 1987.

[92] K. Bewilogua, C. V. Cooper, C. Specht, J. Schroder, R. Wittorf, and M. Grischke. Effect of target material on deposition and properties of metal-containing DLC (Me-DLC) coatings. *Surf. Coat. Technol.*, 132(2-3):275–283, 2000.

[93] A. A. Voevodin, S. V. Prasad, and J. S. Zabinski. Nanocrystalline carbide amorphous carbon composites. *J. Appl. Phys.*, 82(2):855–858, 1997.

[94] S. Zhang, X. Lam Bui, X.T. Zeng, and X. Li. Towards high adherent and tough a-c coatings. *Thin Solid Films*, 482(1-2):138–144, 2005.

[95] W. J. Meng, R. C. Tittsworth, J. C. Jiang, B. Feng, D. M. Cao, K. Winkler, and V. Palshin. Ti atomic bonding environment in Ti-containing hydrocarbon coatings. *J. Appl. Phys.*, 88(5):2415–2422, 2000.

[96] B. Feng, D. M. Cao, W. J. Meng, J. Xu, R. C. Tittsworth, L. E. Rehn, P. M. Baldo, and G. L. Doll. Characterization of microstructure and mechanical behavior of sputter deposited Ti-containing amorphous carbon coatings. *Surf. Coat. Technol.*, 148(2-3):153–162, 2001.

[97] A. Y. Wang, K. R. Lee, J. P. Ahn, and J. H. Han. Structure and mechanical properties of W incorporated diamond-like carbon films prepared by a hybrid ion beam deposition technique. *Carbon*, 44(9):1826–1832, 2006.

[98] E. Lewin, O. Wilhelmsson, and U. Jansson. Nanocomposite nc-TiC/a-C thin films for electrical contact applications. *J. Appl. Phys.*, 100(5):054303–10, 2006.

[99] S. J. Park, K. R. Lee, D. H. Ko, and K. Y. Eun. Microstructure and mechanical properties of WC-C nanocomposite films. *Diamond Relat. Mater.*, 11(10):1747–1752, 2002.

[100] A. A. Voevodin, J. P. O'Neill, S. V. Prasad, and J. S. Zabinski. Nanocrystalline WC and WC/a-C composite coatings produced from intersected plasma fluxes at low deposition temperatures. *J. Vac. Sci. Technol. A*, 17(3):986–992, 1999.

[101] Rusli, S. F. Yoon, H. Yang, J. Ahn, Q. F. Huang, Q. Zhang, Y. P. Guo, C. Y. Yang, E. J. Teo, A. T. S. Wee, and A. C. H. Huan. Investigation of tungsten incorporated amorphous carbon film. *Thin Solid Films*, 355-356:174–178, 1999.

[102] A.A. Magerl A.J. Gusev, A.I. Rempel. *Disorder and Order in Strongly Nonstoichiometric Compounds Transition Metal Carbides, Nitrides and Oxides*, volume 47 of *Springer Series in Materials Science*. Springer, Berlin, 2001.

[103] H.O. Pierson. *Handbook of Refractory Carbides and Nitrides Properties, Characteristics, Processing and Applications*. Materials Science and Process Technology Series. Noyes, Westwood, 1996.

[104] R. Behrisch and W. Eckstein. *Sputtering by Particle Bombardment. Experiments and Computer Calculations from Threshold to MeV Energies*, volume 110 of *Topics in Applied Physics*. Springer, Berlin, 2007.

[105] H. F. Winters and J. W. Coburn. Surface science aspects of etching reactions. *Surface Science Reports*, 14(4-6):161–269, 1992.

[106] A. Horn, A. Schenk, J. Biener, B. Winter, C. Lutterloh, M. Wittmann, and J. Küppers. H-atom impact-induced chemical erosion reaction at c-h film surfaces. *Chem. Phys. Lett.*, 231(2-3):193–198, 1994.

[107] J. Küppers. The hydrogen surface chemistry of carbon as a plasma facing material. *Surface Science Reports*, 22(7-8):251–321, 1995.

[108] E. Vietzke, K. Flaskamp, and V. Philipps. Hydrocarbon formation in the reaction of atomic-hydrogen with pyrolytic-graphite and the synergistic effect of argon ion-bombardment. *J. Nucl. Mater.*, 111(NOV-):763–768, 1982.

[109] E. Vietzke, K. Flaskamp, and V. Philipps. Differences in the ch3 and ch4 formation from graphite under bombardment with hydrogen-ions and hydrogen-atoms argon ions. *J. Nucl. Mater.*, 128(DEC):545–550, 1984.

[110] J. W. Davis, A. A. Haasz, and P. C. Stangeby. Hydrocarbon formation due to combined h-+ ion and h-0 atom impact on pyrolytic-graphite. *J. Nucl. Mater.*, 155:234–240, 1988. Part A.

[111] E. Vietzke, K. Flaskamp, V. Philipps, G. Esser, P. Wienhold, and J. Winter. Chemical erosion of amorphous hydrogenated carbon-films by atomic and energetic hydrogen. *J. Nucl. Mater.*, 147:443–447, 1987.

[112] E. Vietzke, V. Philipps, K. Flaskamp, P. Koidl, and C. Wild. The reaction of atomic-hydrogen with a-c-h and diamond films. *Surface & Coatings Technology*, 47(1-3):156–161, 1991.

[113] A. A. Haasz and J. W. Davis. Comparison of the chemical erosion of carbon carbon composites and pyrolytic-graphite. *J. Nucl. Mater.*, 175(1-2):84–89, 1990.

[114] R. Yamada. Chemical sputtering yields of graphite. *J. Nucl. Mater.*, 147:359–363, 1987.

[115] B. V. Mech, A. A. Haasz, and J. W. Davis. Chemical erosion of pyrolytic graphite by low-energy h+ and d+ impact. *J. Nucl. Mater.*, 241:1147–1151, 1997.

[116] B. V. Mech, A. A. Haasz, and J. W. Davis. Isotopic effects in hydrocarbon formation due to low-energy H+/D+ impact on graphite. *J. Nucl. Mater.*, 255(2-3):153–164, 1998.

[117] M. Balden and J. Roth. New weight-loss measurements of the chemical erosion yields of carbon materials under hydrogen ion bombardment. *J. Nucl. Mater.*, 280(1):39–44, 2000.

[118] J. Roth and C. Garcia-Rosales. Analytic description of the chemical erosion of graphite by hydrogen ions. *Nucl. Fusion*, 36(12):1647–1659, 1996.

[119] J. Roth and C. Garcia-Rosales. Analytic description of the chemical erosion of graphite by hydrogen ions. *Nucl. Fusion*, 37(6):897–897, 1997.

[120] C. Hopf, A. von Keudell, and W. Jacob. Chemical sputtering of hydrocarbon films. *J. Appl. Phys.*, 94(4):2373–2380, 2003.

[121] C. Hopf and W. Jacob. Bombardment of graphite with hydrogen isotopes: A model for the energy dependence of the chemical sputtering yield. *J. Nucl. Mater.*, 342(1-3):141–147, 2005.

[122] J. Roth, J. Bohdansky, and J. B. Roberto. On the influence of impurities on the high-temperature sputtering yield of graphite. *J. Nucl. Mater.*, 128(DEC):534–539, 1984.

[123] J. Roth. Chemical erosion of carbon based materials in fusion devices. *J. Nucl. Mater.*, 269:51–57, 1999.

[124] M. Balden, E. de Juan Pardo, H. Maier, P. Starke, and U. Fantz. Chemical erosion behaviour of doped graphites under hydrogen impact: A comparison of ion beam experiments and planar inductively coupled RF plasmas. *Phys. Scr.*, T111:123–128, 2004.

[125] E. de Juan Pardo. *Characterisation and Mitigation of Chemical Erosion of Doped Carbon Materials.* PhD thesis, Technical University of Munich, 2004.

[126] J. Roth, C. Garcia-Rosales, R. Behrisch, and W. Eckstein. Search for low-erosion carbon materials. *J. Nucl. Mater.*, 191:45–49, 1992. Part A.

[127] R. Schwörer, H. Plank, and J. Roth. Surface modifications and erosion yields of silicon and titanium doped graphites due to low energy d+ bombardment. *J. Nucl. Mater.*, 230(3):208–213, 1996.

[128] http://www.unipress.waw.pl/fityk/. Fityk - A curve fitting and data analysis program.

[129] B. Ravel and M. Newville. ATHENA, ARTEMIS, HEPHAESTUS: data analysis for x-ray absorption spectroscopy using IFEFFIT. *J. Synchrotron Rad.*, 12:537–541, 2005.

[130] J. J. Rehr and R. C. Albers. Theoretical approaches to x-ray absorption fine structure. *Rev. Mod. Phys.*, 72(3):621–654, 2000.

[131] B. Ravel. ATOMS: crystallography for the x-ray absorption spectroscopist. *J. Synchrotron Rad.*, 8:314–316, 2001.

[132] http://icsdweb.fiz karlsruhe.de. Inorganic crystal structure database (ICSD).

[133] Y. Joly. X-ray absorption near-edge structure calculations beyond the muffin-tin approximation. *Phys. Rev. B*, 63(12):125120–10, 2001.

[134] Y. Joly. FDMNES User's Guide. 2007.

[135] K. Schmid. SpecInteg, 2005.

[136] http://gwyddion.net. Gwyddion.

[137] E. S. Gadelmawla, M. M. Koura, T. M. A. Maksoud, I. M. Elewa, and H. H. Soliman. Roughness parameters. *J. Mater. Process. Technol.*, 123(1):133–145, 2002.

[138] L. I. Vergara, F. W. Meyer, H. F. Krause, P. Traskelin, K. Nordlund, and E. Salonen. Methane production from ATJ graphite by slow atomic and molecular D ions: Evidence for projectile molecule-size-dependent yields at low energies. *J. Nucl. Mater.*, 357(1-3):9–18, 2006.

[139] M. Balden, J. Roth, E. D. Pardo, and A. Wiltner. Chemical erosion of atomically dispersed doped hydrocarbon layers by deuterium. *J. Nucl. Mater.*, 313:348–353, 2003.

[140] P. Starke. *Chemische Erosion verschiedener Kohlenstoff-Materialien durch Wasserstoff-Isotope in Niederdruckplasmen.* PhD thesis, Universität Augsburg, 2005.

[141] P. Starke, U. Fantz, and M. Balden. Investigations of chemical erosion of carbon materials in hydrogen and deuterium low pressure plasmas. *J. Nucl. Mater.*, 337-39(1-3):1005–1009, 2005.

[142] U. Fantz and H. Paulin. Chemical erosion of carbon at low temperatures and low ion energies. *Phys. Scr.*, T91:25–28, 2001.

[143] G. Speranza, L. Minati, and M. Anderle. The C1s core line in irradiated graphite. *J. Appl. Phys.*, 102(4):043504–7, 2007.

[144] I. Quintana. Production and Characterisation of metal-doped carbon films. Master's thesis, Max-Planck-Institut für Plasmaphysik, 2004.

[145] The International Centre for Diffraction Data. ICDD/JCPDS database PDF-2, 2000.

[146] G.S. Upadhyaya. *Nature and Properties of Refractory Carbides.* Nova Science, New York, 1996.

[147] K. I. Schiffmann, M. Fryda, G. Goerigk, R. Lauer, P. Hinze, and A. Bulack. Sizes and distances of metal clusters in Au-, Pt-, W- and Fe-containing diamond-like carbon hard coatings: a comparative study by small angle x-ray scattering, wide angle x-ray diffraction, transmission electron microscopy and scanning tunnelling microscopy. *Thin Solid Films*, 347(1-2):60–71, 1999.

[148] S.V. Nagender Naidu and P. Rama Rao. *Phase Diagrams of Binary Tungsten Alloys.* Monograph Series on Alloy Phase Diagrams. Calcutta, 1995.

[149] ASM International. Binary Alloy Phase Diagrams, 1996.

[150] M. H. Lin. Synthesis of nanophase tungsten carbide by electrical discharge machining. *Ceram. Int.*, 31(8):1109–1115, 2005.

[151] Z. Q. Li, H. F. Zhang, X. B. Zhang, Y. Q. Wang, and X. J. Wu. Nanocrystalline tungsten carbide encapsulated in carbon shells. *Nanostruct. Mater.*, 10(2):179–184, 1998.

[152] T. Slimani, P. Goudeau, A. Naudon, G. Farges, and J. L. Derep. Grazing-incidence x-ray-scattering study of the microstructure of tungsten carbon-films. *J. Appl. Crystallogr.*, 24:638–644, 1991.

[153] B. L. French, J. J. Wang, M. Y. Zhu, and B. C. Holloway. Structural characterization of carbon nanosheets via x-ray scattering. *J. Appl. Phys.*, 97(11):114317–8, 2005.

[154] W. Ruland and B. Smarsly. X-ray scattering of non-graphitic carbon: an improved method of evaluation. *J. Appl. Crystallogr.*, 35:624–633, 2002.

[155] N. H. Cho, D. K. Veirs, J. W. Ager, M. D. Rubin, C. B. Hopper, and D. B. Bogy. Effects of substrate-temperature on chemical-structure of amorphous-carbon films. *J. Appl. Phys.*, 71(5):2243–2248, 1992.

[156] J. J. Yeh, R. L. Pfeffer, M. W. Cole, M. Ohring, and J. E. Yehoda. Reactions between tungsten and molybdenum thin films and polycrystalline diamond substrates. *Diamond Relat. Mater.*, 5(10):1195–1203, 1996.

[157] R. Sinclair, T. Itoh, and R. Chin. In situ TEM studies of metal-carbon reactions. *Microsc. Microanal.*, 8(4):288–304, 2002.

[158] A. G. Ramirez, T. Itoh, and R. Sinclair. Crystallization of amorphous carbon thin films in the presence of magnetic media. *J. Appl. Phys.*, 85(3):1508–1513, 1999.

[159] T. J. Konno and R. Sinclair. Crystallization of co-sputtered amorphous cobalt carbon alloys. *Acta Metall. Mater.*, 42(4):1231–1247, 1994.

[160] P. J. F. Harris. Solid state growth mechanisms for carbon nanotubes. *Carbon*, 45(2):229–239, 2007.

[161] A. Gorbunov, O. Jost, W. Pompe, and A. Graff. Solid-liquid-solid growth mechanism of single-wall carbon nanotubes. *Carbon*, 40(1):113–118, 2002.

[162] J. Gavillet, A. Loiseau, F. Ducastelle, S. Thair, P. Bernier, O. Stephan, J. Thibault, and J. C. Charlier. Microscopic mechanisms for the catalyst assisted growth of single-wall carbon nanotubes. *Carbon*, 40(10):1649–1663, 2002.

[163] M. Sevilla and A. B. Fuertes. Catalytic graphitization of templated mesoporous carbons. *Carbon*, 44(3):468–474, 2006.

[164] F. J. Maldonado-Hodar, C. Moreno-Castilla, J. Rivera-Utrilla, Y. Hanzawa, and Y. Yamada. Catalytic graphitization of carbon aerogels by transition metals. *Langmuir*, 16(9):4367–4373, 2000.

[165] A. Oya and H. Marsh. Phenomena of catalytic graphitization. *J. Mater. Sci.*, 17(2):309–322, 1982.

[166] G. Comelli, J. Stohr, C. J. Robinson, and W. Jark. Structural studies of argon-sputtered amorphous-carbon films by means of extended x-ray-absorption fine-structure. *Phys. Rev. B*, 38(11):7511–7519, 1988.

[167] J. Diaz, S. Anders, A. Cossy-Favre, M. Samant, and J. Stohr. Enhanced secondary electron yield from oxidized regions on amorphous carbon films studied by x-ray spectromicroscopy. *J. Vac. Sci. Technol. A*, 17(5):2737–2740, 1999.

[168] H. Muckenhuber and H. Grothe. The heterogeneous reaction between soot and NO2 at elevated temperature. *Carbon*, 44(3):546–559, 2006.

[169] J. Stöhr, D. A. Outka, K. Baberschke, D. Arvanitis, and J. A. Horsley. Identification of C-H resonances in the K-shell excitation-spectra of gas-phase, chemisorbed, and polymeric hydrocarbons. *Phys. Rev. B*, 36(5):2976–2979, 1987.

[170] R. Kapoor, S. T. Oyama, B. Fruhberger, B. D. Devries, and J. G. Chen. Characterization of early transition-metal carbides and nitrides by NEXAFS. *Catal. Lett.*, 34(1-2):179–189, 1995.

[171] J. Diaz, S. Anders, X. Zhou, E. J. Moler, S. A. Kellar, and Z. Hussain. Combined near edge x-ray absorption fine structure and x-ray photoemission spectroscopies for the study of amorphous carbon thin films. *J. Electron Spectrosc. Relat. Phenom.*, 103:545–550, 1999.

[172] G. Speranza and L. Minati. Characterization of c-based materials: The evaluation of sp(2) and sp(3) hybrids. *Diamond Relat. Mater.*, 16(4-7):1321–1324, 2007.

[173] http://srdata.nist.gov/xps/. NIST X-ray Photoelectron Spectroscopy Database, 2003.

[174] M. G. Mason. Electronic-structure of supported small metal-clusters. *Phys. Rev. B*, 27(2):748–762, 1983.

[175] J. Luthin, H. Plank, J. Roth, and C. Linsmeier. Ion beam-induced carbide formation at the titanium-carbon interface. *Nucl. Instrum. Methods Phys. Res., Sect. B*, 182:218–226, 2001.

[176] E. Lewin, E.M.J. Johansson, A. Sandell, M. Gorgoi, F. Schäfers, W. Braun, H. Siegbahn, M. Stüber, U. Jansson, S. Svensson, and W. Eberhardt. HIKE experiments at KMC-1: Recent analysis of thin film nanocomposites. *BESSY Jahresbericht*, 2006.

[177] J. Luthin and C. Linsmeier. Carbon films and carbide formation on tungsten. *Surf. Sci.*, 454:78–82, 2000.

[178] K. U. Klages, A. Wiltner, J. Luthin, and C. Linsmeier. Deuterium bombardment of carbon and carbon layers on titanium. *J. Nucl. Mater.*, 313-316:56–61, 2003.

[179] P. Goldstrass, K. U. Klages, and C. Linsmeier. Surface reactions on beryllium after carbon vapour deposition and thermal treatment. *J. Nucl. Mater.*, 290:76–79, 2001.

[180] J. Diaz, G. Paolicelli, S. Ferrer, and F. Comin. Separation of the sp(3) and sp(2) components in the C1s photoemission spectra of amorphous carbon films. *Phys. Rev. B*, 54(11):8064–8069, 1996.

[181] A.A. Haasz, J.A. Stephens, and E. Vietzke. *Particle Induced Erosion of Be, C and W in Fusion Plasmas*, volume 7, Part A of *Atomic and Plasma-Material Interaction Data for Fusion*. International Atomic Energy Agency (IAEA), Vienna, 1998.

[182] A.F. Holleman and E. Wiberg. *Lehrbuch der Anorganischen Chemie*. de Gruyter, Berlin, 1995.

Acknowledgements

Zum Gelingen dieser Arbeit haben eine Vielzahl an Personen beigetragen, denen ich hiermit danken möchte.

Mein erster Dank gilt meinem Doktorvater **Prof. Dr. Dr. Harald Bolt**, der mir die Durchführung dieser Arbeit am IPP ermöglichte. Sein Vertrauen in meine Arbeit und die vielfache Unterstützung bei externen Messkampagnen haben mich sehr gefreut. Für seine neue Aufgabe am Forschungszentrum Jülich wünsche ich alles Gute und viel Erfolg.

Prof. Dr. E. Werner danke ich für die Möglichkeit, meine Promotion an der Fakultät für Maschinenwesen durchführen zu können. **Prof. Dr. U. Heiz** hat sich dankenswerterweise als Zweitgutachter zur Verfügung gestellt.

Meinem Betreuer **Dr. Martin Balden** gilt mein größter Dank für 3 Jahre tolle Zusammenarbeit, bei der ich sehr viel lernen konnte. Sein Vertrauen in mich, sein großer persönlicher Einsatz, seine Expertise und Unterstützung bei Experimenten sowie die vielen hilfreichen Diskussionen sind mir unvergessen. Danke!

Sehr gefreut hat mich die unkomplizierte und erfolgreiche Zusammenarbeit mit **Dr. Patrick Starke**, der die Plamsaerosionexperimente an der Universität Augsburg durchführte. **Dr. Marcin Sikora** danke ich für viele wertvolle Tipps bei meinen ersten XAFS Schritten, sowie für die interessante Messkampagne an der ESRF. **Dr. Monika Rinke, Dr. Michael Stüber** am IMF I des Forschungszentrums Karlsruhe danke ich für die Nutzung des Raman-Mikroskops sowie **Dr. Harald Leiste** für TEM Untersuchungen. **Dr. Edmund Welter** am HASYLAB danke ich für seine freundliche Unterstützung bei allen XAFS Messungen. Sehr viel Zeit aufgewendet hat in den letzten Monaten **Marcin Rasinski** für TEM Präparation und Analyse. Damit konnten "meine" Carbidkristallite doch noch sichtbar gemacht werden; dafür herzlichen Dank!

Für das angenehme Arbeitsklima und die Unterstützung bei Problemen aller Art geht ein ganz großes Dankeschön an alle Kollegen des Bereichs MF, speziell an die Arbeitsgruppe MSC. Ohne das viele Know-How und die Hilfe, die ich jederzeit von Euch erhalten habe, wäre ich oftmals "auf dem Schlauch gestanden". Ich konnte unendlich viel lernen! Besonderen Dank schulde ich **Freimut Koch** für die Sputter-Unterstützung, **Stefan Lindig** für Hilfe mit XRD und SEM und den Ofen-Meistern **Till Höschen**, **Thomas Dürbeck** und **Fabio Genoese**. **Florian Kost** danke ich für seine stete Bereitschaft mir mit unzähligen XPS-Fragen weiterzuhelfen. **Arno Weghorn** ("Mr. Hochstromquelle") sowie dem Beschleuniger-Team mit **Joachim Dorner** (danke für die spontanen Spätschichten!) und **Michael Fußeder** danke ich für gute Zusammenarbeit und lustige Kaffee-Runden. Für die Untersützung bei der Probenvorbereitung und regen kulinarischen Austausch danke ich herzlich **Gabi Matern**.

Dr. Klaus Schmid bin ich für die kleinen, ungeheuer nützlichen Computerprogramme dankbar, sowie für seinen kompetenten Rat aus dem weiten Feld der Physik den ich mir jederzeit einholen konnte. Ebenso danke ich **Dr. Christian Linsmeier**, der jederzeit ein

offenes Ohr für Fragen und Probleme jeder Art hatte.

Für die engagierte und uneigennützige Teilnahme an Synchrotron Messkampagnen danke ich **Michael Fußeder, Florian Kost, Stefan Lindig, Matthias Reinelt, Aurelia Herrmann**, **Joachim Dorner** und **Susanne Köppl**.

Heun Lee danke ich für Korrekturen und Ratschläge bei englischen Formulierungen.

Für die schöne gemeinsame Zeit und die tolle Zusammenarbeit danke ich allen Mit-Doktoranden, vor allem **Thomas Köck, Aurelia Herrmann, Peter Worbs, Verena Paffenholz, Florian Kost** und **Matthias Reinelt**. Es hat mit Euch richtig Spaß gemacht!

Erin Cochran, Rainer Piechoczek, Stefanie Denis und **Jon Jaimerena Muga** danke ich für ihre Mitarbeit.

Meinen Eltern danke ich für ihre Unterstützung, besonders möchte ich meinem Vater für sein stetes Interesse an meiner Arbeit und die guten Ratschläge danken. Meinem Bruder **Dr. Philipp Adelhelm** danke ich für interessante Diskussionen und Test-Messungen. Ich freue mich auf eine Fortsetzung bei unserem gemeinsamen neuen Thema Wasserstoff.

Katrin, während der letzten 3 Jahre hast Du mich stets unterstützt, auch wenn ich Dir zeitweise wegen mancher Dienstreisen einige Mehrbelastung aufgehalst habe. Danke für alles!